Advanced Drug Delivery Reviews 197 (2023) 114830

Contents lists available at ScienceDirect

Advanced Drug Delivery Reviews

journal homepage: www.elsevier.com/locate/adr

Luminescent quantum dots: Synthesis, optical properties, bioimaging and toxicity

Jeladhara Sobhanan [a,b,1], Jose V. Rival [c,1], Abdulaziz Anas [d,*], Edakkattuparambil Sidharth Shibu [c,*], Yuta Takano [a,e], Vasudevanpillai Biju [a,e,*]

[a] Graduate School of Environmental Science, Hokkaido University, N10 W5, Sapporo, Hokkaido 060-0810, Japan
[b] Department of Chemistry, Rice University, 6100 Main St., Houston, TX 77005, USA
[c] Smart Materials Lab, Department of Nanoscience and Technology, University of Calicut, Kerala, India
[d] CSIR-National Institute of Oceanography, Regional Centre Kochi, Kerala 682 018, India
[e] Research Institute for Electronic Science, Hokkaido University, Sapporo 001-0020, Japan

ARTICLE INFO

Article history:
Received 15 December 2022
Revised 26 March 2023
Accepted 14 April 2023
Available online 20 April 2023

Keywords:
Quantum dots
Nanocrystals
Bioconjugation
Fluorescence
Photoluminescence
Cell labelling
Cell imaging
In vivo imaging
Pharmacokinetics
Nanotoxicity
Phototherapy

ABSTRACT

Luminescent nanomaterials such as semiconductor nanocrystals (NCs) and quantum dots (QDs) attract much attention to optical detectors, LEDs, photovoltaics, displays, biosensing, and bioimaging. These materials include metal chalcogenide QDs and metal halide perovskite NCs. Since the introduction of cadmium chalcogenide QDs to biolabeling and bioimaging, various metal nanoparticles (NPs), atomically precise metal nanoclusters, carbon QDs, graphene QDs, silicon QDs, and other chalcogenide QDs have been infiltrating the nano-bio interface as imaging and therapeutic agents. Nanobioconjugates prepared from luminescent QDs form a new class of imaging probes for cellular and *in vivo* imaging with single-molecule, super-resolution, and 3D resolutions. Surface modified and bioconjugated core-only and core–shell QDs of metal chalcogenides (MX; M = Cd/Pb/Hg/Ag, and X = S/Se/Te,), binary metal chalcogenides ($MInX_2$; M = Cu/Ag, and X = S/Se/Te), indium compounds (InAs and InP), metal NPs (Ag, Au, and Pt), pure or mixed precision nanoclusters (Ag, Au, Pt), carbon nanomaterials (graphene QDs, graphene nanosheets, carbon NPs, and nanodiamond), silica NPs, silicon QDs, etc. have become prevalent in biosensing, bioimaging, and phototherapy. While heavy metal-based QDs are limited to *in vitro* bioanalysis or clinical testing due to their potential metal ion-induced toxicity, carbon (nanodiamond and graphene) and silicon QDs, gold and silica nanoparticles, and metal nanoclusters continue their *in vivo* voyage towards clinical imaging and therapeutic applications. This review summarizes the synthesis, chemical modifications, optical properties, and bioimaging applications of semiconductor QDs with particular references to metal chalcogenide QDs and bimetallic chalcogenide QDs. Also, this review highlights the toxicity and pharmacokinetics of QD bioconjugates.

Contents

* Corresponding authors at: Graduate School of Environmental Science, Hokkaido University, N10 W5, Sapporo, Hokkaido 060-0810, Japan (V. Biju). Smart Materials Lab, Department of Nanoscience and Technology, University of Calicut, Kerala, India (E. Sidharth Shibu). CSIR-National Institute of Oceanography, Regional Centre Kochi, Kerala 682 018, India (A. Anas).

E-mail addresses: anas@nio.org (A. Anas), shibu@uoc.ac.in (E. Sidharth Shibu), biju@es.hokudai.ac.jp (V. Biju).

[1] Equal contribution.

https://doi.org/10.1016/j.addr.2023.114830
0169-409X/

1. Introduction

Since the invention of QDs in the 1980s [1,2], they become an attractive class of nanomaterials for biological applications due to their unique size- and material-dependent optoelectronic and luminescent properties, such as bandgaps and photoluminescence (PL) color [3]. The chemical composition and size of QDs decide these properties. For example, the PL is tuned from the UV to the near-infrared (NIR) region by going from CdS to CdTe QDs through CdSe QDs. Also, quantum confinement tunes the bandgap precisely for a given QD composition. For example, blue- to deep-red-emitting CdSe QDs are obtained by tuning the size in the 2 to 6 nm range. Similarly, the PL wavelength can be selected in the UV–vis-NIR-IR region by choosing materials from CdX, PbX, AgX, $AgInX_2$, $CuInX_2$, InP, InAs, etc., where X is pure or mixed chalcogens (S/Se/Te). The significance of colloidal QDs as alternatives to fluorescent dyes for bioimaging has been established [4]. Surface modification focusing on improving photostability, solubility, and biocompatibility is a critical factor in the biological applications of QDs [5], which is accomplished by preparing shells from semiconductors like ZnS, ZnSe, CdS, and CdSe, or encompassing QDs in biologically inert hosts such as a polymer or silica.

An early challenge in the QD field was surface defects and surface-related nonradiative relaxations in organic ligand-passivated QDs, leading to low PL quantum yields (PLQYs). In this regard, semiconductor coatings to form the core–shell QD structures have successfully improved the abilities of QDs by trapping excitons within the structure [6,7]. Encapsulating QDs in a large band gap material suppresses carrier separation between the core and the shell and non-radiative recombination sites on the surface, improving the PLQY and photostability. The core/shell structure typically comprises type II-VI, IV-VI, and III-V semiconductors, such as CdS/CdSe, PbSe/PbS, CdS/ZnS, CdSe/ZnS, Pb/ZnS, Hg/PbS, InAs/CdSe, and InP/ZnS. [8–10].

Many of these QDs find applications in biological science, which extends from imaging target molecules to tracking cellular processes, monitoring disease progression, delivery of drugs, and photodynamic therapy. However, some QDs, especially those carrying Cd, Pb, and Hg are toxic to live cells and can impair biological processes at cellular and ecosystem levels [11,12]. Indium-based QDs may be a better choice to overcome this problem [13,14]. The silver-based QDs such as Ag_2S, Ag_2Se, Ag_2Te, $AgInS_2$, $AgInSe_2$, $AgInTe_2$, and silicon-based QDs may be more promising materials for bio-application due to their low toxicity and abilities to use near-infrared (NIR) laser that is highly bio-permeable [15,16]. However, PLQYs of such QDs are still insufficient compared to conventional QDs such as CdS/ZnS and CdSe/ZnS and need to be improved.

There is a spectrum of QD applications for expanding through the structural design and choice of constituent materials. Further advances in QDs production methods are required to maintain and improve desirable chemical and optical properties and achieve them with high reproducibility. Further progress requires a better understanding of the complete picture of the surface, atomic arrangement, and metastable properties of QDs. From a toxicity perspective, progress must be made in using heavy metals such as cadmium, lead, and mercury. The nanostructuring of QDs plays an increasingly important role in application-specific toxicity and long-term pharmacokinetics. In addition to bio-applications, solar cells and photocatalysis are emerging fields in which QDs attract attention for light harvesting [17,18]. QDs also enable using single photons and the processing of quantum information [19], which relies on coherent light and electron conduction, presenting new challenges and opportunities to exploit quantum confinement effects [20]. As emergent materials that cleverly use quantum effects, quantum dots have potential applications as a luminescent material and as sophisticated bio-sensors [21]. There remain opportunities to design various future device structures realized by QDs. Against this background, this article reviews historical progress and provides an overview of state-of-the-art QD utilization research focusing on biological applications for future developments.

2. Synthesis of QDs

Since 1993, significant advancements have been made in synthesizing QDs. The bottom-up approach of QD synthesis involves a mixture of metal/chalcogenide precursors and ligands that go through nucleation and growth stages. Here, the morphology, size, and crystal structure of fabricated QDs are impacted by many parameters. The reactivity, concentration, and injection time (the hot-injection approach) of the precursors and ligands, the temperature, and the reaction time substantially impact the structure and properties of QDs. Since QD emission is size-dependent, colloidal growth has been carefully controlled to achieve the target radius with a narrow particle size distribution. The hot injection, heating up, and cation exchange methods have been widely used to synthesize QDs. We classify and discuss prominent examples of QD synthesis.

2.1. Cadmium or lead chalcogenide QDs (MX; M = Cd/Pb, X = S/Se/Te)

High-quality cadmium chalcogenide (CdX, X = S, Se, Te) QDs are widely synthesized [5,22] (Scheme 1). The hot injection method is

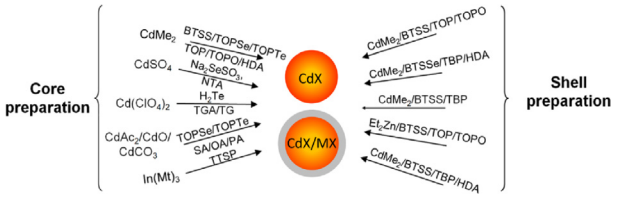

Scheme 1. Standard preparation methods of core–shell CdX (X = S/Se/Te) QDs.

one of the most popular. It uses precursors of cadmium such as dimethyl cadmium ($CdMe_2$), cadmium oxide (CdO), cadmium acetate [$Cd(AcO)_2$] or cadmium carbonate ($CdCO_3$), and sulfides/selenides/tellurides of trioctylphosphine (TOP), tributylphosphine (TBP) or bis(trimethylsilyl) [$(TMS)_2S$] [23–25]. The reaction is carried out at a high temperature in the presence of high boiling solvents such as trioctylphosphine oxide (TOPO), 1-octadecene (ODE), or hexadecylamine (HDA) [26–29]. Bawendi and coworkers demonstrated the preparation of highly crystalline and monodispersed CdSe nanocrystals in an organometallic reaction assisted by saturation, nucleation, and controlled growth of the monomers from precursor solutions of $CdMe_2$ and TOPSe. The resulting nanocrystals showed strong size-dependent absorption and band-edge emission [4]. Weller and coworkers modified the conventional organometallic synthetic route by adding HDA to prepare surface-passivated highly luminescent CdSe nanocrystals exhibiting a PLQY of ~ 50%. They achieved a better-controlled growth rate producing highly-monodispersed and uniform-shaped QDs [27]. Peng *et al.* replaced $CdMe_2$ with CdO precursor and demonstrated the one-pot synthesis of monodispersed CdS, CdSe, and CdTe nanocrystals for large-scale industrial production and green chemistry [30]. They further explored the on-surface mechanism of the growth of CdSe nanocrystals by comparing the difference in activation energies for bulk anionic and cationic surface sites [31]. Another study by Manna *et al.* showed the formation of tetrapod, tripod, dipod, and rod-shaped CdTe [32]. During this process, the zinc blende nucleation is followed by wurtzite phase crystal growth with the help of surfactants such as phosphonic acid. The quality of crystals synthesized using this method depends on the injection and growth temperature. The high temperature facilitates the chemical conversion of precursors to form a saturated solution of monomer that undergoes burst nucleation followed by the growth of nanocrystals in the presence of ligands (surfactants) such as alkyl phosphines, alkyl phosphine oxides, etc. [33,34].

Recently, ODE has been preferred for synthesizing QDs due to its high stability, high boiling point, inertness, low toxicity, ease of handling, and low-cost [35,36]. The solvent molecules bind with unsaturated metal atoms on the surface of growing crystals and thus prevent the formation of bulk-size crystals. Sometimes the solvent molecules themselves act as the ligands for QDs synthesis. The resulting particle size and morphology of nanocrystals are also influenced by various capping agents such as oleic acid, stearic acid, TOP, or TBP. Adding these molecules during synthesis can restrict agglomeration and uncontrolled particle growth during the nucleation [37]. Thus, various parameters such as the reaction temperature, precursor concentrations, the type of precursors, ligands, and solvents are carefully selected to obtain monodispersed and high-quality QDs [38,39]. Nanocrystals formed in this method are capped with hydrophobic ligands such as TOPO, limiting their solubility in water. Thus, the QDs should be surface modified to make them water-soluble, mainly for biological applications, for which techniques like ligand exchange and polymer or phospholipids encapsulation are used. The ligand exchange technique replaces the hydrophobic moieties on the QD surface with ligands such as dodecanethiol, mercaptopropionic acid (MPA), mercapto silanes, dihydrolipoic acid (DHLA), cysteine, polydentate thiols, aminopropanol, peptides, etc. that facilitates stable surface conjugation and aqueous dispersion [40–43]. Dubois *et al.* reported a facile strategy for preparing hydrophilic QDs with improved particle stability [44]. But in some cases, the ligand exchange method has been shown to deteriorate the optical properties, affect the size and shape of QDs and cause particle aggregation [21,45]. Covalent attachment of hydrophilic molecules on the surface or encapsulation of QDs by amphiphilic block copolymers, polyethylene glycol, alkyl saccharides, phospholipid micelles or silica is adopted to alleviate these effects, which preserve the QD properties and minimize dangling bonds [23,46–52]. Recently, Gao and coworkers stabilized CdSe/ZnS QDs with dual silica and polymer encapsulation and demonstrated stable QDs for pH-sensing applications [53].

To further improve the PLQY, direct aqueous route QD synthesis is widely followed [54–61]. The concentration of precursors, pH, reaction temperature, and time are the key parameters determining the quality of crystals formed [59,60,62]. Recently, integrin binding CdTe and CdZnTe QDs with a tunable emission (500–650 nm) and PLQY of ~ 15% were synthesized in a one-pot aqueous reaction using short RGD peptides for specified cell labeling and theranostic applications [63]. Rogach *et al.* demonstrated the synthesis of thioglycolic acid-capped CdTe QDs with emission in the 500–800 nm spectral range and 40–60% PLQY [64]. Thiol capping ligands influence the reaction kinetics, surface quality, optical property, stability, and solubility of nanocrystals [46,65]. Compared to organometallic synthesis, aqueous phase synthesis helps scale up and size-selective precipitation of QDs with high reproducibility. Recently, Wang and coworkers synthesized CdTe/CdS QDs *via* an aqueous route with the emission extending to the vis-NIR region (535–820 nm) and high PLQY (~55%) [66]. Small-size, cysteine-capped CdTe/ZnTe QDs (3–5 nm) were also developed in the aqueous phase for targeted bioimaging, possessing a high PLQY of 52% [67]. Nanocrystals coated with epitaxially grown wide bandgap semiconductor shells such as CdS and ZnS show photochemical stability, higher PLQY, and low surface defects [59,68–71]. Various kinds of semiconductor/semiconductor core/shell nanocrystals developed are CdSe/CdS, CdSe/ZnS, CdTe/CdSe, CdTe/CdS, and CdS/ZnSe [9,72]. ZnS is the common inorganic shell around the core of nanocrystals due to its ideal bandgap, which results in the confinement of electrons and holes within the valence band (VB) and conduction band (CB) of the core material [73–77]. Further, the shell protects the core from the surrounding environment, thus preserving its activity. The energy gap of the core semiconductor determines the emission color. Peng and coworkers prepared zinc blende CdSe QDs coated with CdS shells up to sixteen monolayers epitaxially around the core. They studied the influence of shell-thickness on optical properties such as PLQYs, PL peak positions, PL spectral half-widths, PL lifetimes, blinking kinetics, and crystal structures of core/shell QDs [78]. Another report was the synthesis of CdSe core-coated $Zn_xCd_{1-x}S$ shells *via* a non-injection method from $CdCl_2$, $Zn(OAc)_2$, and thiourea as precursors and glutathione as the capping agent. These nanocrystals showed a PLQY of 35%. But an increase in the shell thickness decreased the PLQY [79].

Recently, cores with multi-shell semiconductors for improved optical properties and high PLQYs such as CdSe/CdTe/ZnSe, CdSe/CdS/$Zn_{0.5}Cd_{0.5}S$/ZnS, CdSe/ZnSe, CdSe/HgTe/CdTe, CdS/HgS/CdS, CdSe/CdS/ZnS, CdS/CdSe/CdS, and CdSe/ZnS/CdSe are also developed [80–86]. Fitzmorris *et al.* demonstrated a facile one-pot synthesis of CdSe/ZnSe/ZnS QDs with a size ~ 6 nm *via* non-injection combined with successive addition of precursors [87]. Here, the PLQY of the QD was increased to 25% compared to CdSe (0.9%) with longer lifetime values of 12 and 30 ns. Aqueous soluble NIR-emitting CdTe/CdSe/ZnS QDs with the PLQY of 84% and emission

in the spectral range of 540–825 nm were also prepared [88]. The ZnS shell around the CdTe/CdSe structure accelerated the indirect radiative recombination at the core–shell interface. Another group reported the hydrothermal synthesis of water-soluble CdSe/ZnS:Mn/ZnS and CdSe/ZnS:Cu/ZnS core/shell/shell doped QDs [89]. The study confirmed that the dopant level around the core influences the bandgap and determines the PL properties of QDs.

Compared to cadmium-based visible light emitting QDs, lead chalcogenide QDs (IV-VI semiconductors) have been widely exploited in the last few decades due to their emission in the NIR region (700–2000 nm) and high PLQYs (greater than 70%) [90,91]. They are employed in optoelectronics, photovoltaics, sensing, and imaging. The absorption and emission of lead-based QDs lie within the biological window (700–1100 nm), where light scattering and autofluorescence are minimal. Thus, these QDs have potential applications for bioimaging, unlike visible-light-emitting QDs, fluorescent proteins, or dyes. Analogous to CdX QDs, lead-based QDs are also synthesized by the hot injection method from lead and chalcogen precursors at a high-temperature [91–97]. Typically used lead precursors are salts such as $PbCl_2$, PbO, and $Pb(CH_3COO)_2$ that form lead oleates with oleic acid (coordinating ligand) in a non-coordinating solvent such as ODE or diphenyl ether. Murray and coworkers reported the first solution phase synthesis of PbSe NCs. Lead oleate and TOPSe precursors in TOP were rapidly injected into diphenyl ether at 150° C to obtain large-size PbSe NCs (3.5–15 nm), further narrowing the size distribution (∼5%) by the size-selective precipitation. The absorption spectra showed size-dependent quantum confinement in the 3–9 nm range. As the crystal size decreased, the separation between electronic states increased, resulting in a blueshifted absorption edge [98].

Inspired by the above synthesis, many groups adopted strategies to obtain good-quality PbX NCs [99]. To obtain large-size colloidal NCs, cubic PbSe QDs of size 20–40 nm were recently synthesized from two types of lead precursors of varying reactivity- lead oleate or lead hexyldecanoate and TOPSe as selenium precursor in ODE solvent. Large cubic crystals were obtained by overcoating the QDs with another layer of lead and selenium precursors. Here, the growth temperature and the choice of lead precursor are the main factors deciding the quality and size of the QDs [100]. Hines *et al.* synthesized colloidal PbS NCs from lead oleate and bis(trimethylsilyl)sulfide (TMS) with a size-tunable absorption in 800–1800 nm spectral range and narrow size distributions (10–15%). The NCs exhibited a PLQY of ∼20% relative to the IR-125 NIR dye [101]. The protocol was further modified to improve the stability, avoid the post-synthesis size focusing, and obtain good-quality PbS QDs [91]. Later, Murphy *et al.* synthesized spherical and cubic PbTe QDs (2.6–18 nm size) from PbO and substituted diphenyl ether with environment-friendly ODE as the solvent [94]. Various parameters such as oleic acid/Pb/Te ratios, temperature, and concentrations were optimized during the synthesis to obtain NCs with a size distribution of 7% with the first absorption peak from 1300 to 1600 nm and a PLQY of 52%. Further, to replace the unstable chalcogenide precursors such as TOPSe and TMS, substitutes such as SeO_2, selenourea in DMF, oleylamine selenide (OLASe), elemental sulfur, sodium sulfide, thioacetamide, hydrogen sulfide gas, tris(diethylamino) phosphine selenide (TDPSe), etc. have been utilized in the synthesis of PbX QDs [102–104]. Modulating the ligands and their interaction with the QDs, precursor concentrations, and the reaction temperature can tune the size, morphology, and stability of PbX nanocrystals. However, these QDs suffer from certain intrinsic limitations for commercialization, including photo-oxidation of the core material under an ambient atmosphere, poor colloidal stability in aqueous solutions, aggregation of QDs after surface modification, quenching of the PLQY, and decreasing stability [105]. Thus, analogous to CdX-based structures, PbX core structures are passivated by the epitaxial growth of inorganic shells such as CdS, CdSe, ZnS, or PbS to obtain core/shell or core/shell/shell QDs [106–109]. Also, cation exchange and ligand exchange reactions based on the Hard and Soft Acid and Base (HSAB) principle on the surface of PbX QDs improved the stability of these QDs [110–112].

2.2. Silver chalcogenide and silver indium chalcogenide QDs (Ag_2X and $AgInX_2$; X = S/Se/Te)

The synthesis of core–shell QDs structures is followed by biofunctionalization to improve biocompatibility. The selection of methods and reaction conditions for synthesizing core–shell and biofunctionalized QDs widely depends on the QD applications. Different precursors and reaction conditions were used to synthesize silver-based QDs (Scheme 2). Notable examples.

include the synthesis of monodispersed Ag_2S QDs with the PL at 1058 nm from a single precursor source $[(C_2H_5)_2NCS_2Ag]$ in cyclohexane [113] and the synthesis of Ag_2S QDs with dodecyl mercaptan coating. In the latter case, hexamethyldisilazane was heated with CH_3COOAg and an organic solvent at 50–110 °C under an argon atmosphere, followed by refluxing a solution of $AgNO_3$ and sodium diethyldithiocarbamate [113–117]. The synthesis at high temperature (190 °C) with fine control over the Ag core and Ag/S ratio has produced uniform-size QDs with an increase in their PL lifetime by six-fold or more. Maintaining the temperature and reagent ratios is critical in synthesizing silver-based QDs because the exposure of silver precursor to high temperature (around 200 °C) for a longer time can cleave the Ag-S or C-S bonds, yielding a mixture of silver-based QDs and Ag NPs. The QDs synthesized using organic solvents are poor in their biocompatibility. Their hydrophilicity was improved by decorating their surfaces with ligands such as MPA and glutathione (GSH), L-cysteine, dimercaptosuccinic acid, bovine serum albumin, and certain target-specific molecules. A water-soluble Ag_2S QDs with 510–1221 nm emission were prepared by reflexing the reaction mixture prepared in ethylene glycol. The synthesis at room temperature with GSH [118], BSA-Ag^+ complexes, and aptamers targeting cancer cells was also reported [119,120]. The molar ratio of Ag:S, Ag: ligand, the degradation rate of sulfur sources, the reaction temperature, and the reaction time were found as the determinant factors of particle size and emission properties of Ag_2S QDs. Ag_2Se QDs were synthesized in a three-neck flask containing a mixture of silver acetate, 1-octane thiol, and ODE. The flask was exposed to 160 °C with vigorous shaking, and the QD formation was initiated with the injection of selenium powder dissolved in tri-n-octyl phosphine [121,122]. A cation exchange-based facile aqueous synthesis method was introduced to synthesize Ag_2Te, in which $AgNO_3$ and CdTe QDs were mixed in a microcentrifuge tube [123–125]. The CdTe QDs for this reaction were synthesized *via* refluxing a mixture of $CdCl_2$, GSH, and NaHTe at 95 °C for up to 150 min.

Ag_2S, Ag_2Se, and Ag_2Te QDs can also be precursors of composite QDs. The exchange of Ag^+ in nearly monodispersed Ag_2S QDs with In^+ at a 3:1 ratio resulted in $AgInS_2$ QDs [126] (Scheme 3). A single-step preparation method of Ag_2S and $AgInS_2$ QDs was reported recently [127–135], in which the refluxing of the precursors of silver (silver acetate), Indium (Indium nitrate hydrate), and sulfur (L-cysteine) at a molar ratio of 1:4:2 at 100 °C for four hours resulting in the formation of water-soluble $AgInS_2$ QDs [132].

The chemically synthesized QDs are decorated with other molecules to achieve site-specific imaging and delivery and avoid non-specific binding and uptake. The nonspecific binding and uptake are generally avoided by coating the QDs with blockers such as bovine serum albumin, polyvinylpyrrolidone, and detergents such as triton x 100 [136]. The biological reduction of bulk materials mediated by microorganisms, plant extracts, or animal cell lines

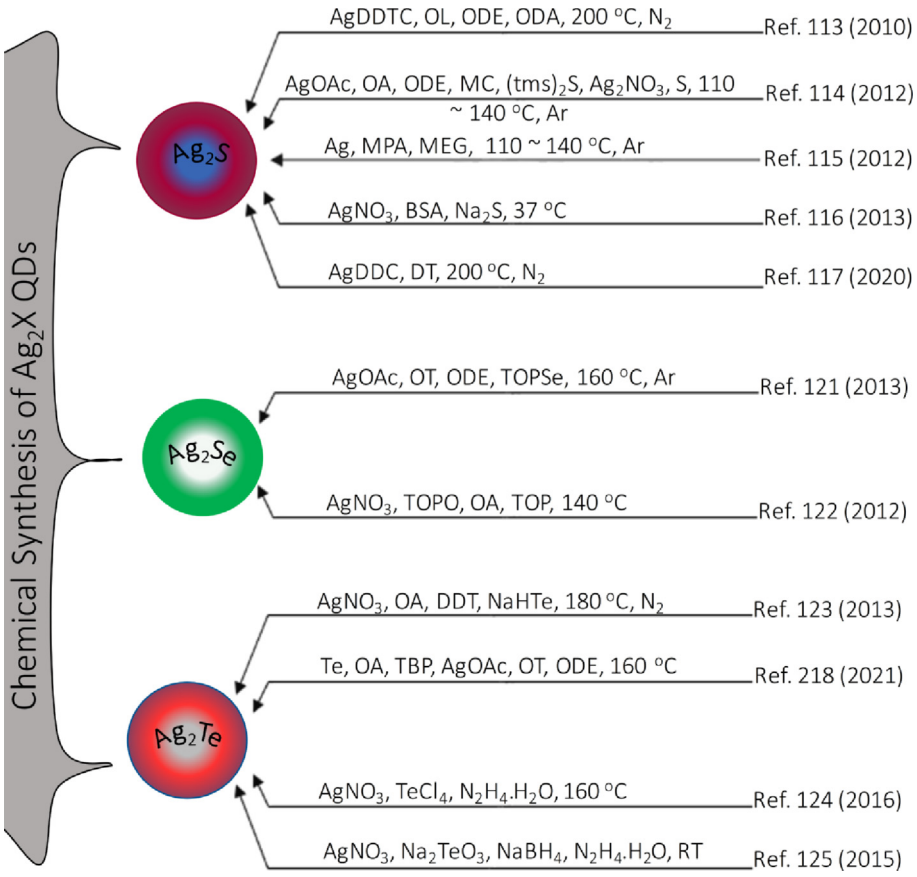

Scheme 2. Standard preparation methods of Ag_2X (X = S/Se/Te) QDs.

can also yield silver-based QDs with comparable optical properties to chemically synthesized ones. Biological synthesis, generally known as "Green synthesis," has been introduced to achieve QDs without toxic chemicals and high-temperature reactions [137]. Metal-reducing agents extracted from plants, such as amino acids, terpenoids, flavonoids, and phenolic compounds, can also orchestrate the production of NPs from bulk materials [138] (Table 1).

Although the biocompatibility and optical properties of such QDs are comparable with the chemically synthesized ones, the long reaction time and lack of control over the reaction are more significant challenges. Microorganisms in natural ecosystems have acquired different mechanisms such as biosorption/bioaccumulation/intracellular sequestration, bio-precipitation, extracellular sequestration, active transport of metal ions (efflux), chelation or reduction of metal ions to deal with the metals depending on their level of toxicity. These adaptation mechanisms can also be used to synthesize NPs in bioreactors [137]. The cell lines having higher concentrations of GSH are widely used in biomimetic synthesis, in which the precursor molecules ($AgNO_3$ and Na_2S) are introduced into the cell culture flasks and maintained in a CO_2 atmosphere. The precursors interacted with GSH within the cytoplasm of cells to produce QDs, the size and optical properties of which may vary with the reaction time. A 20 h reaction in $HepG_2$ cell lines resulted in the production of Ag_2S QDs with an emission at 943 nm [138].

2.3. Silicon QDs

Silicon QDs (Si QDs) have been synthesized using laser pyrolysis, plasma-assisted decomposition, and microemulsion techniques (Scheme 4). In the laser pyrolysis method, the SiH_4 precursors were subjected to high-temperature CO_2 laser pyrolysis to obtain Si QDs of 5–10 nm, which were then dispersed in methanol and etched with hydrofluoric acid and nitric acid for 2–4 min to yield hydrogen-terminated Si QDs [145]. In another method to prepare water-dispersible Si QDs, $SiBr_4$ was decomposed by exposure to 13.56 MHz radio waves [146]. Thus, Si QDs were dispersed in an organic solvent (toluene) by sonication and treated with hydrofluoric acid to remove surface oxides. The microemulsion technique used $SiCl_4$ as the precursor, dissolved in anhydrous hexane and pentaethylene glycol monododecyl ether [147]. The mixture was further reacted with allylamine under UV irradiation for four hours.

2.4. Copper indium chalcogenide QDs ($CuInX_2$; X = S/Se/Te)

Compared to the binary QDs (e.g., CdS, CdSe, CdTe, etc.), the colloidal synthesis of copper indium chalcogenide NCs was rather tricky because of the imbalanced reactivity of metal cations (Cu^+ and In^{3+}) towards chalcogenides (S^{2-}, Se^{2-}, and Te^{2-}) [148]. To control the size and chemical composition of QDs and to maintain excellent phase purity, the reactivity of metal cations must be balanced by carefully selecting metal precursors and ligands. According to the HSAB (Hard-Soft Acid-Base) principle, the cations from group I (Cu^+) and group III (In^{3+}) were respectively soft and hard Lewis acids, and the chalcogen anions are soft Lewis bases, and their softness follows the order ($S^{2-} < Se^{2-} < Te^{2-}$) [149,150]. The synthesis of copper indium chalcogenides is more difficult in this situation due to the soft acid and soft base preferred reactivity, particularly in the strongest soft acid and base combination (Cu^+ and Te^{2-}). Different synthetic procedures were used to get around the synthetic difficulties, including the solvothermal, hot injection,

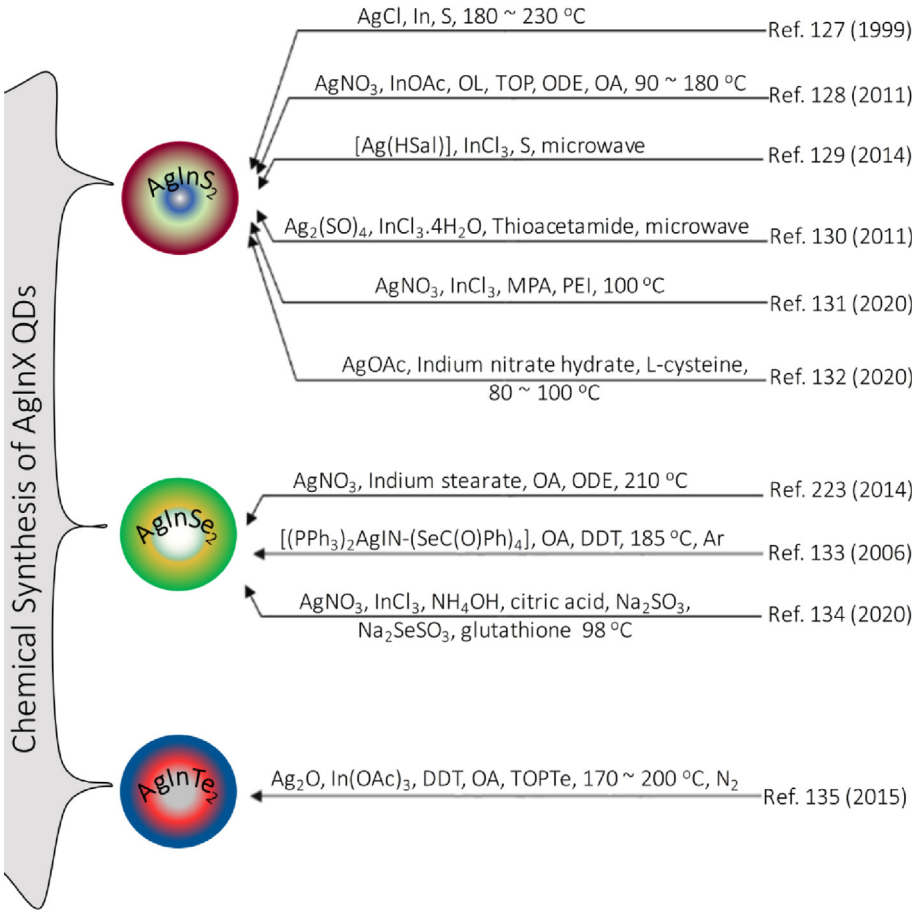

Scheme 3. Standard preparation methods of $AgInX_2$ (X = S/Se/Te) QDs.

Table 1
Major reports on the biological synthesis of silver-based QDs.

QDs	Precursors	Biological agents	Properties		Ref.
			Size (nm)	PL (nm)	
Ag_2S	$AgNO_3$, Na_2S, $Na_2S_2O_3$	Microorganisms: Shewanella spp., Bacillus subtilus, Pleurotus ostreatus	7–12	315 – 470	[137,139,140]
	$AgNO_3$, thiourea	Plant extracts: Camellia sinensis, Combretum mole, Acacia mearnsii, Rosmarinus officinalis, Pistacia atlantica	8–15	~ 520	[141,142]
Ag_2Se	Na_2SeO_3, $AgNO_3$,	Microorganisms: Saccharaomyces cerevisiae	~ 4	1100–1400	[143]
	$AgNO_3$, Na_2SeSO_3, thiourea	Plant extracts: Camellia sinensis	~ 9	240 – 550	[144]

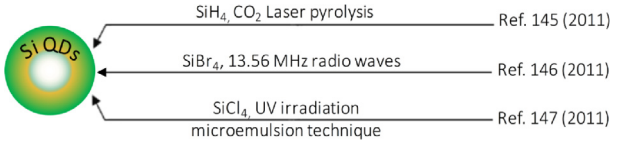

Scheme 4. Standard preparation methods of Si QDs.

hydrothermal, microwave-assisted, and heating-up methods (Scheme 5).

The synthesis of $CuInS_2$ QDs using single metal precursors comprising Cu-S and In-S bonds was introduced to reduce the synthesis complexity and balance the reactivity of metal cations [148,149]. For example, ethyl xanthates, dithiocarbamates, or single-source alkanethiol derivatives were utilized to make metal salts. These Cu and In salts were then combined with oleylamine and heated up to 180 °C for a while, where the thermal decomposition of the metal salts resulted in the formation of $CuInS_2$ QDs [150,151]. This synthesis method could effectively overcome the imbalanced Cu^+/In^{3+} reactivity; however, it resulted in an extra synthetic step (synthesis of single source metal precursors) towards the $CuInS_2$ QDs. The most common and convenient synthetic method for $CuInS_2$ QDs is considered to be alkanethiol-mediated synthesis [152–156]. In this method, the excess thiol ligands (soft base) were introduced along the metal cations to balance the reactivity of Cu^+ and In^{3+} ions with sulfur anions by preferential complexation with Cu^+ ions (soft acid). For example, Xie *et al.*, in their typical synthesis, elemental sulfur dissolved in oleylamine was injected into a ODE solution containing a mixture of Cu^+ and In^{3+} salts, oleic acid, and dodecanethiol at 180 °C [152]. Here, dodecanethiol could reduce the reactivity of sulfide anions (S^{2-}) towards Cu^+ ions rela-

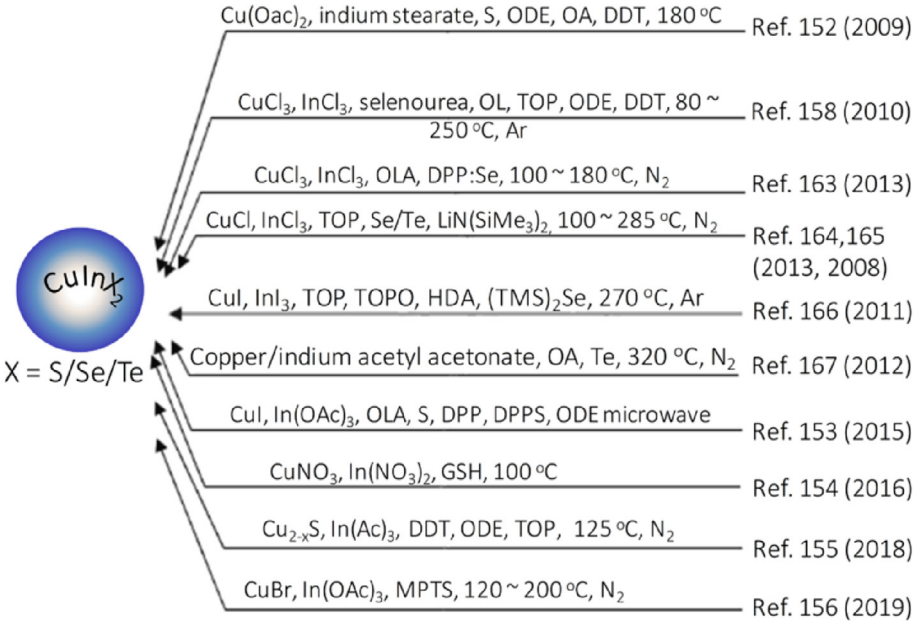

Scheme 5. Standard preparation methods of $CuInX_2$ (X = S/Se/Te) QDs.

tive to In^{3+} ions. Researchers constantly piloted subsequent modifications in alkanethiol-mediated synthesis by varying metal salts and sulfur precursors, injection temperature, and other reaction parameters [149]. In another method, the decomposition of dodecanethiol at a higher temperature was utilized to synthesize $CuInS_2$ QDs. In this heat-up synthetic method, the precursors were heated at a higher temperature for a more extended period in the presence of dodecanethiol to produce $CuInS_2$ QDs. Nevertheless, the prolonged heating time was found to be a disadvantage due to the slow decomposition kinetics of dodecanethiol.

Compared with $CuInS_2$, copper indium selenides ($CuInSe_2$) are significantly less developed [157]. $CuInSe_2$ QDs can be synthesized using the same alkanethiol-mediated synthesis. In a typical synthesis, metal salts (CuCl and $InCl_3$) and selenourea were heated with ODE in the presence of TOP, oleylamine, and dodecanethiol to produce $CuInSe_2$ QDs. However, its applicability is confined due to the slow decomposition of thiols, which results in the formation of anion-mixed [$CuIn(S;Se)_2$] QDs [158]. Also, the synthesis of NCs from a single precursor source is constrained by the exceptionally difficult production of metal selenide precursors [159]. The thiol and air-free synthesis of $CuInSe_2$ QD was carried out by selenium-dissolved oleylamine, or TOP, injected into (or heated with) the solution of Cu^+ and In^{3+} salts [160–162]. Due to the comparatively high reaction temperature and lengthy development time, the generated NCs were usually bigger. It was necessary to improve the reaction kinetics to decrease the size of the produced QDs. Hence, promoting agents like diphenylphosphine [163], lithium salicylamide [164], or trimethylsilyl selenide [165,166] were introduced. For example, diphenylphosphine could successfully help adjust the size of the synthesized $CuInSe_2$ NCs from $\sim$ 1 to 9.2 nm by keeping their stoichiometries constant [163].

The formation of $CuInTe_2$ QDs is extremely complicated due to the strongest soft acid and base interaction (Cu^+ and Te^{2-}), which causes an imbalance in the reactivity of Cu^+ and In^{3+} ions with telluride anions [150]. To overcome this issue, passivating Cu^+ ions with dodecanethiol and reacting with dioctylphosphine oxide were employed [167]. Later, indium-rich $CuInTe_2$ QDs were synthesized *via* an amide-promoted approach [168] or a sequential cation-exchange reaction [169]. In the amide-promoted approach, lithium bis(trimethylsilyl)amide ($LiN(SiMe_3)_2$) was combinedly injected with telluride precursor to the reaction mixture containing metal cations and ligands at a higher temperature [168]. The amide superbase amplifies nucleation by producing highly reactive metal-amide intermediates. As a result, the amide-promoted reaction proceeds more quickly and produces QDs of smaller size. The QDs can successfully replace all the cations or anions by introducing a new cation or anion in the surrounding medium [169]. Here, the $CuInTe_2$ QDs were fabricated by employing a sequential cation-exchange reaction. For this, CdTe QDs could be first changed into Cu_2Te QDs, which are then combined with In^{3+} solution to produce $CuInTe_2$ QDs.

The two essential steps involved in synthesizing core/shell QDs are (i) the preparation of QDs and (ii) the subsequent development of shells around them. The selection and production of the core and shell materials of the QDs were based on the valence and conduction bands of the constituent materials. Based on the bandgap and energy levels, these core/shell QDs were divided into three broad groups, Type-I, Type-II, and quasi-Type II. For example, introducing shell material will shield the core from the outer environment and might be able to passivate the defect states. Hence, surface trapping and non-radiative recombination of photogenerated charge carriers were suppressed by modifying the surface of QDs with wider bandgap materials, such as ZnS. For instance, Xie *et al.* introduced a one-pot method for creating the ZnS shells [152]. A shell could be developed around the NC surface at temperatures typically higher than 210 °C and growth times between 30 min and 2 h. The fabricated shells help enhance the stability of as-synthesized QDs. The practical applications of copper indium chalcogenides QDs are typically limited due to their meager PLQY (<10%) and poor photostability. However, Li *et al.* created a highly scalable approach for creating $CuInS_2$ QD core–shell structures using either CdS or ZnS, which improved the PLQY (from 5 to 10% to more than 80%) and the PL lifetime [170]. Later, McHugh *et al.* successfully demonstrated the fabrication of $CuInSe_2$/ZnS core/shell QDs with the PLQY of more than 20% in the short-wave infrared region (SWIR; greater than 1000 nm) [171]. Interestingly, Zn ions may have entered the core at the start of shell deposition and caused a blueshifted PL emission. However, the extended shell development period improved the PLQY, and the

emission wavelength remained almost unaltered. The observed narrowing of the PL full-width at half maximum (fwhm) demonstrates that the shell coating technique did not affect the size or composition distribution to become wider (from 170 nm to 140 nm). They further demonstrated enhanced photostability of $CuInSe_2$ QDs by fabricating the Al-doped ZnS shells (ZnS:Al). Similar to ZnS coating, aluminum precursors have also been introduced into the reaction mixture to form CIS@ZnS:Al QDs. The fabricated core–shell QDs also showed good photobleaching resistance in simulated sunlight.

2.5. Indium-based binary QDs

Beyond 1300 nm, adjusting the emission maxima of copper indium chalcogenides is challenging. However, using In-based binary QDs, the emission can be tuned in the 500–1600 nm range (for example, InAs, InP). Due to their scant investigations, there are still opportunities for advancement in synthesizing these QDs. The examples of their synthesis from the literature are listed below.

The synthesis of InAs QDs requires control over the reaction conditions due to the covalent nature of their bonds, elevated reaction temperature, and precursor reactivity. Even if researchers can achieve this under such extreme conditions, controlling the size and size distribution of QDs is challenging. In 1995, Wells *et al.* synthesized nanocrystalline InAs by the room temperature reaction of Indium (III) halides and tris(trimethlsilyl) arsenide [$As(SiMe_3)_3$] in toluene and which was further annealed at a higher temperature (~400 °C) to produce black powder of InAs [172]. Later, Guzelian *et al.* produced InAs QDs by the dehalosilylation reaction of $InCl_3$ and $As(SiMe_3)_3$ at 240–265 °C using TOP as a solvent and capping agent [173]. Different particle sizes ranging from 2.5 to 6 nm were obtained with 10–15% size distributions during post-synthetic size-selective precipitation. The PL emission of these QDs was adjustable from 880 to 1200 nm having 0.5–2.5% PLQY. Later, Battaglia and Peng synthesized InAs QDs using noncoordinating solvents such as ODE [174]. They could alter the particle size by introducing various fatty acids with different chain lengths as stabilizing ligands. Following the research output from their regroup, many researchers produced almost monodisperse InAs QDs by employing a size-focusing technique *via* one-pot synthesis [175]. Here, the size-focusing technique was utilized to restrict the unwanted Ostwald ripening process associated with the high reactivity of the arsenic precursor [$As(SiMe_3)_3$].

Even though InP QDs are the most studied III-V semiconductor QDs in terms of synthesis, the initial quality of synthesized QDs was noticeably poor. Also, the synthesis, which typically requires 3–5 days on average, was much longer [172,176–178]. Healy *et al.* fabricated InP QDs for the first time using the chemical reaction of $InCl_3$ and tris(trimethylsilyl)phosphine [$P(SiMe_3)_3$], and X-ray photoelectron spectroscopy (XPS) was used to validate the product [176]. Later in 1995, Wells *et al.* created brown-black InP powder by ultrasonically dissolving Indium (III) halides and $P(SiMe_3)_3$ in pentane and then annealing it at a higher temperature (~400 °C) [172]. The drawbacks of the above-mentioned synthetic approaches were lifted by creating new and improved ones, such as hot injection, heat-up, and seed-growing protocols. For example, using the hot injection technique, Battaglia *et al.* prepared InP QDs [174]. Here, $P(SiMe_3)_3$ precursor was injected into the reaction mixture containing indium acetate and fatty acids in ODE under precise control of the reaction parameters and degassing conditions. This hot injection method was faster, more cost-effective, and more eco-friendly than the abovementioned methods. Tessier et al. recently produced InP QDs by injecting an aminophophine as a precursor and a reducing agent [179]. Later, the heating approach was developed to address the inability of hot injection to make QDs on a large scale [180]. Green *et al.* introduced a single precursor [$In(PtBu_2)_3$] synthesis of InP QDs, by heating it in the presence of a coordinating solvent [181]. However, the uncontrolled reaction kinetics led to a highly unfavorable size distribution. The solvothermal reaction in autoclaves was also considered in the heat-up method [182,183]. Later, the seed-medicated approach was employed to address the size-focused synthesis of QDs. In this method, the nucleation started from an outside source; hence, the growth was controlled and regulated, resulting in better size focusing. For example, Ramasamy *et al.* synthesized monodisperse QDs using a two-step seed-medicated technique. An optimized amount of Zn(In)-P complexes was quickly injected into InP QD seeds holding an average size of 1.9 nm, resulting in larger QDs [184].

InAs and InP QDs are highly susceptible to surface oxidation and have poor electronic tolerance to surface traps owing to their unique tetrahedral coordination. Such surface trap states are responsible for the low PLQY in InAs and InP QDs, which was solved by bandgap engineering to design a heterojunction with a shell around the core. For example, Cao *et al.* fabricated core/shell QDs with InAs as cores and II-VI semiconducting materials (CdSe, ZnSe, and ZnS) as shells with different radii [185]. In this case, the shells were prepared by utilizing high-temperature pyrolysis of organometallic precursors in a coordinating solvent in the second stage after the cores were synthesized using the hot injection approach in the first stage. In further studies, they could generate double shell overgrown InAs/CdSe/ZnSe QDs with the PLQY up to 70%. The sizes of QDs ranged from 1.9 to 6.3 nm, and the corresponding PL emission peaks were tunable over the 885–1425 nm range. Later, Xie *et al.* coated an InAs core with a lattice-matched CdSe shell using a one-pot SILAR (sequential ionic layer adsorption and reaction) approach [175]. Utilizing absorption and PL spectroscopy, they tracked the formation of the CdSe shell and spotted a sizable shift of the PL spectrum to red. Intriguingly, these core/shell QDs displayed a dramatic increase in the PLQY from 1% to 90% with an emission range of 700–1400 nm and a PL fwhm of 70 nm. Later, Franke et al. produced monodispersed InAs core/shell QDs using a continuous injection technique [186]. They used a syringe pump to constantly inject the arsenic precursor [tris(trimethyl germyl)arsine], which helped them to establish strict control over the kinetics of precursor conversion in the nucleation and growth processes. As a result, large InAs QDs (4.5 nm) with narrow size distributions and PL linewidths of 100 nm were obtained. They were subsequently used as cores to produce InAs/CdSe/CdS core/shell/shell QDs emitting in the spectral range of 1300–1430 nm. Due to its identical cubic unit cell, substantial bulk bandgap, and suitable band alignment, ZnS is the most often utilized shell material for InP QDs. Haubold *et al.* used the seed-mediated growth technique to coat ZnS shells on InP QDs [187]. However, they could not attain a PLQY above 23% because of the partial self-nucleation of ZnS. Later, Xie *et al.* adopted the SILAR technique and thermal cycling to prepare core/shell QDs with enhanced emission characteristics, achieving 40% PLQY [188].

Conversely, Li *et al.* improved the PLQY by up to 22% by treating the InP core with zinc stearate before coating it with ZnS [189]. Later, this approach spread widely and has been used to make InP/ZnS QDs and other InP core–shell QDs. Xu *et al.* subsequently developed a quick synthesis technique to prepare InP/ZnS core/shell QDs with the PLQY up to 60% [190]. Zinc carboxylates were used in this case as initiators and stabilizers to enhance the PLQY and solubility of the InP/ZnS core/shell QDs. Recently, Won et al. used a seed-mediated hot injection technique to demonstrate double-layer coated InP/ZnSe/ZnS QDs with almost unity PLQY [191]. They employed hydrofluoric acid to eliminate the oxidative InP core surface during growth to prevent Auger recombination and increase the PLQY.

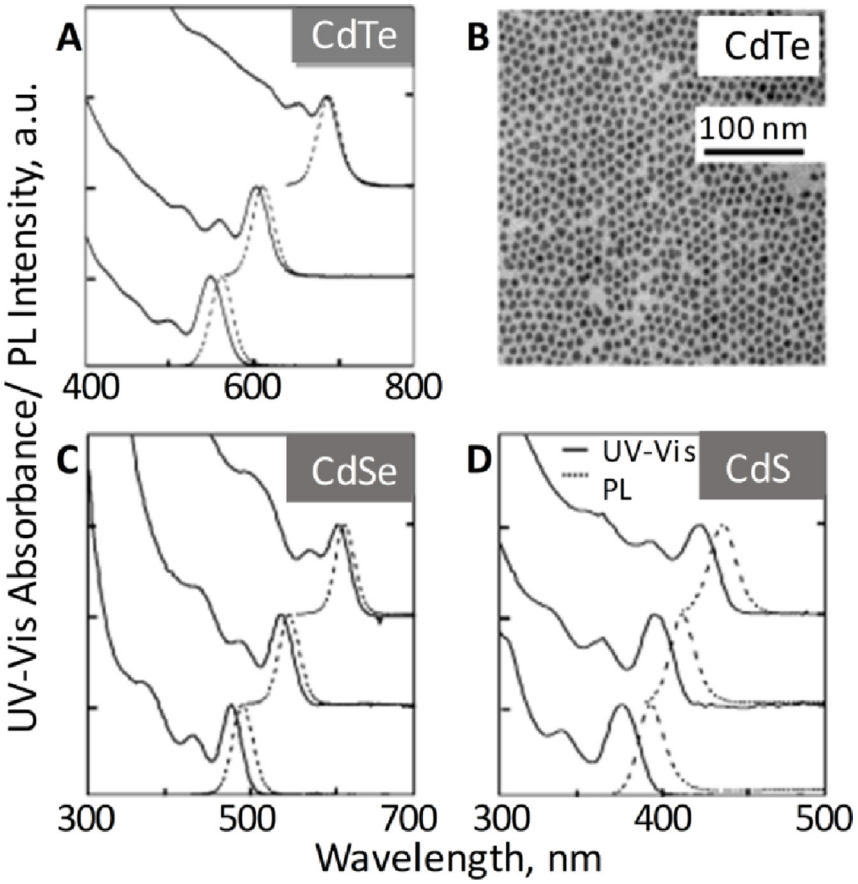

Fig. 1. Absorption and PL spectra of (A) CdTe, (B) CdSe, and (D) CdS QD solutions showing the temporal evolution of the size of the crystals, causing spectral redshifts. Reprinted with permission from Ref. [201].

3. Optical properties of QDs

3.1. Cadmium or lead chalcogenide QDs (MX, M = Cd/Pb; X = S/Se/Te)

Well-designed QDs are exceptionally bright with high PLQY and show high photostability and unique electronic properties resulting from the reduced size ranging from 2 to 20 nm in diameter [192]. The excitons in QDs are bound by the Coulomb interactions and tightly confined in three dimensions. Quantum confinement influences QD's electrical, optical, and mechanical properties due to their peculiar tunable bandgap properties with particle shape and size [193,194]. A decrease in the particle size towards the nanoscale increases the interband energy and results in quantum confinement. The effect of quantum confinement on the optical absorption of a QD was first demonstrated in 1990 by Luis Brus and Moungi Bawendi using quantum mechanical molecular orbital calculation [195]. The bandgap energy becomes larger with the decrease in particle size towards the Bohr radius. QDs show excellent optoelectronic properties compared to bulk materials due to the size within the exciton Bohr diameter. CdX QDs exhibit a broad and continuous excitation range and narrow Gaussian emission spectra, with the first exciton peak 15–30 nm less than the emission peak and increases with a decrease in wavelength together with the appearance of second and third excitonic peaks [196,197]. Excitation to levels away from band-edge states results in their broad absorption. They also possess high PLQY (0.1–0.9), large molar extinction coefficients (10^5-10^7 $M^{-1}cm^{-1}$), and large two-photon absorption cross-sections (ca. 10^3-10^4 GM). CdSe, CdS, and CdTe QDs have intrinsic bandgaps of 1.74, 2.4, and 1.5 eV, which can be further tuned by the particle size, surface defect passivation, and doping by impurities [198–201]. Fig. 1 shows the absorption and PL.

characteristics of as-synthesized CdX QDs. The half-width at the half-maximum (hwhm) in the lower energy side of the first excitonic peaks in the absorption curves for CdTe, CdSe, and CdS QDs were 18, 14, and 11 nm, respectively. For PL spectra, the fwhm values for CdTe, CdSe, and CdS QDs were 29, 25, and 18 nm, respectively. The sharp peaks indicate nearly monodispersed QDs, and the size can be tuned depending on the synthetic approach. The size and growth kinetics of these particles can be determined from UV–vis absorption spectra [30]. The high surface-to-volume ratio of QDs generates loosely bound atomic orbitals (dangling orbits) from many bare atoms on the surface. These dangling orbitals contribute to the surface defects, promoting nonradiative relaxation and quenching the PL. Thus, the passivation of these surface defects can also alter the visible range absorption, PL emission, and PLQY. One way to achieve this is by covering the core with a large bandgap material (shell). This also minimizes or suppresses the PL blinking or photo-oxidation of QDs [199,200].

The PL of QDs depends on the relative states of VB and CB and the bandgap of the core and shell. Shells of higher bandgaps confine the excitons within the core, and the energy gap of the core determines the emission wavelength. Such type QDs include CdSe/CdS, CdTe/CdS, and CdSe/ZnS [202]. But the thickness of shells decreases the surface activity of the core. Coating a wide bandgap core material with a narrow bandgap material partially confines the excitons on the shell, as seen in ZnS/CdSe and CdS/CdSe QDs. Though such systems have shown increased resistance to photobleaching, the PLQYs were low. Coating with a wide bandgap material on its surface could overcome these problems. Design

of staggered type QDs involves both VB and CB of the core either at a lower or higher state compared to the shell resulting in the confinement of carriers on the core and the shell. The good spatial separation of electrons and holes in this type results in longer decay lifetimes and increases wavelength accessibility. Examples of this type include CdS/ZnSe, CdTe/CdSe, CdTe/CdS, ZnTe/CdS, ZnTe/ZnSe, and CdSe/ZnSe. Coating further with multi-shells enhances the structural and optoelectronic properties of QDs, such as the bandgap, PLQY, PL lifetime, and the PL wavelength [193,194,203].

PbX QDs are ideal NIR-fluorescent probes owing to their broad absorption of photons in the visible and NIR region [106,204], which exhibit quantum-confined optoelectronic properties similar to CdX QDs [96,97]. PbS, PbSe, and PbTe QDs have high bandgap energies of 0.41 eV, 0.28 eV, and 0.31 eV, and exciton Bohr radius values of 18 nm, 46 nm, and 150 nm, respectively [91,106,205]. Differences in the reaction temperature and precursors provide different sizes and optical properties to PbS QDs (Fig. 2A) [205–207]. Brian *et al.* synthesized PbSe QDs having first, second, and third excitonic peaks and diameters of 8.1, 7.1, and 5.8 nm for samples with 0.58, 0.69, and 0.86 eV, respectively (Fig. 2B). The emission wavelengths of these QDs were tuned in the 1.3–1.5 μm range by changing the size. Similarly, Murphy et al. synthesized 2.9 nm-size PbTe QDs with 41–52% PLQY and PL spectra in the 1. 0 ∼ 2.1 μm range [94].

The PLQY of PbX QDs is generally less than CdX QDs. Small-size QDs of 1.5–4 nm diameter exhibit high PLQYs (greater than 70%), while for QDs in the 5–10 nm size range, it lies in the 20–30% range [208]. DHLA-capped PbS QD synthesized *via* an aqueous route is found to emit in the 870–1010 nm region with a PLQY of ∼10% and it was decreased by ∼20% after one month with no apparent redshift [209]. In another study, GS-capped PbS QDs showed 30% PLQY in water, which was synthesized by a ligand exchange reaction for PL imaging [90]. But surface-modified lead-based QDs have poor colloidal stability in a buffer solution compared to CdX QDs, decreasing the PLQY [210]. The energy band of bulk PbX QDs shows a positive temperature coefficient (blueshift) and a negative pressure coefficient (redshift) with increasing temperature or pressure [211].

The PL lifetime of PbX QDs is determined by several parameters such as the particle size, surface ligands, temperature, and the dispersion medium that influences the surface defects, bandgaps, and the local dielectric constant. For PbSe QDs, the lifetime decreased from 10.5 μs to 1.62 μs when the temperature was increased from 1.4 K to 150 K. Typically, the values range between a few hundred nanoseconds to a few microseconds. PbS QDs also followed a size-dependent decrease in the lifetime. As the size was increased from 2.35 nm to 5.61 nm, the PL lifetime was decreased from 2.57 μs to 0.71 μs [212,213]. In addition, the poor stability of PbX QDs under an ambient atmosphere also affects its PL properties [214].

3.2. Silver-based QDs

The optical properties of QDs, such as broad absorption spectra, narrow emission spectra, and high resistance to photobleaching, are advantageous for their biological applications [16]. The new generation heavy metal-free QDs retain most of the advantages of heavy metal-based QDs, which include the size-tunable emission, a broad absorption band, a narrow emission spectrum, possibilities of exciting multiple QDs with a single excitation source, and high resistance to photobleaching [215]. The unique optical and electronic properties of QDs originating from their quantum confinement offer many advantages to QDs over organic fluorophores. The significant limitations of organic fluorophores for bioimaging applications are narrow absorption bands, broad emission spectra, and photobleaching. Narrow absorption and broad emission spectra of fluorescent dyes limit their application to multiplexed imaging due to the need for multiple irradiation sources and the possible overlap of emission spectra between dyes. The short lifetime and photobleaching restrict their application to prolonged imaging of cellular processes. The size effects of QDs on the bandgap, absorption spectra, and PL color discussed above are exciton Bohr radius-dependent, which is the separation distance between the excited electron and the hole that makes up an exciton. The same can be explained based on the Bohr model of the hydrogen atom, as shown in the following equation.

$$B = \frac{h^2 \epsilon}{e^2} \left(\frac{1}{m_e} + \frac{1}{m_h} \right)$$

Here, ϵ is the dielectric constant of the semiconductor, h is the reduced Planck's constant, e is the electronic charge, and m_e and m_h are the effective masses of the electron and hole, respectively. The exciton Bohr radius of QDs varies depending on the semiconductors used and the QD size, with the e-h pair strongly confining when the physical diameter of a QD falls within the exciton Bohr diameter [216]. This quantum confinement effect orchestrates the size-dependent optoelectronic properties of QDs [215]. The energy gap between the conduction band bottom and the valence band top expands with decreasing QD size, leading to PL spectral shift towards the blue end [195,217]. The exciton Bohr radius of QDs varies with the material (Table 2).

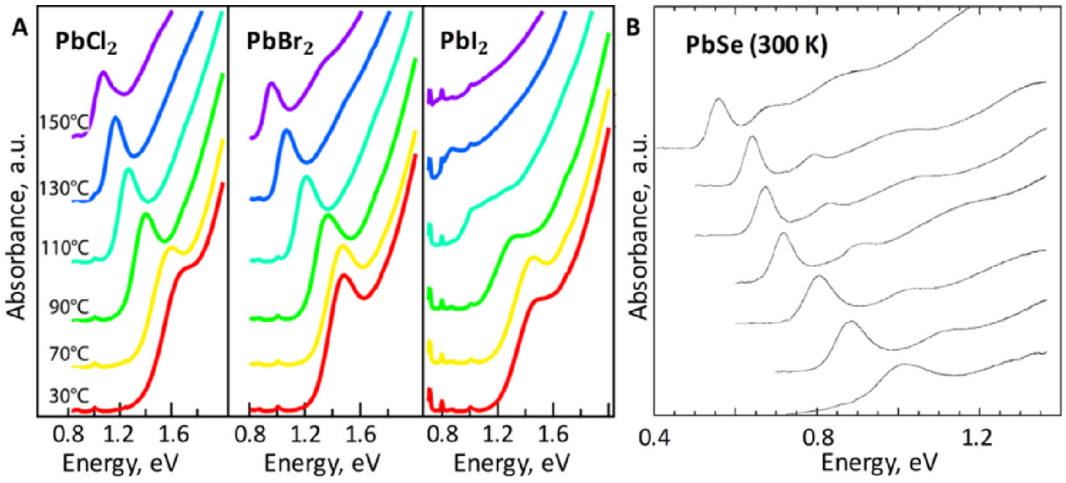

Fig. 2. Absorption spectra of (A) PbS QDs from different precursors [(a) $PbCl_2$, (b) $PbBr_2$, and (c) PbI_2] and at different synthetic temperatures, and (B) PbSe QD samples having different sizes. Reprinted with permission from (A) Refs. [206] and (B) [207].

Table 2
Size-dependent optical properties of silver-based QDs.

QD	Exciton Bohr radius (nm)[a]	Particle size (nm)[b]	PLQY (%)	Emission wavelength (nm)	reference
Ag_2S	2.2	~10 nm	*	785–1058	[113,205]
		1.5–4.6	*	690–1227	[114]
			7–39	780–950	[219]
		5.5–10	*	–	[220]
Ag_2Te	*	5.9 ± 1.1	*	1400	[221]
		16–5.9	12	950–2100	[218]
		250–300	*	340	[218]
$AgInS_2$	5.5	3.5–4.3	36 – 63	770–855	[222]
		1.8–6.2		470–650	[132]
		1.0–3.5	8.76	500–700	[131]
$AgInSe_2$		~24 nm	–	–	[223]
		2	4	650–750	[134]
$AgInTe_2$	3.5	~10.6	13	~1100	[135]

[a] For doped QDs, the Bohr radii of the host material are provided, [b]Sizes from TEM imaging or calculated from absorption spectra are given here. *not reported in the referred manuscript

The cross-section of a QD shows an inorganic core, responsible for the fundamental optical properties, covered by a shell that stabilizes the core and preserves the PLQY. The typical size of silver-based QDs reported in the literature ranges from 1 –10 nm in diameter. Their wavelength can be tuned from UV–vis to NIR (Table 2) by adjusting their size. Fig. 3 shows the optical properties of various AgX QDs. The absorption spectrum of Ag_2S QDs does not show a discrete band. However, the size-tunable narrow band PL emission within 975–1175 nm was observed by increasing the QD size from 2.4 nm to 4.4 nm. The exciton Bohr radius of Ag_2S QDs is at 2.2 nm, and these QDs show redshifted PL spectra up to 1175 nm. Ag_2Te QDs show emission in the 1175–1300 nm spectral range, depending on the precursor concentrations and growth rate during synthesis. The absorption spectrum showed a redshift from 920 nm to 1150 nm as the size was increased from 2 to 2.7 nm [218].

A primary requirement in biological applications is the QDs with PL outside the absorption window of bodily fluids and tissue. The biological medium least attenuates light in the 650–950 nm and 1000–350 nm. Hence, QDs having PL in this range are appreciated for biological applications, especially *in vivo* imaging [224]. The PL of $AgInS_2$ QDs was tuned from 650 to 850 nm by adjusting their size by varying the Ag:In precursor ratio during the synthesis [225]. Another group synthesized $AgInS_2$ NPs with the bandgaps at 2.61, 2.38, and 2.26 eV and peak energies at 1.61, 1.51, and 1.45 eV for 2.5, 3.4, and 4.3 nm diameter QDs, respectively, as shown in the absorption and PL spectra (Fig. 4A) [222]. The absorption spectra of alloyed

$AgIn(S_1Se_x)_2$ QDs exhibited a redshift with an increase in the Se concentration due to changes in the optical bandgaps (Fig. 4B and C) [223]. Further, $AgInTe_2$ QDs strongly absorb the visible and NIR light. The PL emission is tunable in the NIR region depending on

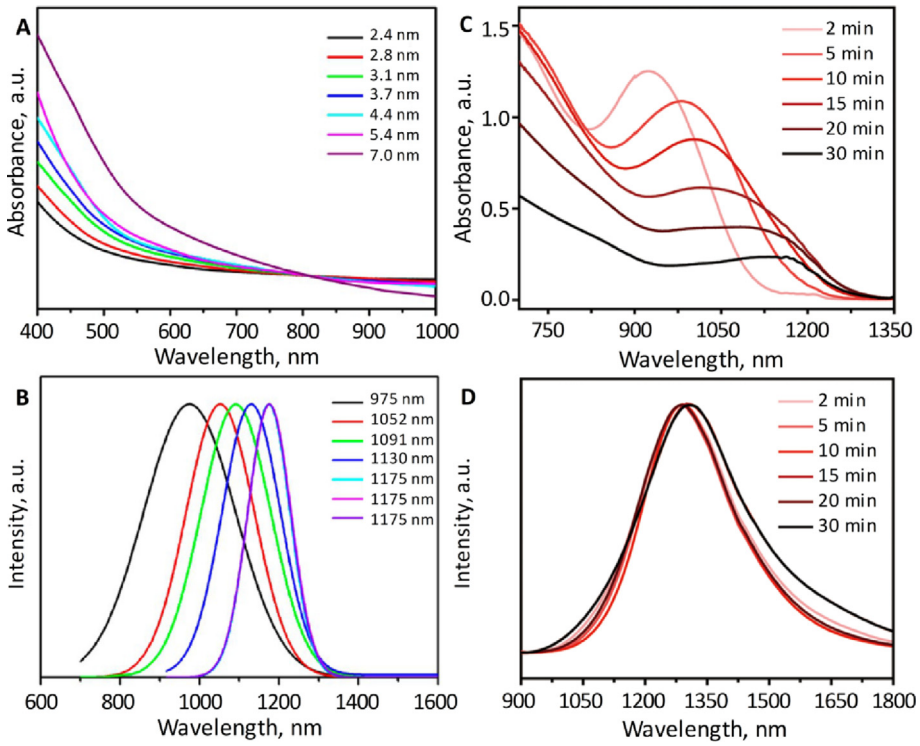

Fig. 3. (Upper panel) Absorption and (lower panel) PL spectra showing (A and B) size-dependent properties of Ag_2S and (C and D) growth time-dependence of Ag_2Te. Reprinted with permission from Refs. [205,218].

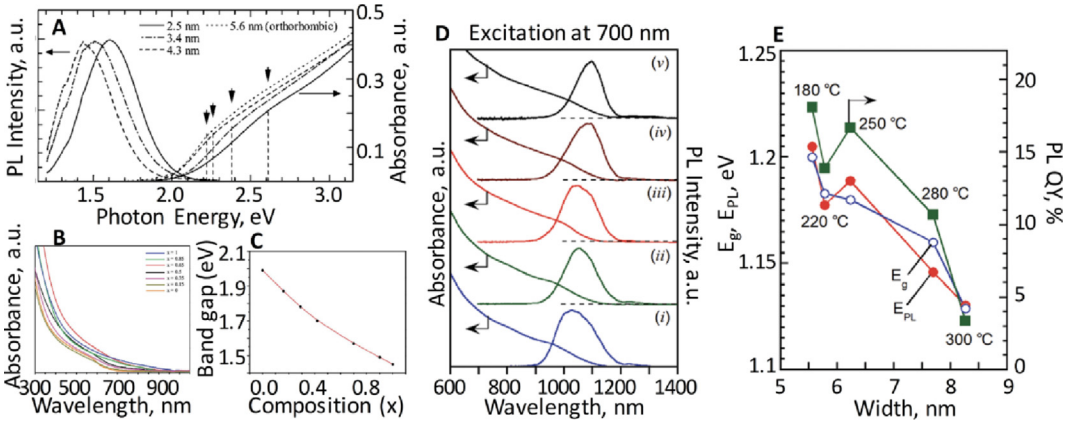

Fig. 4. Absorption and PL spectra of (A) $AgInS_2$, (B) absorption spectra of $AgIn(S_{1-x}Se_x)_2$, and (C) composition-dependent optical bandgap, and (D) absorption and PL spectra of $AgInTe_2$ QDs prepared at (i) 180 °C, (ii) 220 °C, (iii) 250 °C, (iv) 280 °C, and (v) 300 °C, and E) bandgap (E_g), PL peak energy (E_{PL}), or PLQY as a function of the width of $AgInTe_2$ NCs. Reprinted with permission from (A) Refs. [222], (B, C) [223], and (D, E) [226].

the size of nanocrystals, and the fwhm is found to lie between 100 and 150 nm (Fig. 4D, E). In addition, fine-tuning the PL of silver-based QDs could also be achieved by adding Zn to generate quaternary QDs. For example, the PL of ZnAgInSe could be fine-tuned from 660 to 800 nm by varying the Zn:Ag precursor ratio from 5.0:0.5 to 0.5:2.0. Increasing the size of Ag_2S having PL in the 690–820 nm range, and using them as seeds for the second growth process yielded larger QDs with PL ca. 1200 nm. Such a PL maximum was also reported for PEGylated Ag_2S QDs with an average size of 5.6 nm.

3.3. Silicon QDs

Si QDs are excellent nanoprobes for bioimaging applications compared to traditional fluorescent organic dyes due to their NIR emission and high PLQYs. They exhibit broad absorption, narrow emission, and photobleaching resistance from visible to NIR light [16]. The emissive properties of Si QDs are directly influenced by their diameters owing to the quantum confinement of charge carriers. The quantum confinement effect becomes more prominent as the size of Si QDs decreases below the exciton Bohr radius (4.2 nm). The PL lifetime studies suggest that Si QDs may experience both indirect and direct bandgap transitions. Larger silicon nanoparticles (5–100 nm) show indirect bandgap transitions with long exciton-hole recombination time resulting in weak emission. For example, GaAs and CdSe have a high rate of radiative electron-hole recombination, and their radiative lifetimes range from 1 to 10 ns. Recombination occurs more slowly in indirect gap materials like Si, typically in the order of tens of microseconds to milliseconds. On the other hand, theoretical studies of exciton quantum confinement in Si QDs with 1–5 nm imply that a change from indirect to direct bandgap transitions happens for smaller ones [147,227,228]. According to this theory, the excitonic radiative lifetime reduces from milliseconds to nanoseconds when the particle size is decreased from 3 nm to 1 nm [229].

3.4. Copper indium chalcogenide QDs

Like cadmium chalcogenide QDs [230,231], copper indium chalcogenide QDs ($CuInE_2$; E = S or Se) are direct bandgap semiconductors with relatively narrow bandgap energies ($CuInS_2$: 1.53 eV; $CuInSe_2$: 1.05 eV). The $CuInS_2$ QDs have an exciton Bohr radius of about 4.1 nm, and the quantum confinement in this crystal can be seen up to a diameter of 8 nm [232]. Therefore, changing the size of QDs causes the bandgap to vary, enabling emission from the visible to NIR range (450–1500 nm) [152]. Using theoretical analysis, Omata and coworkers further evaluated the effective size-dependent PL of $CuInS_2$ QDs [233].

The absorption features of $CuInE_2$ (E = S/Se) QDs can be varied over the entire visible range based on the QD size. Compared to binary semiconducting QDs, $CuInE_2$ QD's absorption spectra do not exhibit well-distinguished exciton peaks. Instead, these QDs show a broad shoulder and a long tail extending to the NIR region. Many factors contribute to such featureless absorption bands, including the inherent electronic properties, chemical compositions, and size and shape inhomogeneities. The positions of the first excitation peak in the absorption spectra of $CuInS_2$ (CIS) QDs are determined by the second derivative of the local minima, which are redshifted with increasing size (Fig. 5A and B). Coating with a layer of ZnS decreases the probability of nonradiative recombination in trap states. It thus results in enhanced PLQYs with a blueshift in PL maxima and the first excitonic band. The larger molar extinction coefficient was another appealing attribute of $CuInS_2$ QDs [155,234,235]. Based on the size of QDs, both Qin *et al.* and Booth *et al.* created a power law to determine the molar absorption coefficient [234,235]. These findings were later found to have limitations due to challenges in establishing correlations among colloidal QD sizes, positions of the absorption peaks, and concentrations. Recently, Xia *et al.* looked into the molar absorption coefficients of $CuInS_2$ QDs and found that it follows a power law with an exponent of 2.45 at the first exciton transition energy and scale with the QD volume at 3.1 eV [155]. Fig. 5C represents the optical transition in these QDs, which is both size- and composition-dependent for copper chalcogenides. Most importantly, $CuInS_2$ QDs often have a much higher molar absorption coefficient than other biocompatible QDs. Also, $CuInS_2$ QDs display localized surface plasmon resonance bands in the NIR region and electronic transition bands in the visible region due to point defects like copper vacancies [236].

Compared to binary QDs, $CuInS_2$ QDs display broad emission spectra with wider fwhms (90–120 nm). At first, size distribution was assumed to cause the broad PL spectra [237]. Nevertheless, it was determined after extensive research that the broad PL spectrum is connected to the distribution of vibrational states [159]. Further studies demonstrated that the preferential localization of the excitonic hole at copper sites broadens the PL signals [238,239]. Additionally, when compared to other binary QDs, $CuInS_2$ QDs have a significantly longer emission lifetime. For example, non-shelled $CuInS_2$ QDs exhibit biexponential decays, with a faster component lasting between 1 and 10 ns and a slower component delayed up to 100 ns [170]. Furthermore, the presence of multiple electronic states involved in absorption and emission

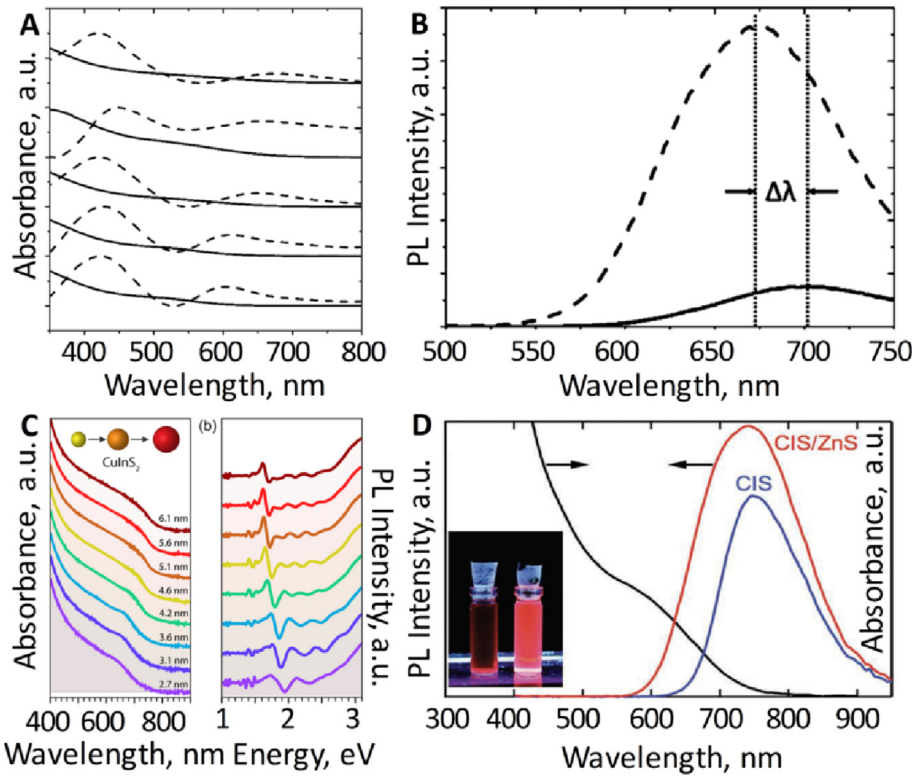

Fig. 5. Absorption and PL spectra of (A) CIS QDs. Bottom to top corresponds to QD sizes of 3.0 nm, 3.2 nm, 3.4 nm, 3.6 nm, and 3.8 nm, respectively. (B) PL spectra of CIS QDs, before (solid line) and after passivation with ZnS (dashed line), showing a blueshift (Δλ). (C) Absorption and PL spectra of CIS and (D) $CuIn_xSe_y$ QDs. Reprinted with permission from (A, B) Refs. [234], (C) [155], and (D) [166].

lowers the reabsorption probability, which otherwise causes more significant Stokes shifts (200–300 meV) [240]. Interestingly, the optical characteristics of these QDs could be modified by changing the particle size and the chemical composition [241]. For $CuInSe_2$ QDs, a bandgap of 1.66 eV was observed with ca. 745 nm emission, and it was shifted to 737 nm by passivation with ZnS shell (Fig. 5D). Here, the fwhm and PLQY were increased to 175 nm (133 nm without ZnS) and 40 ∼ 60%, respectively. The absorption peak was determined at ca. 800 nm [166].

3.5. Indium-based binary QDs

Due to their rapid electron mobility and low exciton binding energy, indium-based binary semiconductor QDs exhibit remarkable optoelectronic properties [242]. InAs QDs show a large exciton Bohr radius (34 nm) and a low bulk bandgap (0.35 eV) due to the quantum confinement effect. On the other hand, the InP QDs have a bandgap of 1.35 eV and an exciton Bohr radius of 10 nm. The large exciton Bohr radius of InAs QDs aids in fabricating large-size QDs. However, due to the comparatively small Bohr exciton radius of InP QDs, ultrasmall particles have been prepared for showing quantum confinement [243]. Indium-based binary semiconductor QDs show sharper excitonic absorption peaks than copper indium chalcogenides, and as the QD size increases, the excitonic peak redshifts. Adam *et al.* identified that the molar extinction coefficients of InP QDs increase with the particle size and could be related to the sample concentrations [244].

Due to surface trap states, the PLQY of indium-based binary semiconductor QDs is relatively low (ca. 2.5%). However, it could be improved by proper surface engineering. For example, surface treatment of InP QDs using hydrofluoric acid substantially improved the PLQY up to unity [191]. Such surface engineering also helped to extend the PL lifetime of InP QDs. Likewise, the fabrication of core/shell structures might enhance the PLQY of various QDs. Fig. 6A shows the spectral features of as-synthesized InAs core and core/shell QDs and samples stored in oxygen for ten months. With time, the absorption edge was shifted to the blue region, with the PLQY continuously decreasing due to the core oxidation [185]. Spectral features of InP/ZnSe/ZnS core/shell/shell green QDs in another are shown in Fig. 6B and C. With the introduction of multilayer shells, the absorbancy increased below 450 nm, and InP/ZnSe/ZnS QDs showed ∼95% PLQY. Also, the PL spectral width (fwhm = 36 nm at 528 nm) was decreased considerably [245]. The emission spectra generally exhibit a bathochromic shift as the size of QDs increases. For example, the PL spectrum of InP covers the visible and NIR region, whereas InAs emits at shorter wave infrared regions as the size increases [14,246].

4. Biological applications of QDs

4.1. Cadmium or lead chalcogenide QDs

The narrow excitation and broad emission of conventional fluorophores, such as organic dyes and fluorescent proteins, restrict their biomedical applications for several reasons. The limitation of probes for multiple excitations of fluorophores, spectral cross-talk between various detection channels, and photobleaching of these probes are lifted by using QDs cross-linked to different biomolecules such as peptides, nucleic acids, antibodies, polymers, and ligands [247–255]. The widely adopted strategies for attaching biomolecules to QDs involve conjugation *via* biotin-streptavidin interaction and crosslinking using EDC/NHS, SMCC, DMT-MM, SATA, SPDP, etc. for targeted diagnosis and drug delivery applications [256–261]. The unique optical properties of cadmium-based QDs, such as broad excitation and narrow emission bands in the

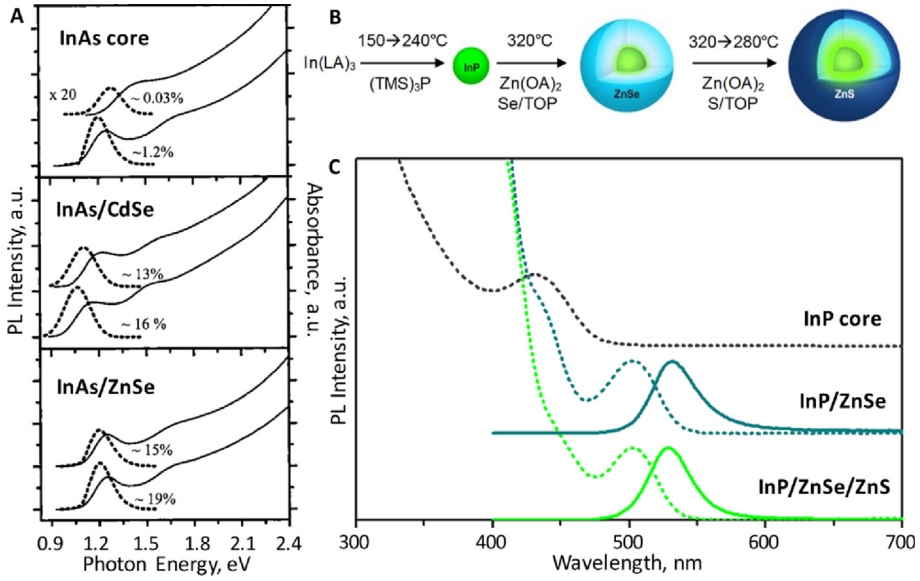

Fig. 6. Absorption (solid lines) and PL (dotted lines) spectra of (A) InAs, InAs/CdSe, and InAs/ZnSe QDs. (B) A synthetic scheme of InP core QDs InP/ZnSe/ZnS core/shell/shell QD preparation. (C) Absorption (dotted lines) and PL (solid lines) spectra of InP, InP/ZnSe, and InP/ZnSe/ZnS QDs. Reprinted with permission from (A) Refs. [185], and (B) [245].

UV-NIR spectral region, high photostability, high PLQY, high molar extinction coefficients, and one- and multi-photon absorption cross-sections make them ideal for biosensing, bioimaging, and cancer therapeutic applications [66,261–264]. For example, CdS QD labeled blocker DNA from the hybridized hairpin-blocker complex was utilized for sensitive detection of target DNA through a target-induced displacement reaction. The cadmium ions released from the blocker DNA are quantified by voltammetry, and the PL signal intensity was increased with increases in the target DNA concentration. The detection limit was 1.2 pM, and this method showed good reproducibility [265].

Another report showed the detection of melamine using mercaptopropionic acid labeled CdSe QDs synthesized from an aqueous route (Fig. 7A and B). The interaction between

positively charged melamine and the negatively charged QDs resulted in QDs PL quenching which was proportional to the concentration of melamine [265]. NIR-emitting QDs have recently been employed to improve optical sensing further and determine specific metal ions to avoid scattering and background fluorescence in the visible region. Also, QDs are excellent energy donors, making them promising for constructing FRET pairs. The PL properties of QDs have been utilized to detect various biomolecules and elucidate different molecular recognition processes in the presence of target analytes [266]. A FRET-based CdTe-guanine and gold NP-cytosine conjugates as fluorescent turn-on probes were used for the bioanalysis of guanine (Fig. 7C-E). The base-pairing interaction between the nucleobases guanine and cytosine formed the QDs-guanine-gold NP-cytosine complex, which quenched the PL of QDs due to energy transfer from QDs to gold NPs. The gold NP-cytosine conjugate preincubated with guanine didn't show any FRET due to the formation of complementary cytosine-guanine bases, and the PL intensity of QD-cytosine was increased with the concentration of free guanine [267].

Similarly, QDs conjugated with nucleic acids, aptamers, or functional proteins have been exploited to detect RNA/DNA sequences and analyze protease activities [268,269]. Cadmium-based QDs as electrochemical and fluorescent labels are also promising for immunoassay to determine protein biomarkers and to develop new readout techniques based on electrochemical and microfluidics [269–271]. They offer a high signal-to-noise ratio and intense emission for an extended period to observe various cellular and biophysical processes. CdSe/CdS/ZnS QDs coated with peptides were used to track single glycosyl-phosphatidyl-inositol-anchored avidin (Av-GPI) test probes in HeLa cells. Using total internal reflection fluorescence (TIRF) microscopy and single-QD tracking, the lateral diffusion behavior and interactions of Av-GPI with glycosphingolipid GM1-rich plasma membrane microdomains and with caveolae were studied [79]. Thus, single-molecule detection using QDs has enabled an understanding of cell membrane dynamics, motor protein kinetics, and gene regulation mechanisms [80–82].

QDs conjugated to antibodies/peptides/ligands have been extensively applied for various immunoassays, including labeling membrane proteins, nuclear antigens, fixed cells and tissues, chromosomes/DNA, and microtubules [83]. *In vitro* imaging using QDs has opened intriguing possibilities for identifying many molecular markers overexpressed on cancer cells. Primary or secondary antibodies conjugated to QDs mark the receptors overexpressed on cells, which help diagnose and image tumor cells derived from the breast, pancreatic, bone marrow, glioblastoma, etc. Water-soluble GSH-coated CdSe/CdZnS QDs coupled with anti-HER2 antibody using sulfo-SMCC, exhibiting a PLQY of ~0.4, were prepared and used to determine the expression level of HER2 on KPL4 human breast cancer cells by fluorescence imaging [273]. Similarly, QD-antibody conjugates were valuable for multiple labeling and multicolor imaging of live cells (HeLa and AX2 cells) [274]. As an alternative to the high-cost antibodies, ligands such as folic acid (FA), transferrin, epidermal growth factors (EGFRs), aptamers, etc., conjugated to QDs are used in identifying and imaging cancer cells. Singh and coworkers introduced CdSe/CdS/ZnS-MPA and CdTe-mercaptosuccinic acid (MSA) QDs conjugated to FA and anti-HER2 antibodies having 59% and 77% PLQYs, respectively. Confocal imaging of human MCF7 breast cancer cells showed efficient receptor-mediated endocytosis and cytotoxicity for QD-FA conjugates compared to non-folate QDs [275]. Another application of QD-FA conjugates is the combined X-ray computed tomography and photothermal therapy (PTT, Fig. 8) using silica NPs multifunctionalized with CdSe/ZnS QDs and GNRs (GNR@SiO_2@QDs).

Fluorescence cell images in this report revealed that GNR@SiO_2@QDs were selectively internalized by folate receptors expressing HeLa cells. Further *in vitro* studies demonstrated a

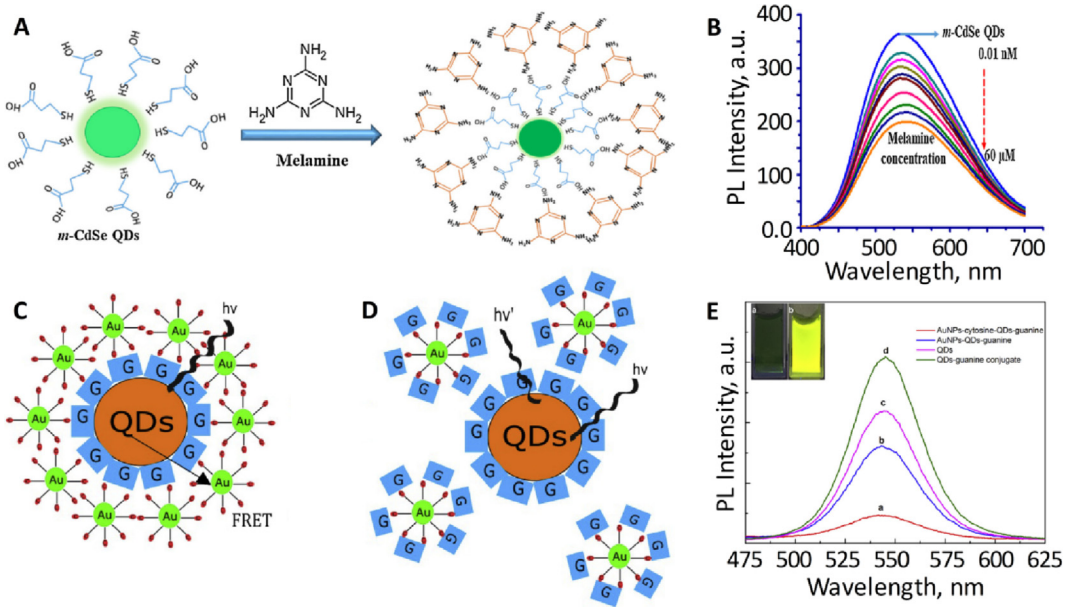

Fig. 7. (A) Pictorial representation of complex formation between m-CdSe QDs and melamine, (B) QD PL spectra with different concentrations of melamine [0.01 nM to 60 μM], (C) a scheme of the FRET mechanism between QDs-guanine and AuNPs-cytosine, (D) a scheme of the interaction of AuNPs-cytosine pre-incubated in guanine solutions with QDs-guanine dispersion, and (E) PL spectra of (a,b,d) QDs-guanine conjugates (a) with AuNPs-cytosine, (b) with AuNPs, and (d) without any additive, and (c) pristine QDs. Inset of E: optical images under 365 nm UV lamp for (left) QDs-guanine-AuNPs-cytosine FRET system and (right) QDs-guanine-AuNPs. Reprinted with permission from Ref. [267,272].

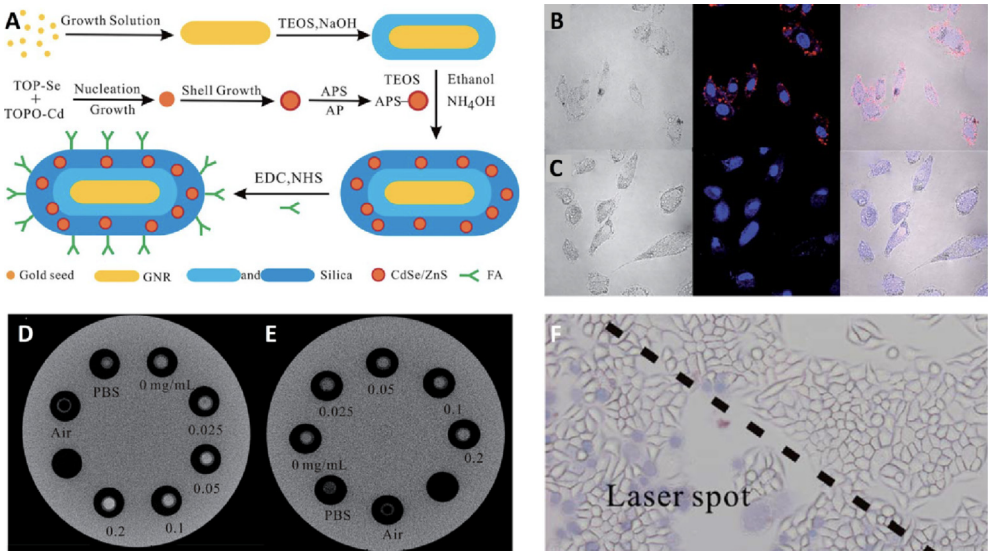

Fig. 8. (A) A scheme of GNR@SiO_2@QD–FA preparation. (B and C) bright-field, fluorescence and merged images of HeLa cells labeled by (B) GNR@SiO_2@QD–FA and GNR@SiO_2@QDs. (D, E) CT images of HeLa cells treated with (D) GNR@SiO_2@QD–FA and (E) GNR@SiO_2@QDs. (F) Photothermal therapy effects of GNR@SiO_2@QD-FA on HeLa cells irradiated for 4 min with 810 nm laser. Reproduced with permission from Ref. [276].

strong X-ray attenuation and high heat generation from GNRs are ideal for theranostic applications [276].

Bioimaging has recently focused on NIR QDs and NIR light owing to their high spatiotemporal resolution, non-ionizing radiation, and absence of tissue autofluorescence [277]. Deep tissue imaging utilizing NIR QDs in the 700–1700 nm spectral window has enabled the study of various molecular, physiological, and metabolic functions. NIR QDs reported so far bioimaging include CdTe/CdSe, CdSeTe/CdS, CdTeSe/CdS, CdTe/Cds, CdHgTe/ZnS, and CdMnTe/Hg. As multiple QDs can be excited by a single wavelength source for multicolor emission, QDs are excellent probes for *in vivo* imaging and detecting many cancer biomarkers [278–282]. Recently, Zhang *et al.* developed biocompatible core/shell PbS/CdS QD with bright emission ca. 1600 nm under 808 nm excitation, which was applied for noninvasive and high-speed (60 FPS) *in vivo* imaging [283]. This PEG functionalized NIR-IIb QD allowed the excitation and emission to effectively penetrate up to 1.2 mm, which helped image blood flow and tumor vasculatures in mice. Following injection, QDs were accumulated in the tumor region by enhanced permeation and retention (T/NT ~ 32), followed by a biliary pathway-mediated excretion (Fig. 9). Similarly, RGD peptide-functionalized NIR QDs could target the

$\alpha_v\beta_3$ integrins and visualize the tumor vasculature *in vitro* and *ex vivo* in U87MG human glioblastoma tumor-bearing mice. This

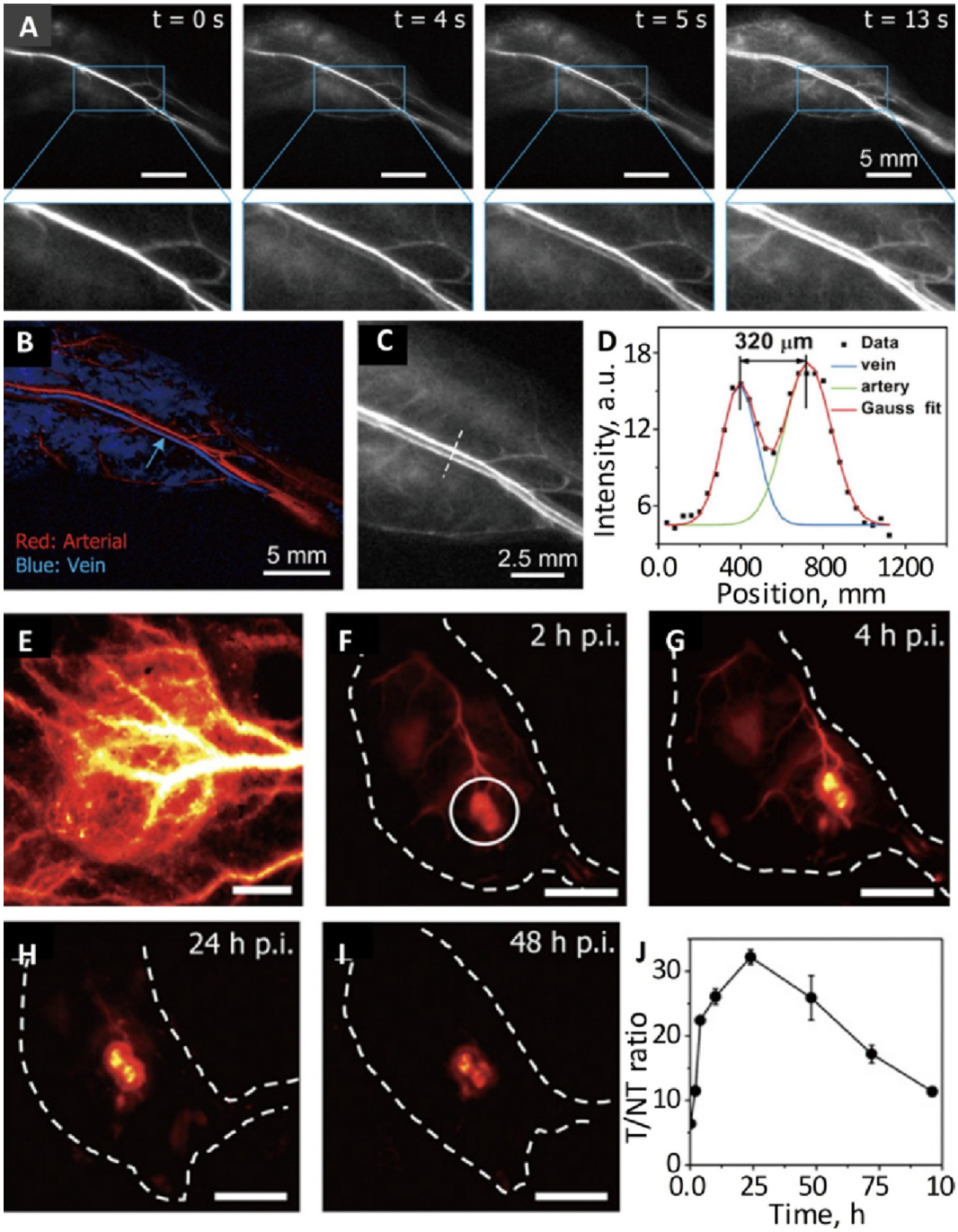

Fig. 9. NIR-IIb imaging of blood flow at 60 fps. (A) A time course of ~1600 nm fluorescence images recorded under 808 nm excitation of a mouse hind limb after i.v. injection of PEG-QDs showing the blood flow returning to the femoral vein after filling the femoral artery; t = 0 corresponds to NIR-IIb signal starting to show up in the femoral vein. (Scale bar: 5 mm.) (B) PCA for differentiation of arterial and venous components, (C) A zoomed-in image of a subregion in the hind limb. (D) Cross-section fluorescence intensity profiles of femoral vein and artery marked in C. (E) High-magnification, wide-field fluorescence image of an s.c. Xenograft MC38 tumor on a mouse after i.v. injection of PEG-CSQDs (Scale bar: 1 mm.). (F-I) Wide-field fluorescence images at different time points after injection (Scale bar: 10 mm.). (J) Time course curve of the tumor-to-normal tissue ratios (T/NT) throughout 96 h post-injection. Imaging parameters: 1500 nm long-pass filter, laser power density ~ 60 mW/cm^2. Reprinted with permissions from Ref. [283].

report showed the possibilities for integrin-targeted NIR fluorescence-guided detection and therapy of cancer cells [284].

4.2. Silver-based QDs

The superiority of QDs in bioimaging and drug delivery compared with fluorescent dyes has been well-defined [286,286]. The high photostability, brightness, large Stokes shift, longer PL lifetime, and high surface area to volume ratios make these QDs suitable for continuous imaging of multiplexed cellular processes at a high clarity, even from deep tissues [286]. The silver-based QDs with emission properties in the NIR window are especially attractive for *in vivo* imaging, as the emission from these QDs is not trapped within the absorption window of biological fluids (Table 3). Apart from some reports on the charge-based interaction of QDs

with cell surfaces, the specific application of QDs primarily depends on the choice of the functional group attached to them.

Table 3
Application of silver QDs to *in vivo* imaging and drug delivery.

QDs	Functionalization	Mode of delivery	Application	Target	Reference
Ag_2S	EDC-NHS	Oral	Drug delivery	Liver	[287]
Ag_2S	Peptide	Injection	Imaging	Tumor	[288]
Ag_2Se	PEG-cetuximab	Injection	Cancer therapy	Tongue	[289]
Ag_2Se	Glucose	Injection	Imaging	Breast tumor	[290]
Ag_2Te	PLGA & cell vesicle	Injection	Imaging	Tumor	[291]
Ag_2Te	PEG	Injection	imaging	Liver, spleen	[221]
$AgInS_2$	Oct-arginine	Injection	Imaging	Stem cell transplant	[292]

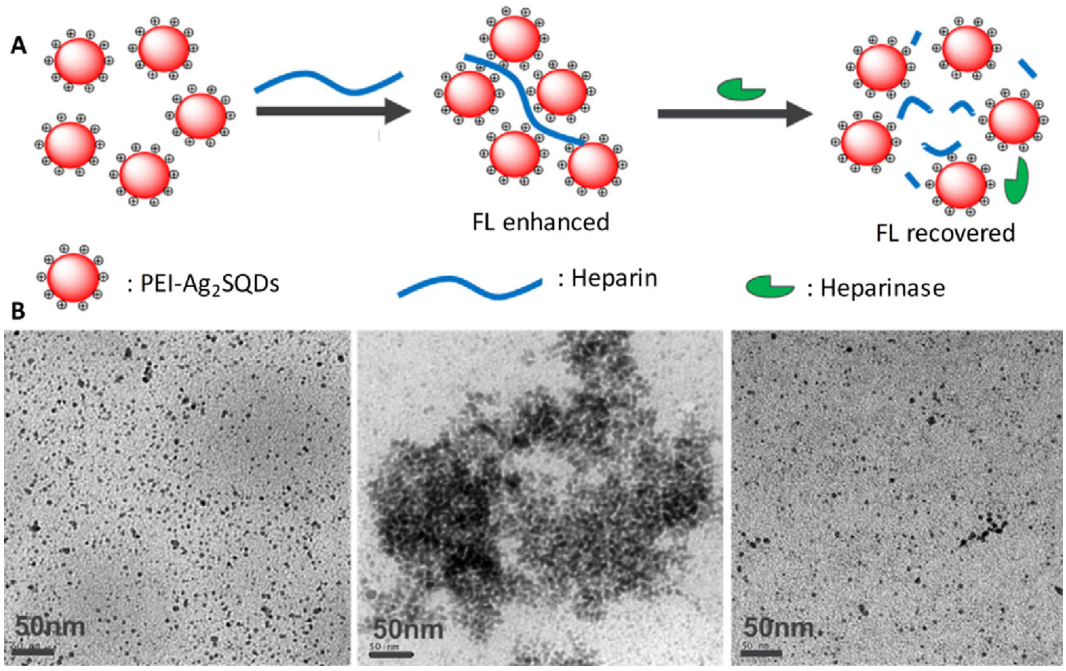

Fig. 10. (A) A scheme of the switch-on-switch-off sensor based on PEI-Ag_2S QDs for detecting heparinase. (B) The TEM images showing the decondensed and condensed PEI-Ag_2S QDs. Reprinted with permission from Ref. [302].

Most studies attached small molecules [290], peptides [293], proteins [294], or antibodies [295] to guide QDs to the target. The QDs are conjugated to the functional molecules through various modes, including electrostatic interaction [296], biotin-streptavidin interaction, direct binding of the thiol group with metals, and direct coupling during synthesis [297].

Although electrostatic binding is an easy choice, the stability of functionalized QDs depends on the pH, temperature, and ionic strength of the reaction medium. Streptavidin-biotin interaction is a simple and more desired conjugation mode. Streptavidin can be covalently linked with the QDs containing carboxyl groups by EDC coupling, and such QDs readily label biotinylated biomolecules [298]. Conjugation of multiple silicon QDs with streptavidin and their specific interaction with biotinylated microbeads were confirmed for biological applications [299]. Streptavidin-biotin conjugation has been utilized to add antibodies, peptides, and small molecules to the surface of silver-based QDs and was used for imaging and tracking biological processes. In one such application, fluorescence quenching of Ag_2S QDs by caffeic acid quinone was used to detect cytochrome *C* [300]. In this approach, caffeic acid quinone was synthesized through a cascade of reactions initiated with the oxidation of trypsin by cytochrome oxidase C to produce a heme peptide [300]. The polyethyleneimine caped Ag_2S QD (PEI-Ag_2SQDs) synthesized by a modified Duman and Wang's method [118,301] was used as the cancer marker heparinase sensor [302] (Fig. 10). The principle of this 'switch-off-switch-on detection' is that the substrate heparin induces a charge-based condensation of PEI-Ag_2SQDs and quenches the PL of QDs. The heparinase enzyme cleaves the heparin, releases the PEI-Ag_2SQDs, and uncages the QD emission [302]. A similar mechanism based on quenching of Ag_2Te and $AgInS_2$ QDs PL was reported for measuring nanomolar concentrations of catechol [303] and dopamine [131]. The NH_2 group in dopamine interacts with the NH_2 group in the MPA and PEI-caped $AgInS_2$ QDs, resulting in their aggregation and fluorescence quenching.

In another application, a linear relation was established between the increase of PL of $AgInS_2$ QDs and ascorbic acid and was proposed for detecting vitamin C [304]. In this case, the enhanced PL is attributed to the abilities of ascorbic acid to suppress the surface defects of QDs. The increased resonance Rayleigh Scattering (RRS) of a thioglycolic acid (TGA) functionalized Ag_2Se QDs on interaction with a Conconavalin A (Con A) have been proposed for preparing biosensors for studying the carbohydrate-protein interactions [305]. Here, the ConA, which can bind specifically to the glucose moiety of a cell membrane glycoprotein, is attached to the TGA-Ag_2SE QDs *via* intermolecular hydrogen bonding. Integrating multiple colored QDs and antibodies within a mesoporous silica NP platform is also propitious for the enzyme-linked immunosorbent assay (ELISA) tool [306]. QDs conjugated with markers are good candidates for immunocytochemical assays in cell biology. These assays generally involve combining cells with markers conjugated with QDs, removing nonspecific or unbound

conjugates by washing, and documentation by fluorescent or confocal microscopy. One of the studies utilized the high glucose consumption of cancer cells; glucose-conjugated Ag_2Se QDs showed internalization in more than 94% of MCF-7 cells compared to non-conjugated QDs [290]. The Ag_2SQDs conjugated with an antagonist (AMD3100) of a chemokine receptor ($CXCR_4$) have been demonstrated for the easy detection of breast cancer cells (Fig. 11) [307].

The $CXCR_4$ is considered one of the efficient markers, over-expressed during the progression of cancer, especially in breast cancer [308]. The $CXCR_4$ also supports the intracellular translocation of QDs conjugated to AMD3100. The intense emission of Ag_2SQDs-AMD conjugate at 860 nm on irradiation with a 660 nm laser facilitates the specific imaging of breast cancer cells. The hyperthermia induced by the same conjugate on irradiation with a 785 nm laser facilitates their therapy. In a similar study, PEG-capped Ag_2Se QDs were conjugated with cetuximab, a clinical anti-epidermal growth factor receptor antibody drug for tumor therapy, through a disulfide reduction and sulfhydryl-amine coupling [289,309]. The QD-drug combination was demonstrated to be efficient for imaging and treatment. FA- targeting the folate receptor of cancer cells conjugated to $AgInS_2$ [310] and $AgInTe_2$ QDs [311] also facilitated the imaging of cancer cells. All these studies show that the QDs can serve as an excellent probe in cell biology for multiplexed detection, identification of target molecules even at low copy numbers, and prolonged high-resolution imaging. However, more scientific studies are needed to estimate the number of antibodies available to hybridize with the target protein to increase sensitivity. Also, efforts are required to avoid the nonspecific binding of free streptavidin with biotin synthesized by some cancer cells [312]. Evolving from the earlier studies, which focused on labeling cell surface markers, recent studies showed significant improvement in applying silver-based QDs for tracking intracellular processes. A major hurdle in this was the delivery of QDs inside the cell, for which their large size compared to fluorescent dyes and susceptibility to endocytosis arrest was challenging [285].

Cell-penetrating peptides have been known to translocate proteins, magnetic NPs (~40 nm), and liposomes (~200 nm), which are hydrodynamically larger than the QDs (5–15 nm) and hence can be readily transported. A straightforward approach to this is the self-assembled preparations of peptides over the QDs, but it does not support control over the size, shape, and composition of the QDs [296]. A cell-penetrating peptide, RGD, was conjugated with DOX- functionalized Ag_2S QDs through an acid–amine coupling reaction to target tumor cells [313]. The cell-penetrating TATE peptide, which binds somatostatin receptor subtype-2 (SSTR2) explicitly, was conjugated on the surface of an Ag_2Se QDs to image the SSTR-2 overexpressing neuroendocrine tumor [314]. The Ag_2S QDs and RGD peptide cross-linked on the surface of a self-assembled amphiphilic peptide nanochain was used to label the integrin receptor $\alpha_v\beta_3$ of the cancer cells [315]. A BSA-coated Ag_2SeQDs conjugated with a cancer marker Arg-Gly-Asp (RGD) and drug doxorubicin (DOX) also exhibited similar properties in tumor cells [316]. Here the RGD facilitates the translocation of QDs into the cytoplasm, where the acidic pH induces the protonation of COO-groups derived from BSA and the release of DOX to kill the tumor cells (Fig. 12). The localization of QDs could be visualized by irradiating QDs.

The stability of QDs is a significant criterion for their *in vivo* imaging or drug delivery. In most studies, the QDs are applied through oral administration or injection routes. An early report demonstrated the fluorescence from 1 cm deep in the backside of nude mice injected with Ag_2Se QDs in the abdominal cavity [317]. The Ag_2S and Ag_2Se QDs with tunable PL in the NIR region are promising for imaging biological processes, even from 5 mm deep tissues, with high reliability and signal-to-noise ratio [215]. The peptide (Arg-Gly-Asp-Dephe-Lys) conjugated Ag_2S QDs injected in animal models showed a biodistribution including in target tumor cells within one hour of administration, which helped attain the maximum fluorescence contrast within 24 h and image for 30 days (Fig. 13A, B) [288]. The injected QDs are retailed

in the bloodstream for different intervals, depending on the QD functionalization and injection position. The polyethylene-coated Ag_2Te QD injected intravenously in mice was circulated for a short time in the blood and accumulated in the liver and spleen, where it was stable for several days [221]. The degradation products of the QDs were detected in the urine and feces, which indicates their renal and hepatobiliary excretion.

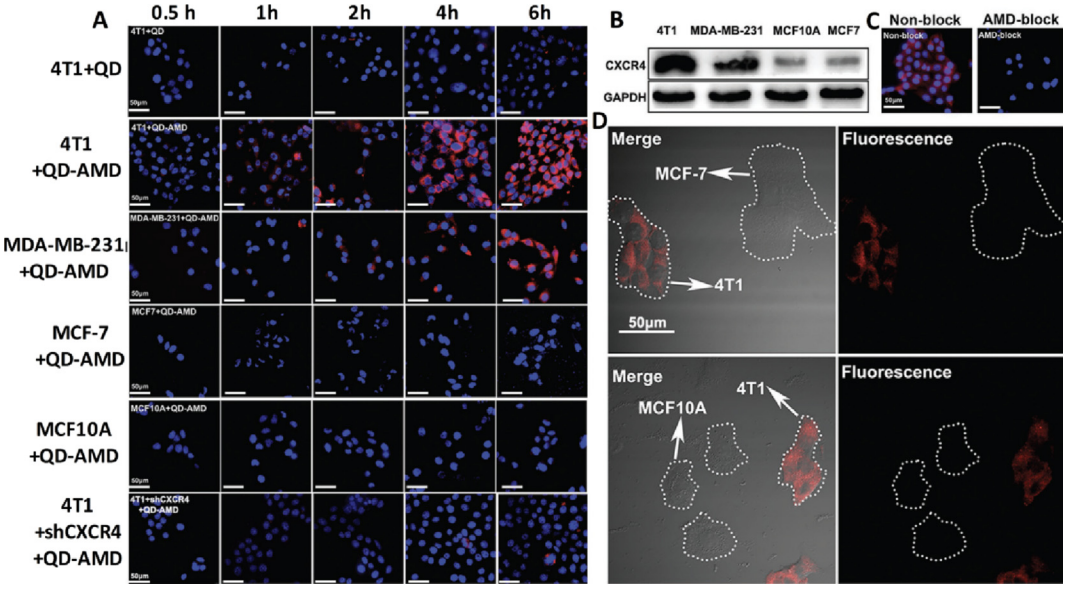

Fig. 11. Imaging of breast cancer cells with different CXCR4 expression by QD-AMD probe. (A) Intracellular fluorescence of QD-AMD in 4T1, MDAMB-231, MCF-7, and MCF-10A cells after incubation for 0.5, 1, 2, 4, and 6 h, and the cellular uptake of the probe by 4T1 cells after the silencing of CXCR4. (B) Western-blot analysis of CXCR4 expression in the four cell lines. (C) Uptake of the probe in cells with and without AMD3100 pretreatment. (D) Confocal microscopy imaging of the selectivity of QD-AMD probe in mixed cell populations (4T1 and MCF-7; 4T1 and MCF-10A). Reprinted with permission from Ref. [307].

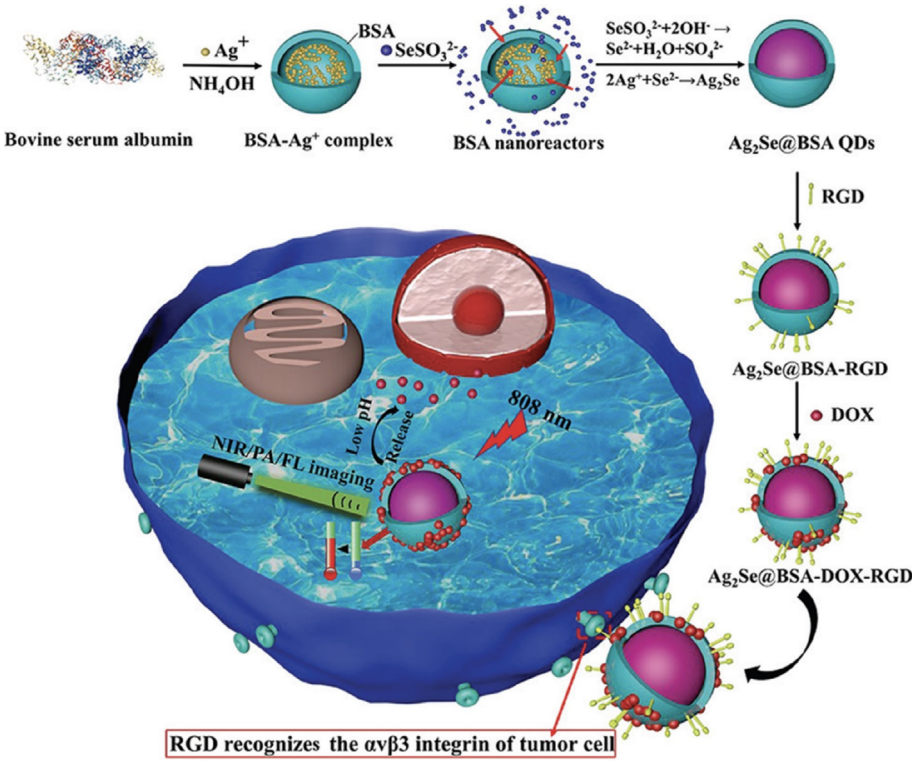

Fig. 12. A scheme of the preparation and mode of action of BSA-capped Ag_2Se QDs functionalized with RGD and DOX. Reprinted with permission from Ref. [316].

QDs may progressively degrade along the gastrointestinal tract, depending on their surface properties, and may fail to pass through the GI tract. The QDs coated with polymers, silica shell, and thiol functional groups and encapsulated within liposomes and dendrimers were more resistant to enzymatic degradation in the gastrointestinal environment [243]. The polymer-conjugated silver sulfide QDs administered orally were reported to translocate through the small intestine wall, through clathrin mediate endocytosis and micropinocytosis, into the mesenteric veins and reach the liver in 30 min [117]. The rapid uptake of Ag_2S QDs conjugated with diabetic drugs, metformin, and nicotinamide mononucleotide, through the small intestine and increased therapeutic potency also confirmed these abilities QDs to translocate the GI tract. The role of coating material in the targeting of QDs was demonstrated in a study by Zhang and coworkers. They observed 17 fold increase in the accumulation of PLGA (poly(lactic-co-glycolic acid) conjugated Ag_2Te QDs when they were packed within a cell vesicle prepared from 4 T1 cells (Fig. 13C-F) [291]. $AgInTe_2$ and Ga-dopped AgInSe QDs packed within a liposome of 1,2-distearoyl-*sn*-glycero-3-phosphocholine (DSPC) were used successfully for biological imaging in animal models [318]. The $AgInS_2$ QDs conjugated with octa-arginine peptides were used to label the adipose tissue-derived stem cells (ASCs) and quantitatively detect their accumulation in the lungs and liver *in vivo* imaging experiments in mouse animal models. The QD-labeled ASCs were transplanted through the tail vein of a mouse, and the PL was detected after 10 min in the lungs and liver of sacrificed animals, with a 40 and 60 % transplantation rate, respectively [292]. The photosensitizer, phthalocyanine conjugated with PEG-capped silicon QDs, was found to accumulate in the tumor cells of a HeLa tumor-bearing mouse [319]. The QD-drug combination was internalized through a biotin-receptor motif and facilitated simultaneous imaging and photodynamic therapy.

4.3. Silicon QDs

Earlier studies used physical methods such as electroporation and microinjection for the cellular delivery of QDs. At the same time, cell-penetrating peptides, bacterial toxins, and viral vectors have been proven to be more efficient in recent reports. Silicon QDs dispersed in phospholipid micelles and surface functionalized with amine or transferrin groups were internalized in the pancreatic cancer cells, while those without functionalization remained in the solution (Fig. 14) [146,320]. Rosso-Vasic *et al.* received similar results [321]; amine-terminated silicon Si QDs were readily taken up and distributed in the cytosol of murine cell line BV2. Another silicon QD showed the selective labeling of endoplasmic reticula of live human umbilical vein endothelial cells with a block copolymer (Pluronic F127) conjugate (Fig. 14) [146]. These results indicate the suitability of silicon QDs in bioimaging and the importance of functionalization on the translocation of QDs [320,321]. The concept of cell-penetrating peptides stemmed from the observation that living cells internalize an 86-amino acid-long fragment from the HIV-1 TAT protein, which binds to the *trans*-acting response element of the viral RNA to transactivate the viral promoter [322]. Tat peptide segment (residues 48–60) derived from this protein has emerged as a novel cell-penetrating peptide for delivering a wide range of therapeutic macromolecules and NPs [323] due to its excellent delivery efficiency and minimal toxicity.

4.4. Copper indium chalcogenide QDs

Low cost, high stability, low cytotoxicity, and great sensitivity make cadmium-free QDs the best for biosensing applications. Copper-based QDs, like the above-discussed ones, are potential candidates for biolabeling and bioimaging due to their versatile surface chemistry, broad absorption bands, narrow emission

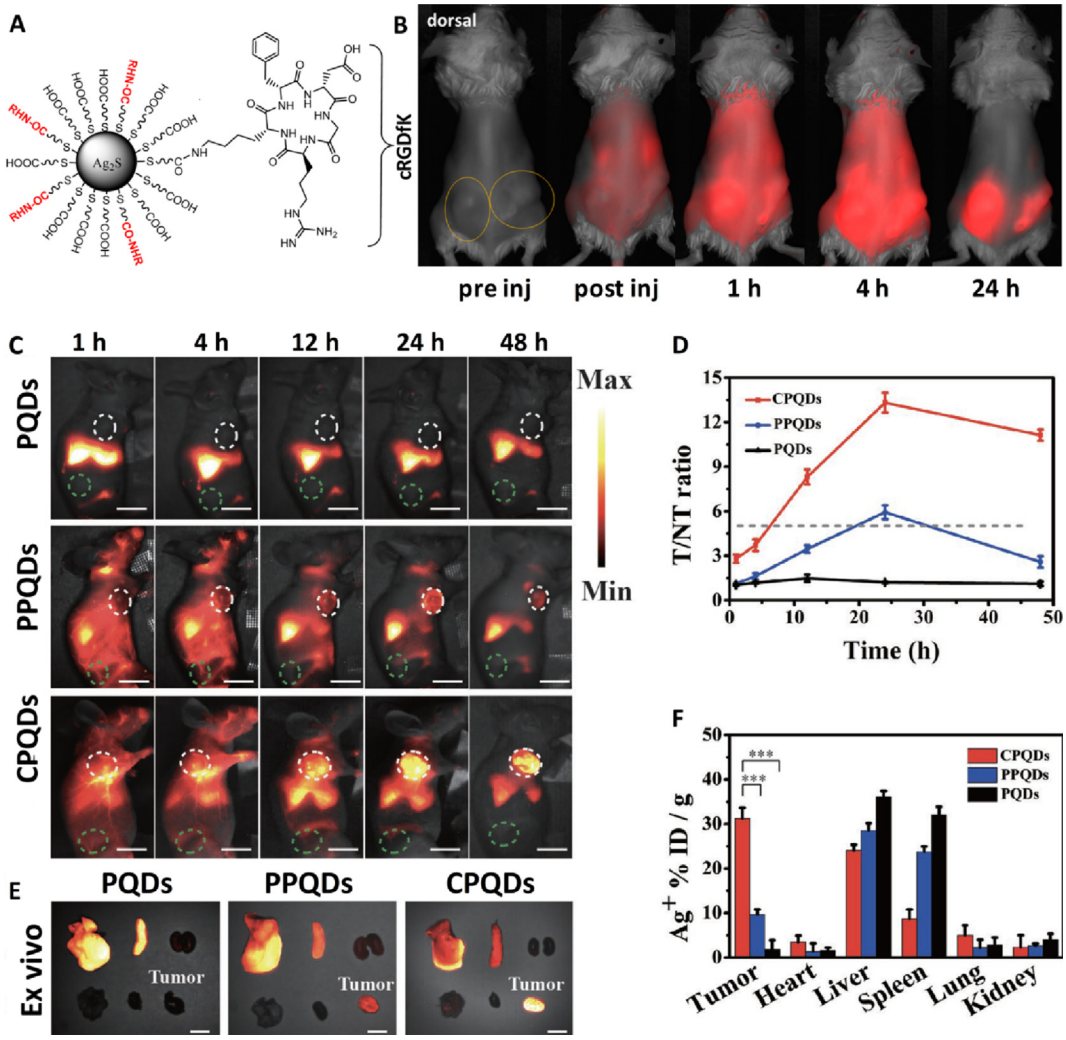

Fig. 13. (A) A scheme of the cRGDfK conjugated Ag_2S QDs. (B) Representative *in vivo* fluorescence images of cRGDfK-Ag_2S in 4T1luc tumor-bearing Balb/c mice at different time points after i.v. administration. Circles indicate bilateral subcutaneous tumor locations. The red color is from the QD. (C) Enhanced *in vivo* tumor imaging with CPQDs. NIR II FL images of 4 T1 tumor-bearing mice injected with PQDs, PPQDs, and CPQDs throughout 48 post-injection. The white and green dashed circles indicate tumor and normal tissue areas. D) The T/NT ratios of the mice. The gray dotted line indicates the Rose criterion. E) *Ex vivo* NIR-II PL data from the tumors and major organs collected from representative mice at 48 h post-injection. F) The biodistribution of the PQDs, PPQDs, and CPQDs at 48 h post-injection. Scale bar: 1 cm. The data points represent mean ± SD (n = 3). Reprinted with permission from Refs. [288,291]. (For interpretation of the references to color in this figure legend, the reader is referred to the web version of this article.)

bands, and photostability. Furthermore, the emission wavelength of copper indium chalcogenides can be tuned from the visible to the NIR region and even the SWIR region, which is extremely useful in bioimaging. Gao and coworkers demonstrated enzyme detection at the molecular level using $CuInS_2$ QDs [324]. For this, the authors initially fabricated water soluble, NIR-absorbable, MPA-capped $CuInS_2$ QDs using the hydrothermal method and subsequently used them for extremely sensitive and selective detection of thrombin using fibrinogen (Fib) in human serum at picomolar levels. The electrostatic interaction and hydrogen bonding between the carboxylic acid group of MPA and the amino groups of fibrinogen resulted in forming of a Fib-$CuInS_2$ QDs complex with enhanced PL intensity and PL peak redshift. The interaction of fibrinogen with thrombin is a crucial stage in blood clotting. Introducing Fib-$CuInS_2$ QDs to thrombin decreases the PL intensity, allowing thrombin detection due to the formation of insoluble fibrillar fibrin-$CuInS_2$ QDs agglutinates. This result is beneficial in detecting disease-related blood coagulation issues.

Similarly, Liu and coworkers used MPA-capped $CuInS_2$ QDs to detect lysozyme [325]. Here, the PL quenching of QDs results from the electrostatic interaction and electron transfer between the QDs and cationic polyelectrolyte poly(dimethyl diallyl ammonium chloride) (PDAD). With the addition of lysozyme aptamer, the PL intensity was recovered to its initial value due to the competitive binding of PDAD and lysozyme aptamer, which suppressed the QD-PDAD contact. Since the interaction was specific to lysozyme over other proteins, it helped in lysozyme-sensitive and -selective detection. Later, Speranskaya and coworkers used $CuInS_2$/ZnS core/shell QDs as a fluorescent marker for quantitative immunoassay investigation of the mycotoxin aflatoxin B1 [326]. They fabricated the organic soluble QDs by hydrophilization using polyethylene glycol (PEG) containing an amphiphilic copolymer. The resulting QDs further conjugated with the aflatoxin B1-protein derivative and subsequently used for fluorescence labeling in a heterogeneous immunoassay to determine the mycotoxin aflatoxin. According to their findings, QD-based immunoassays are more sensitive than enzyme-based immunoassays. Later, An and coworkers used $CuInS_2$ ZnS-SG QDs to sensitively detect cytochrome *c* (Cyt c) [327]. Using the hot reflux approach in an aqueous solution, they initially created negatively charged QDs with good

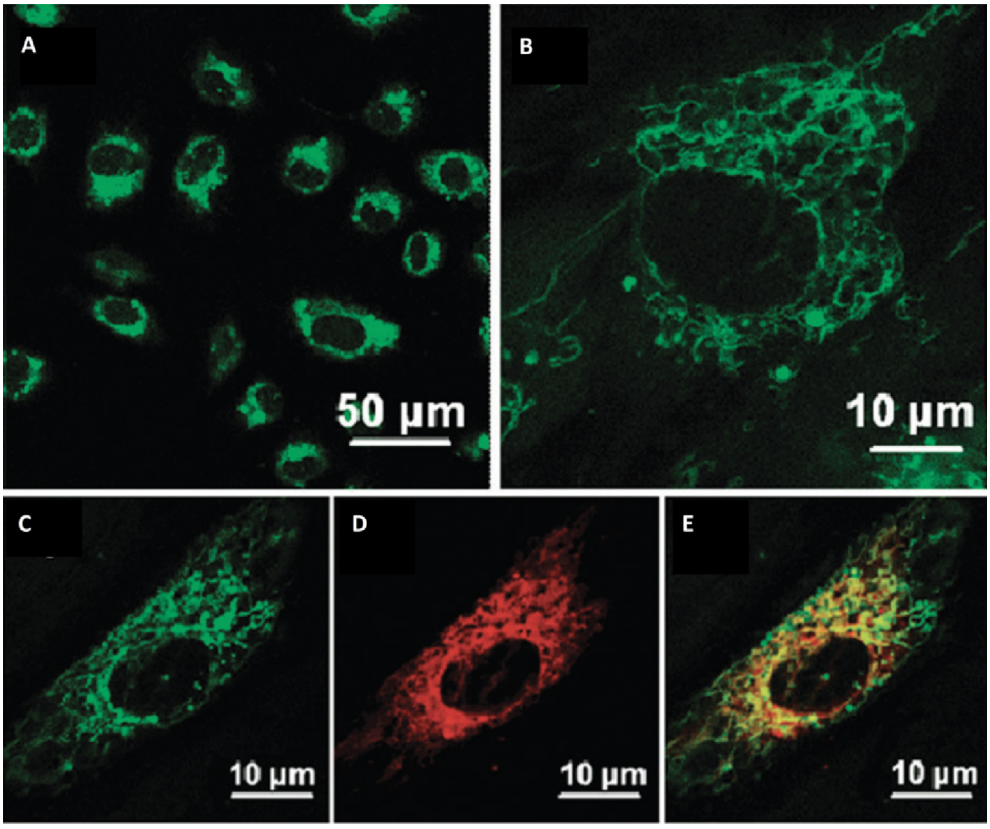

Fig. 14. Confocal laser scanning fluorescence microscope images of live cells labeled with F127-treated Si-QDs. (A) Low and (B) high magnification images, respectively. (C-E) Confocal microscope images of live HUVEC cells labeled with (C) F127-treated Si-QDs, (D) ER-tracker red, and (D) the merged image of (C) and (D). Reprinted with permission from Ref. [146]. (For interpretation of the references to color in this figure legend, the reader is referred to the web version of this article.)

photochemical stability and hydrophilicity. Through thiolated covalent bonding, the -SG moieties were fixed on the surface of QDs. Then, -SG moieties on the surface of QDs were connected to Cyt c utilizing a photo-induced electron transfer technique. The electron transfer process between the electron-deficient heme group in Cyt c and the electron-rich QDs quenched the QD PL intensity. Notably, even in the presence of additional strong interfering proteins such as myoglobin (Mb), hemoglobin (Hb), or bovine serum albumin (BSA), the luminescent $CuInS_2$-ZnS-SG QDs showed high selectivity toward Cyt c. $CuInS_2$-ZnS-SG QDs were also used as probes for imaging HeLa cells, exploring their excellent biocompatibility and low cytotoxicity.

For cell imaging, luminescent $CuInS_2$/ZnS QDs should have several characteristics, including outstanding photochemical stability, excellent water solubility, and tunable particle size. Therefore, rational surface engineering and functionalization of $CuInS_2$/ZnS QDs are highly significant. Several techniques have been proposed in the last few years to make hydrophobic $CuInS_2$/ZnS QDs more water-soluble, including silica coating, ligand exchange, and amphiphilic polymer encapsulation. For example, Foda and coworkers successfully fabricated highly stable and low cytotoxic NIR-emitting $CuInS_2$/ZnS@SiO_2 NPs for cell imaging applications [328]. They adopted encapsulation of hydrophobic $CuInS_2$/ZnS QDs using lipophilic silane micelles by silanization and subsequent sodium silicate deposition in water to achieve such nanoprobes. The resultant $CuInS_2$/ZnS@SiO_2 were bioconjugated with a ligand protein, holo-Transferrin (Tf), for bioimaging. The bioconjugation of $CuInS_2$/ZnS@SiO_2 and Tf was achieved by surface modification of silica surface with an epoxy group (3-glycidyloxypropyl)-trime thoxysilane (GPTMS)-silane coupling in ethanol. The nanoprobe showed enhanced bioavailability; hence, they were successfully used for imaging HeLa cells. Later, Zhao and coworkers fabricated hydrophobic $CuInS_2$/ZnS QDs and phase-transferred them into aqueous solutions for bioimaging applications by employing an effective ligand exchange method using GSH and MPA (Fig. 15) [329]. In another example, Liu and

workers coated amphiphilic BSA-PCL [bovine serum albumin-poly(ε-caprolactone)] bioconjugate to $CuInS_2$/ZnS QDs for bioimaging [330]. Herein, the maleimide-sulfhydryl reaction helped couple BSA and PCL amphiphilic core. Following this, the $CuInS_2$/ZnS QDs were incorporated in the amphiphilic protein-polymer bioconjugate by transferring the QDs into the aqueous phase containing BSA-PCL, providing higher biocompatibility and less toxicity to the QDs. Additionally, they created NIR-luminescent nanoprobes by linking the cyclic Arg-Gly-Asp (cRGD) peptide with BSA-PCL-modified QDs through carbodiimide coupling.

The customized nanoprobe demonstrated remarkable selectivity for the targeted tumor cells overexpressing integrin $\alpha v\beta_3$. Later, Spangler and coworkers introduced a new room temperature, aqueous phase synthetic method for fabricating $CuInS_2$/ZnS core/shell QDs [331]. These QDs were then conjugated with IgG antibodies and used for fluorescent tagging of THP-1 leukemia cells. EGFR receptors overexpressed on THP-1 leukemia cells were tagged using QDs-IgG antibody conjugates made *via* EDC/NHS cross-linking. Confocal fluorescence microscopic investigations helped observe the strong PL from QDs. Mallick and coworkers later created a new multifunctional and tetra-coordinating ligand with a PEG spacer based on lipoic acid and lysine. They employed it for ligand exchange on $CuInS_2$/ZnS QDs. The developed water-soluble QDs exhibited outstanding colloidal stability in solutions and freezing conditions over an extended period [332]. The biotin-binding protein streptavidin (Tr) was conjugated with the

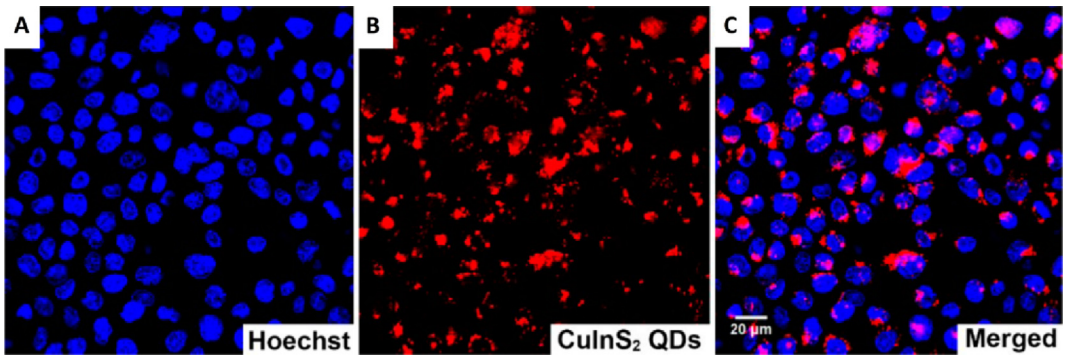

Fig. 15. Confocal fluorescence images of (A) Hoechst labeled nuclei, (B) $CuInS_2$ QDs, and (C) merged images. Adapted with permission from Ref. [329].

carboxylic acid entity of QDs *via* a straightforward carbodiimide coupling procedure. Live-cell imaging of the biotinylated cell surface revealed minimal nonspecific binding of the Tr-conjugated QDs to mammalian cells. Later, employing biocompatible GSH as a capping ligand and stabilizer, Arshad and coworkers established a cost-effective and environmentally safe aqueous synthetic technique for preparing $CuInS_2$ QD [333]. It was bioconjugated with arginyl-glycyl-aspartic acid (RGD) peptide *via* EDC/NHS coupling and employed in bioimaging applications in HeLa cells due to its low cytotoxicity. Later, Dutková and coworkers developed chitosan-capped $CuInS_2$ and $CuInS_2$/ZnS QDs, which they utilized to examine the metabolic activity in several cell lines [334].

Infrared QDs are remarkably relevant for biological imaging due to their tunability in the proper infrared windows like NIR-I (700–1000 nm) and NIR-II (1000–1400 nm) [246]. These QDs provide better tissue penetration and greater spatial and temporal resolutions due to the lower photon absorption and scattering of biological tissues in the infrared regions. They have been used for both *in vitro* and *in vivo* imaging. For instance, Li and coworkers constructed dodecanethiol-tethered $CuInS_2$/ZnS QDs and then transferred them to the aqueous phase by replacing the surface ligand with DHLA. Such QDs were subsequently employed for *in vivo* imaging of mice [335]. Here, QDs were injected intravenously into mice, and it was shown that the QDs accumulated in the liver, spleen, and lungs. A well-known tumor-targeting molecule FA was bioconjugated to highly luminescent and stable PEGylated phospholipid micelle-encapsulated $CuInS_2$/ZnS QDs by Yong and coworkers in the same year. They have been successfully employed for tumor targeting and live animal imaging applications [336]. According to toxicology studies, the micelle-encapsulated QDs were nontoxic to cells or tissues. Later, Kim and coworkers created NIR-emitting $CuInS_2$/ZnS core/shell QDs with a glycol-chitosan coating for *in vivo* imaging applications [337]. Mercaptoundecanoic acid (MUA) was used for ligand exchange with the as-prepared QDs, followed by the EDC/NHS coupling reaction with glycol-chitosan to facilitate aqueous phase transformation. Here, an amide bond was formed between the carboxyl group of the MUA-QDs and the amine terminal of the glycol-chitosan. To accomplish *in vivo* tumor targeting, the integrin binding RGD peptide was covalently attached to the QD surface. In another example, Liu and coworkers stabilized $CuInS_2$/ZnS QDs with Pluronic F127 block copolymer micelles, which increased the colloidal and optical stability of QDs, enabling their *in vitro* and *in vivo* imaging applications [338]. Using ZnS coating, Yu and coworkers prepared highly luminescent $CuInS_2$ QDs at low temperatures while maintaining 50–60% PLQY. It was also transported into the aqueous phase by ligand swapping with DHLA or 11-MUA and bioconjugated with single-domain antibodies (sdAbs). The resultant QDs were utilized for *in vivo* imaging of brain tumors and *in vitro* imaging of pancreatic cancer cells [339]. In the same year, Panthani and coworkers fabricated $CuInSe_xS_{2-x}$/ZnS core/shell QDs loaded poly (lactic-co-glycolic acid) (PLGA) microparticles, which they used for *in vivo* whole animal fluorescence imaging to visualize the deep tissue within the gastrointestinal tract [340]. Later, Lian and coworkers fabricated $CuInSe_2$/ZnS QDs with extremely efficient NIR-II PL (PLQY = 21.8%) for real-time NIR PL imaging (Fig. 16) [341].

4.5. Indium-based binary QDs

Due to their low toxicity, indium-based binary QDs have recently emerged as an excellent nanoprobe in biological applications. Researchers started looking into the possibilities for *in vitro* and *in vivo* imaging applications using indium-based binary QDs. For example, Bharali and coworkers fabricated FA bioconjugated InP/ZnS core/shell QDs for confocal and two-photon bioimaging [342]. To make QDs aqueous soluble, they were initially ligand exchanged with MAA and then bioconjugated with FA *via* DCC coupling between the carboxylic acid moiety of the QDs and amino groups of FA. The QD-FA conjugate was used for bioimaging and demonstrated QD-FA internalization in human nasopharyngeal epidermal carcinoma cells (Fig. 17). Later, Yong *et al.* used highly photostable and biocompatible InP/ZnS core/shell QDs

for *in vitro* pancreatic cell imaging [343]. The cancer-specific monoclonal antibodies such as anticlaudin 4, anti-prostate stem cell antigen, and anti-PSCA were conjugated to the MSA-coated QDs using carbodiimide chemistry for *in vitro* targeted confocal bioimaging. This receptor-mediated targeted labeling and imaging assisted early-state cancer cell detection.

Later, Zhang and coworkers fabricated InP/ZnSe/ZnS QDs with visible and NIR emissions for bioimaging *in vitro* and *in vivo* [344]. Here, the InP core provided the visible excitonic emission, whereas the Zn incorporation and defective ZnSe shell overcoating were responsible for the NIR trap state emission. To make InP/ZnSe/ZnS QDs soluble in aqueous solutions, they employed various phase transfer techniques in which the tumor-targeted imaging potential of the cRGD-modified poly(acrylic acid)-octylamine (PAA-based) amphiphilic polymer wrapped InP/ZnSe/ZnS QDs was greatly improved (Fig. 18). Lim and coworkers recently addressed the

background autofluorescence-PL interference in bioimaging by employing copper-doped InP QDs [345]. The doped QDs showed longer PL lifetimes and larger Stokes shifts. The QDs were swapped with the hydrophilic ligands lipoic acid and zwitterionic lipoic acid (1:1) to make these aqueous soluble. Subsequently, bioconjugation of biotin was accomplished by EDC coupling. The carboxylic acid group of lipoic acid has been extensively used to conjugate QDs with biomolecules. However, regardless of the pH or ionic strength, the quaternary ammonium and sulfonate groups on the zwitterion-containing lipoic acid rendered the

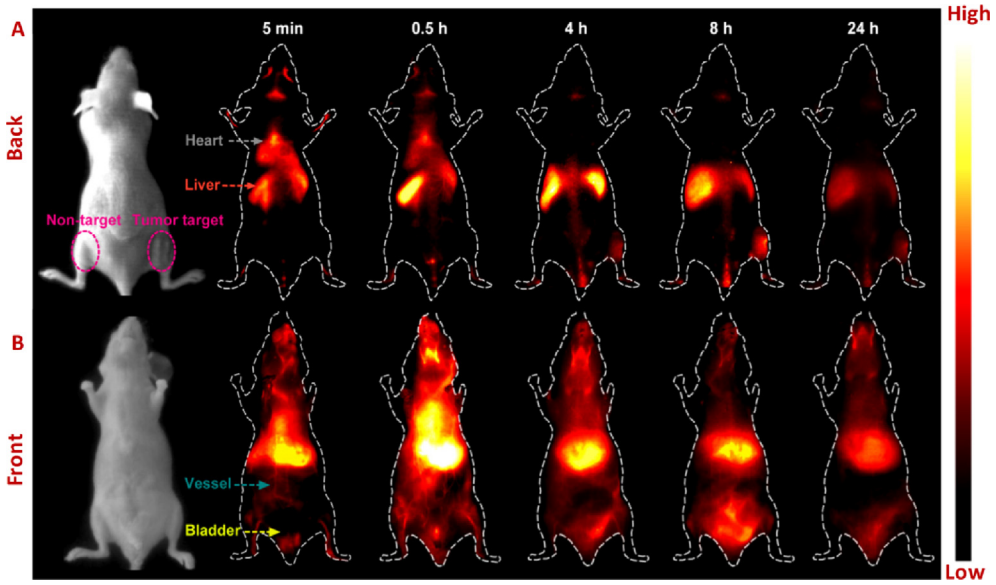

Fig. 16. Brightfield photographs and NIR-II images from (A) the back and (B) the front of tumor-bearing nude mice after i.v. injection of Ab-QDs at different times. Adapted with permission from Ref. [341].

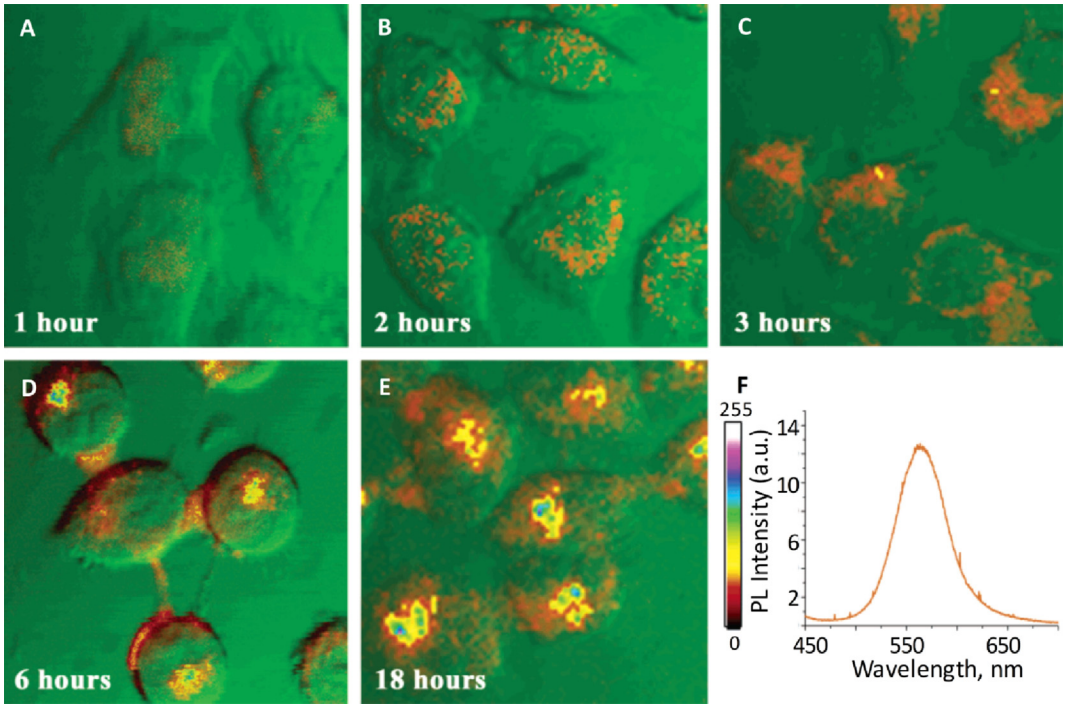

Fig. 17. Confocal images showing fluorescence of QD-FA in KB cells and a localized PL emission spectrum. Here green color shows the transmission data, while the intensity-coded (red to white) channel shows the QD fluorescence. Adapted with permission from Ref. [342]. (For interpretation of the references to color in this figure legend, the reader is referred to the web version of this article.)

QDs with excellent colloidal stability and helped minimize non-specific adsorption of QDs to substrates. These biotin-conjugated Cu-doped InP/ZnS QDs were further used to demonstrate the selective imaging of streptavidin beads. InAs QDs have also been used for bioimaging. Overgrowing shells improved the optical properties InAs QDs and widened the bandgap. For example, Zimmer and coworkers fabricated ZnSe-shelled InAs QDs with NIR emission for *in vivo* imaging of lymph nodes [346]. By using a DHLA-PEG combination in a ligand exchange procedure, these QDs were engineered to be aqueous soluble. The surface functionalized QDs were then intravenously injected into mice and demonstrated *in vivo* imaging. Later, the same research group fabricated NIR (700–900 nm) emitting aqueous-soluble InAs(ZnCdS) core–shell QDs for *in vitro* and *in vivo* imaging [347]. As prepared core–shell QDs were ligand exchanged using amine-functionalized poly(amino-$PEG_{11})_{25\%}$-PIL polymer and the primary amine-containing water-soluble QDs were bioconjugated with streptavidin *via* EDC coupling. After testing in HeLa cells, these QDs were intravenously injected into mice, and tumor vasculature imaging was demonstrated.

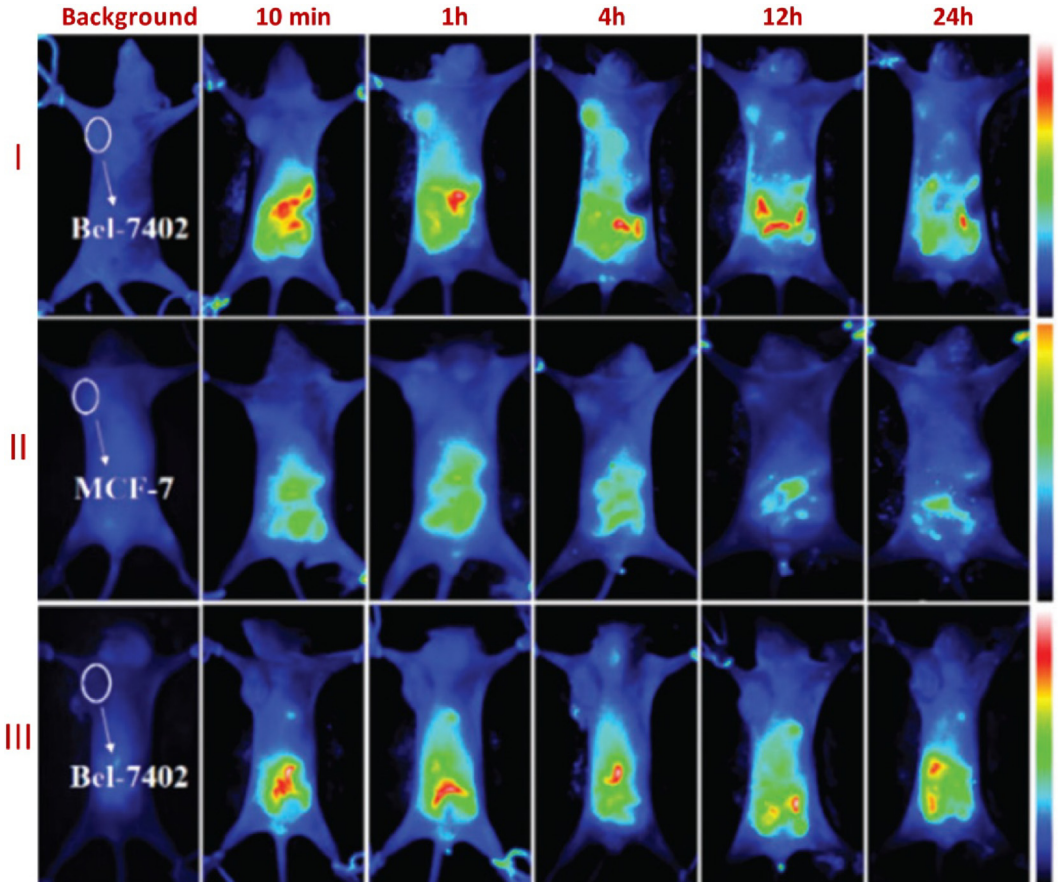

Fig. 18. Dynamic distributions of PAA-based amphiphilic polymer-wrapped InP/ZnSe/ZnS QDs (I and II) with or (III) without cRGD modification after intravenously injected into Bel-7402 tumor-bearing mice or MCF-7 tumor-bearing mice. The tumor sites are outlined in white circles. For each group, color bars are provided, in which the signal strengthens as the color evolves from bottom to top. Adapted with permission from Ref. [344].

5. Toxicity of QDs

Significant progress has been achieved in synthesizing and utilizing cadmium- and lead-based QDs for various applications. However, their practical utilization is limited due to their inherent heavy metal content and toxicity. The pharmacokinetics and toxicity of nanomaterials are determined by physicochemical factors such as size, chemical composition, surface charge, and surface coating. These factors control the biodistribution, degradation, or excretion of QDs [254,255,348,349]. Despite introducing a uniform protecting inorganic shell or polymer coating over the core material for their slow discharge/degradation, toxic metal ions released from these nanocrystals due to photooxidation or poor stability mark a severe threat to the environment [349–353]. Cadmium-based QDs have also shown aggregation while binding to intracellular proteins or membranous structures, generating reactive oxygen species and causing cytotoxicity [5,11,12]. Parak and coworkers investigated the cytotoxicity of CdSe and CdSe/ZnS QDs with coatings of MPA, PEG-silica, and polymer in several cell lines. The release of Cd^{2+} from the core significantly varied in QDs with ZnS, silica, or polymer coating compared to MPA due to different cellular uptake abilities [354]. The precipitation of particles on the cell surface was also found to impair the cells [355]. QDs also found to have prolonged circulating lifetime *in vivo*. The fluorescence images of living mice injected with polymer-coated CdSe/ZnS QDs (PEG-750 and mPEG-5000) showed deposition in the lymph nodes, bone marrow, liver, spleen, and intestines (Fig. 19) [356]. The intravenously injected QDs were retained in these tissues for at least a month. The effect of CdTe QDs on the mitochondrial morphology and structure in HepG2 cells was studied, which showed membrane-potential disruption, increased calcium influx, and impaired cellular respiration due to the release of Cd^{2+} ions [357]. Thus, research is shifting to cadmium- and lead-free semiconductor QDs with minimal toxicity.

The initial studies used QDs bearing toxic heavy metals (Cd, Pb, Hg, etc.) in their core and covered with shells to improve their dispersity and reduce toxicity. In biological systems, the enzymatic action within the cellular environment and hydrographic conditions, including varying pH and salinity, deteriorates the safety coatings and, successively, the core of these QDs. Increased use of heavy metal-based QDs in consumer products such as solar cells, displays, and electronic systems poses long-term health and environmental risks by affecting aquatic life and impairing biogeochemical cycles [11,358,359]. Recent studies indicated that these QDs within the cells (injected for drug delivery or imaging) or in the environment (reaches through effluents or disposal of electronic waste carrying QDs) could lead to the slow release of heavy metals, which can induce toxicities to the ecosystem. Therefore, QDs without heavy metals would be essential for biological applications. The NIR emission spectrum of QDs based on I-III and I-III-VI group elements lift the limitations of biological imaging due to low background signals and excellent tissue penetration. Cell-based assays showed that silver-based QDs are less toxic than heavy metal-based QDs. Indeed, one of the toxicity pathways of heavy metal ions (Cd, Pb, and Hg) is reactive oxygen species generation [223,280,289]. *In vitro* studies in animal cell lines (HeLa,

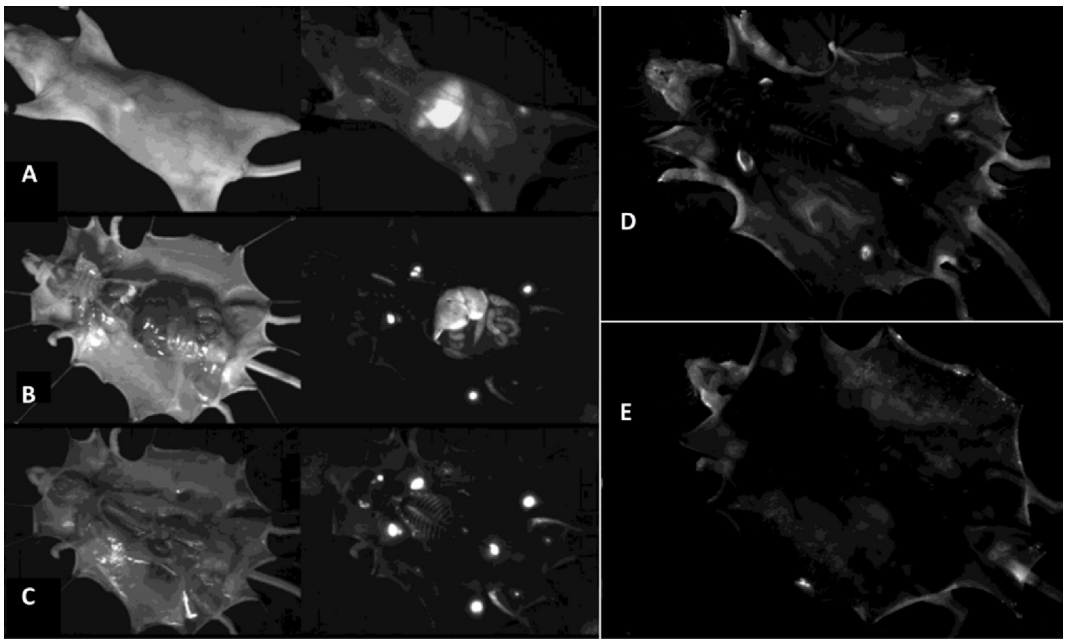

Fig. 19. Mouse imaged 24 h post-injection of 645 nm mPEG750 QDs: (A, B, C – left) brightfield images, (A, B, C – right) fluorescence images. (A) whole animal, (B) skin and peritoneum removed, sternum pinned back showing marrow staining, but concealing cervical nodes, (C) sternum, heart, lungs, liver, and digestive tract removed. QD-staining to (A) axillary and inguinal lymph nodes and (B, C) the bone marrow, lymph nodes, and liver. (D) Mouse imaged 133 days post-injection of mPEG750 QDs. (E) Dissection of the control (un-injected) mouse. Mice were imaged under identical conditions, and images were displayed using similar brightness functions. Reprinted with permission from Ref. [356].

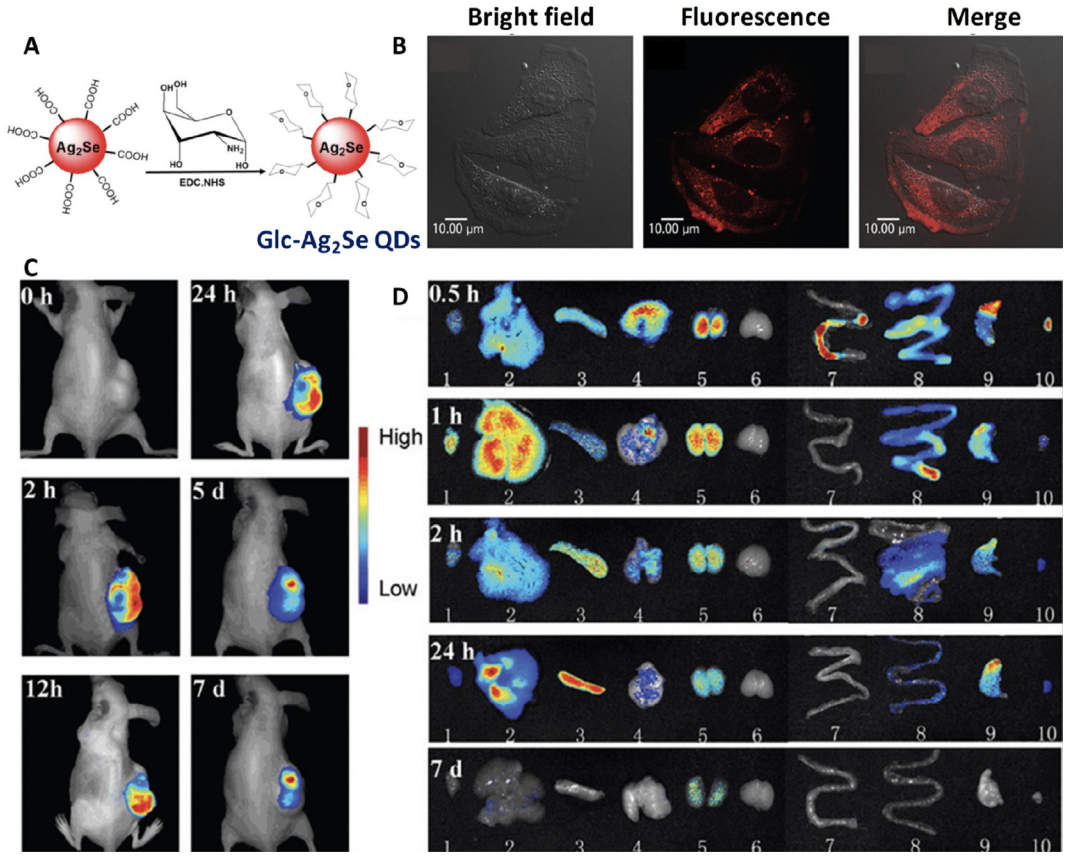

Fig. 20. (A) A scheme of EDC conjugation of Glucose-Ag_2Se QDs. (B) Laser scanning confocal imaging of MCF-7 cells incubated with Glc-Ag_2Se QDs or controls (C) Images of nude mice bearing MCF7 tumor after intravenous injection of glucose- Ag_2Se QDs *in vivo.* (D) Organs dissected from the animal after different time intervals to show the clearing of injected QDs. The heart (1), liver (2), spleen (3), lungs (4), kidney (5), brain (6), large intestine (7), stomach (9), and urinary bladder (10) are numbered. Reprinted with permission from Ref [290].

A549, and BHK21) showed that more than 75% of these cells could survive in the presence of 100 μg mL^{-1} concentration of $AgInSe_2$ QDs [360]. The Tat peptide conjugated Ag_2S QDs reported by Chen *et al.* was used for dynamic tracking of human bone marrow mesenchymal stem cells without inducing ROS production or any toxicity to the proliferation and differentiation of stem cells [361]. $AgInS_2$ QDs and their modified forms with Zn and octa-arginine peptides are less toxic than cadmium-based QDs to adipose tissue-derived stem cells (ASCs). $AgInS_2$ QDs were also not found to produce inflammatory cytokines [292].

In vivo studies have shown that silver-based QDs injected into animals accumulate in the primary excretion routes, such as the liver and kidney, indicating the possibility of a clearing [288]. The glucose-conjugated Ag_2Se QDs injected intraperitoneally into the tail region of the mouse were distributed to the spleen, kidneys, and liver within two h of injection and were primarily cleared in 24 h (Fig. 20) [290]. No signals of silver were detected in the ICP-MS analysis of samples collected on the 7th day of the experiment. The *in vivo* biodistribution study of Si QDs radio labeled with positron-emitting tracer (PET) showed that dextran-coated Si QDs are rapidly cleared from the mouse bloodstream and that the QDs were excreted *via* renal filtration [362]. Silicon QDs are nontoxic, and the silicic acid produced during the degradation is easily excreted through the urine [145,363].

Copper indium chalcogenides have emerged as a promising candidate due to their near-complete compliance with the requirements for usage as a biological contrast agent and their relatively low toxicity. Numerous studies indicate that both conjugated and non-conjugated $CuInS_2$/ZnS core/shell QDs do not affect cell viability and are generally non-toxic [364–368]. Speranskaya and coworkers examined the cytotoxicity and hemocompatibility of $CuInS_2$/ZnS core/shell QDs with various polymeric shells to address biocompatibility [364]. Confocal microscopy analyses of $CuInS_2$/ZnS core–shell QDs revealed cell penetration, and a trypan blue staining assay revealed negligible toxicity. The hemocompatibility

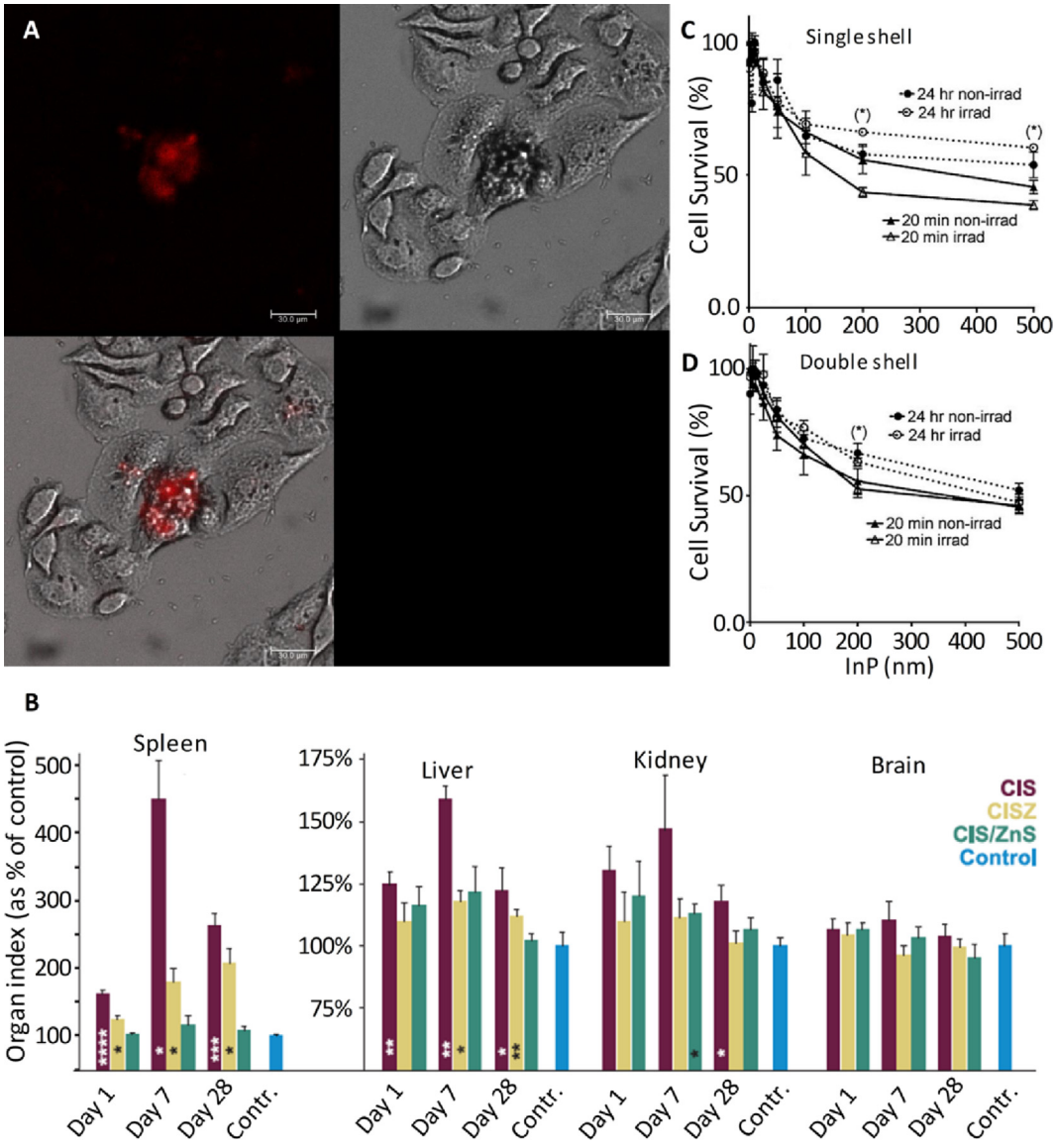

Fig. 21. (A) Confocal laser scanning fluorescence microscopy images showing human HEP2 carcinoma cells labeled with CIS/QDs covered with PMAO-Jeffamine M1000 polymer. (B) Organ index (organ weight/total body weight) plotted as the percent of control values for four major organs. Error bars are standard deviations. (C and D) Direct comparison of cytotoxicity assays after 20 min (triangles) *vs.* 24 h (circles) of incubation with QDs. The lines guide the eye: dashed lines indicate the 24 h incubation times. (C) Single-shell InP QDs. (D) Double-shell InP QDs. Reprinted with permission from Refs. [364,366,369].

assays significantly rely on the QD surface. The experiments showed that the hydrophilic shells of QD were intact, confirming their hemocompatibility (Fig. 21A). Furthermore, PEGylated $CuInS_2$/ZnS

core/shell QDs showed excellent biocompatibility and low toxicity in BALB/c mice [365]. Recent research by Kays and coworkers compared the toxicity of $CuInS_2$/ZnS core–shell QDs, and shell-free $CuInS_2$ QDs encapsulated in an amphiphilic lipid polymer [366]. Notably, significant *in vivo* toxicity was brought on by releasing harmful ions from the shell-free QDs. On the other hand, the ZnS shell prevented the core degradation, making the system more biocompatible (Fig. 21B). Later, Chen and coworkers investigated the *in vivo* imaging potential using *Caenorhabditis elegans* models and O-carboxymethyl chitosan coated on top of the shell-free and core–shell QDs [367]. Even after 96 h exposure, the QDs exhibited excellent chemical stability and no toxicity. Further, Liu and coworkers investigated developmental toxicity of $CuInS_2$/ZnS QDs in Chinese rare minnow (Gobiocypris rarus) embryos [368]. They found the $CuInS_2$/ZnS core/shell QDs potentially toxic to G. rarus embryos, causing DNA damage and decreased survival rates.

Developing indium-based binary QDs emerged as a non-toxic substitute for heavy metal-based QDs. Chibli and coworkers used reactive oxygen species assays to evaluate the toxicity of InP QDs [369]. They were able to establish that superoxide was the primary contributor to the toxicity of InP QDs. However, the InP QDs shelled with ZnS could significantly reduce the toxicity by trapping the photogenerated charges in the core and reducing their interaction with electrolytic media (Fig. 21C, D). Later, Brunetti and coworkers examined the toxicity of InP/ZnS and CdSe/ZnS core/shell QDs *in vitro* and *in vivo* and found that InP/ZnS QDs are safer than heavy metal-based QDs [13]. The *in vivo* investigations employing the drosophila model and *in vitro* cell culture studies showed that InP/ZnS QDs have significantly lower intrinsic toxicity. Recently, Jalali and coworkers used the MTT assay, LDH assay, DAPI, and actin staining to test the cell viability and biocompatibility of InP/ZnO and InP/ZnS films on neuro2A cells [370,371]. The results showed no impact on cell viability, membrane integrity, or morphology. The highly toxic arsenic ions may cause cell death even at low doses [372]. Therefore, a comprehensive evaluation of the toxicity of InAs QDs is necessary.

6. Summary and prospects

Since 1998, semiconductor quantum dots have emerged as the most promising luminescent probes for bioimaging. Further, bioconjugate chemistry, cell biology, biochemistry, pharmacology, bioimaging technologies, and biomedicine helped formulate quantum dots into integral parts of modern bioimaging. The versatile surface chemistry and tunable bandgap of quantum dots have been the keys accompanying these tiny crystals to bioimaging and biosensing. This review systematically introduces significant progress in the synthesis, surface modification, and absorption and photoluminescence properties of core-only and core–shell quantum dots based on cadmium-, lead-, copper-, silver-, indium- and silicon, which is accompanied by the introduction of various functional groups and biomolecules to the quantum dot surface through bioconjugate reactions. The later half of the review focuses on various biological applications such as biomolecular detections, cell membrane labeling and imaging, cancer marker-specific cell labeling and imaging, intracellular delivery and imaging, multimodal *in vivo* imaging, and visible- and NIR *in vivo* imaging. The final part focuses on the cytotoxicity and pharmacokinetics of various quantum dots.

Although several methods have been introduced to synthesize luminescent quantum dots, high-quality ones are prepared by high-temperature colloidal methods by temporally and thermally separating the crystal nucleation and growth processes. Despite the heavy metal-based toxicity of Cd- or Pb-based quantum dots, early reports about these materials helped advance the field. Nevertheless, more recently developed silver-, copper- and indium-based quantum dots are more promising for biomedical applications than Cd-/Pb-based quantum dots due to their large two-photon absorption cross-section and near-infrared emission. Although bare QDs and other nanoparticles can be used for bioimaging, specific applications such as targeted imaging, diagnosis, drug delivery and therapy require modifying the quantum dot surface with a shell, small molecules having reactive functional groups, and biomolecules such as aptamers, hormones, ligands, peptides, or antibodies [373–376]. This review also provides insights into different biomolecules attached to quantum dots for targeted imaging. Even though high-quality core–shell quantum dots and ready-to-use quantum dot bioconjugates have been commercially available and extensively tested for bioimaging of cells and animal models for over a decade, clinical trials of quantum dots are still in their infancy. The missing links between quantum dots and biomedicine are the development of high-quality non-toxic quantum dots emitting in the first and second biological windows and the rationalization of their long-term pharmacokinetics.

Data availability

No data was used for the research described in the article.

Declaration of Competing Interest

The authors declare that they have no known competing financial interests or personal relationships that could have appeared to influence the work reported in this paper.

Acknowledgments

V. B. acknowledges a MEXT-JSPS Grant-in-Aid for Scientific Research B (23H01781), the Hokkaido University Photoexcitonix Program and the Crossover Alliance to Create the Future with People, Intelligence and Materials. A. A. is thankful to the financial support from CSIR under the E3OW scheme for MLP2013. E.S.S. thankful to the Science and Engineering Research Board (SERB) for a Ramanujan Fellowship (SB/S2/RJN-005/2017) and a Startup Research Grant (SRG/2022/586). J. S. acknowledges a Hokkaido University DX doctoral Scholarship.

References

[1] A.I. Ekimov, Exciton absorption by copper(I) chloride crystals in a glassy matrix, Fiz. i Khimiya Stekla. 6 (1980) 511–512.
[2] L.E. Brus, A simple model for the ionization potential, electron affinity, and aqueous redox potentials of small semiconductor crystallites, J. Chem. Phys. 79 (1983) 5566–5571, https://doi.org/10.1063/1.445676.
[3] M. Bruchez, M. Moronne, P. Gin, S. Weiss, A.P. Alivisatos, Semiconductor nanocrystals as fluorescent biological labels, Science 281 (1998) 2013–2016, https://doi.org/10.1126/science.281.5385.2013.
[4] C.B. Murray, D.J. Norris, M.G. Bawendi, Synthesis and characterization of nearly monodisperse CdE (E = sulfur, selenium, tellurium) semiconductor nanocrystallites, J. Am. Chem. Soc. 115 (1993) 8706–8715, https://doi.org/10.1021/ja00072a025.
[5] D. Mo, L. Hu, G. Zeng, G. Chen, J. Wan, Z. Yu, Z. Huang, K. He, C. Zhang, M. Cheng, Cadmium-containing quantum dots: Properties, applications, and toxicity, Appl. Microbiol. Biotechnol. 101 (2017) 2713–2733, https://doi.org/10.1007/s00253-017-8140-9.
[6] D. Vasudevan, R.R. Gaddam, A. Trinchi, I. Cole, Core-shell quantum dots: Properties and applications, J. Alloys Compd. 636 (2015) 395–404, https://doi.org/10.1016/j.jallcom.2015.02.102.
[7] A.R. Loukanov, C.D. Dushkin, K.I. Papazova, A.V. Kirov, M.V. Abrashev, E. Adachi, Photoluminescence depending on the ZnS shell thickness of CdS/ZnS core-shell semiconductor nanoparticles, Colloids Surf. A Physicochem. Eng. Asp. 245 (2004) 9–14, https://doi.org/10.1016/j.colsurfa.2004.06.016.

[8] L. Qi, J. Ma, H. Cheng, Z. Zhao, Synthesis and characterization of mixed CdS/ZnS nanoparticles in reverse micelles, Colloids Surf. A Physicochem. Eng. Asp. 111 (1996) 195–202, https://doi.org/10.1016/0927-7757(96)03545-5.
[9] B.O. Dabbousi, J. Rodriguez-Viejo, F.V. Mikulec, J.R. Heine, H. Mattoussi, R. Ober, K.F. Jensen, M.G. Bawendi, (CdSe)ZnS core-shell quantum dots: Synthesis and characterization of a size series of highly luminescent nanocrystallites, J. Phys. Chem. B. 101 (1997) 9463–9475, https://doi.org/10.1021/jp971091y.
[10] Z. Zeng, C.S. Garoufalis, A.F. Terzis, S. Baskoutas, Linear and nonlinear optical properties of ZnO/ZnS and ZnS/ZnO core shell quantum dots: Effects of shell thickness, impurity, and dielectric environment, J. Appl. Phys. 114 (2013), https://doi.org/10.1063/1.4813094.
[11] Y. Liang, T. Zhang, M. Tang, Toxicity of quantum dots on target organs and immune system, J Appl. Toxicol. 42 (2022) 17–40, https://doi.org/10.1002/jat.4180.
[12] J. Sobhanan, P. Jones, R. Kohara, S. Sugino, M. Vacha, C. Subrahmanyam, Y. Takano, F. Lacy, V. Biju, Toxicity of nanomaterials due to photochemical degradation and the release of heavy metal ions, Nanoscale 12 (2020) 22049–22058, https://doi.org/10.1039/D0NR03957H.
[13] V. Brunetti, H. Chibli, R. Fiammengo, A. Galeone, M.A. Malvindi, G. Vecchio, R. Cingolani, J.L. Nadeau, P.P. Pompa, InP/ZnS as a safer alternative to CdSe/ZnS core/shell quantum dots: In vitro and in vivo toxicity assessment, Nanoscale 5 (2013) 307–317, https://doi.org/10.1039/C2NR33024E.
[14] H.B. Jalali, S. Sadeghi, I.B. Dogru Yuksel, A. Onal, S. Nizamoglu, Past, present and future of indium phosphide quantum dots, Nano Res. 15 (2022) 4468–4489, https://doi.org/10.1007/s12274-021-4038-z.
[15] J. Li, K. Pu, Semiconducting polymer nanomaterials as near-infrared photoactivatable protherapeutics for cancer, Acc. Chem. Res. 53 (2020) 752–762, https://doi.org/10.1021/acs.accounts.9b00569.
[16] S. Chinnathambi, S. Chen, S. Ganesan, N. Hanagata, Silicon quantum dots for biological applications, Adv. Healthc. Mater. 3 (2014) 10–29, https://doi.org/10.1002/adhm.201300157.
[17] S.A. McDonald, G. Konstantatos, S. Zhang, P.W. Cyr, E.J.D. Klem, L. Levina, E.H. Sargent, Solution-processed PbS quantum dot infrared photodetectors and photovoltaics, Nature Mater. 4 (2005) 138–142, https://doi.org/10.1038/nmat1299.
[18] X.-B. Li, C.-H. Tung, L.-Z. Wu, Semiconducting quantum dots for artificial photosynthesis, Nat. Rev. Chem. 2 (2018) 160–173, https://doi.org/10.1038/s41570-018-0024-8.
[19] V.I. Klimov, A.A. Mikhailovsky, S. Xu, A. Malko, J.A. Hollingsworth, C.A. Leatherdale, H.-J. Eisler, M.G. Bawendi, Optical gain and stimulated emission in nanocrystal quantum dots, Science 290 (2000) 314–317, https://doi.org/10.1126/science.290.5490.314.
[20] C.-Y. Lu, J.-W. Pan, Quantum-dot single-photon sources for the quantum internet, Nat. Nanotechnol. 16 (2021) 1294–1296, https://doi.org/10.1038/s41565-021-01033-9.
[21] A. Smith, H. Duan, A. Mohs, S. Nie, Bioconjugated quantum dots for in vivo molecular and cellular imaging, Adv. Drug Deliv. Rev. 60 (2008) 1226–1240, https://doi.org/10.1016/j.addr.2008.03.015.
[22] V. Biju, Chemical modifications and bioconjugate reactions of nanomaterials for sensing, imaging, drug delivery and therapy, Chem. Soc. Rev. 43 (2014) 744–764, https://doi.org/10.1039/C3CS60273G.
[23] Y. Chen, Y. Jiang, Z. Zhang, C. Wang, X. Liu, Synthesis spectrum properties of high-quality CdS quantum dots, J Nanosci. Nanotechnol. 10 (2010) 6544–6549, https://doi.org/10.1166/jnn.2010.2642.
[24] A.M. Smith, H. Duan, M.N. Rhyner, G. Ruan, S. Nie, A systematic examination of surface coatings on the optical and chemical properties of semiconductor quantum dots, Phys. Chem. Chem. Phys. 8 (2006) 3895, https://doi.org/10.1039/b606572b.
[25] S. Mussa Farkhani, A. Valizadeh, Review: Three synthesis methods of CdX (X = Se, S or Te) quantum dots, IET Nanobiotechnol. 8 (2014) 59–76, https://doi.org/10.1049/iet-nbt.2012.0028.
[26] Y.C. Cao, J. Wang, One-pot synthesis of high-quality zinc-blende CdS nanocrystals, J. Am. Chem. Soc. 126 (2004) 14336–14337, https://doi.org/10.1021/ja0459678.
[27] D.V. Talapin, A.L. Rogach, A. Kornowski, M. Haase, H. Weller, Highly luminescent monodisperse CdSe and CdSe/ZnS nanocrystals synthesized in a hexadecylamine-trioctylphosphine oxide-trioctylphospine mixture, Nano Lett. 1 (2001) 207–211, https://doi.org/10.1021/nl0155126.
[28] D.C. Onwudiwe, M. Hrubaru, E.E. Ebenso, Synthesis, structural and pptical properties of TOPO and HDA capped cadmium sulphide nanocrystals, and the effect of capping ligand concentration, J. Nanomater. 2015 (2015) 1–9, https://doi.org/10.1155/2015/143632.
[29] C.R. Bullen, P. Mulvaney, Nucleation and growth kinetics of CdSe nanocrystals in octadecene, Nano Lett. 4 (2004) 2303–2307, https://doi.org/10.1021/nl0496724.
[30] Z.A. Peng, X. Peng, Formation of high-quality CdTe, CdSe, and CdS nanocrystals using CdO as precursor, J. Am. Chem. Soc. 123 (2001) 183–184, https://doi.org/10.1021/ja003633m.
[31] R. Lai, C. Pu, X. Peng, On-surface reactions in the growth of high-quality CdSe nanocrystals in nonpolar solutions, J. Am. Chem. Soc. 140 (2018) 9174–9183, https://doi.org/10.1021/jacs.8b04743.
[32] L. Manna, D.J. Milliron, A. Meisel, E.C. Scher, A.P. Alivisatos, Controlled growth of tetrapod-branched inorganic nanocrystals, Nature Mater. 2 (2003) 382–385, https://doi.org/10.1038/nmat902.
[33] J. Van Embden, P. Mulvaney, Nucleation and growth of CdSe nanocrystals in a binary ligand system, Langmuir 21 (2005) 10226–10233, https://doi.org/10.1021/la0510811.
[34] N.T.K. Thanh, N. Maclean, S. Mahiddine, Mechanisms of nucleation and growth of nanoparticles in solution, Chem. Rev. 114 (2014) 7610–7630, https://doi.org/10.1021/cr400544s.
[35] S.F. Wuister, A. Meijerink, Synthesis and luminescence of (3-mercaptopropyl)-trimethoxysilane capped CdS quantum dots, J. Lumin. 102–103 (2003) 338–343, https://doi.org/10.1016/S0022-2313(02)00525-2.
[36] N. Ben Brahim, M. Poggi, N.B. Haj Mohamed, R. Ben Chaâbane, M. Haouari, M. Negrerie, H. Ben Ouada, Synthesis, characterization and spectral temperature-dependence of thioglycerol-CdSe nanocrystals, J. Lumin. 177 (2016) 402–408, https://doi.org/10.1016/j.jlumin.2016.05.026.
[37] Y.-F. Liu, J.-S. Yu, Selective synthesis of CdTe and high luminescence CdTe/CdS quantum dots: The effect of ligands, J. Colloid Interface Sci. 333 (2009) 690–698, https://doi.org/10.1016/j.jcis.2009.01.008.
[38] X.L. Rong, Q. Zhao, G.H. Tao, Aqueous synthesis of CdSe and CdSe/CdS quantum dots with controllable introduction of Se and S sources, Chin. Chem. Lett. 23 (2012) 961–964, https://doi.org/10.1016/j.cclet.2012.05.029.
[39] M.-J. Almendral-Parra, Á. Alonso-Mateos, S. Sánchez-Paradinas, J.F. Boyero-Benito, E. Rodríguez-Fernández, J.J. Criado-Talavera, Procedures for controlling the size, structure and optical properties of CdS quantum dots during synthesis in aqueous solution, J. Fluoresc. 22 (2012) 59–69, https://doi.org/10.1007/s10895-011-0930-3.
[40] J.J. Buckley, E. Couderc, M.J. Greaney, J. Munteanu, C.T. Riche, S.E. Bradforth, R. L. Brutchey, Chalcogenol ligand toolbox for CdSe nanocrystals and their influence on exciton relaxation pathways, ACS Nano. 8 (2014) 2512–2521, https://doi.org/10.1021/nn406109v.
[41] B.R.C. Vale, R.S. Mourão, J. Bettini, J.C.L. Sousa, J.L. Ferrari, P. Reiss, D. Aldakov, M.A. Schiavon, Ligand induced switching of the band alignment in aqueous synthesized CdTe/CdS core/shell nanocrystals, Sci. Rep. 9 (2019) 8332, https://doi.org/10.1038/s41598-019-44787-y.
[42] W.N. Wenger, F.S. Bates, E.S. Aydil, Functionalization of cadmium selenide quantum dots with poly(ethylene glycol): Ligand exchange, surface coverage, and dispersion stability, Langmuir 33 (2017) 8239–8245, https://doi.org/10.1021/acs.langmuir.7b01924.
[43] D.R. Larson, W.R. Zipfel, R.M. Williams, S.W. Clark, M.P. Bruchez, F.W. Wise, W.W. Webb, Water-soluble quantum dots for multiphoton fluorescence imaging in vivo, Science 300 (2003) 1434–1436, https://doi.org/10.1126/science.1083780.
[44] F. Dubois, B. Mahler, B. Dubertret, E. Doris, C. Mioskowski, A versatile strategy for quantum dot ligand exchange, J. Am. Chem. Soc. 129 (2007) 482–483, https://doi.org/10.1021/ja067742y.
[45] S. Basiruddin, A. Saha, N. Pradhan, N.R. Jana, Advances in coating chemistry in deriving soluble functional nanoparticle, J. Phys. Chem. C. 114 (2010) 11009–11017, https://doi.org/10.1021/jp100844d.
[46] N. Gaponik, D.V. Talapin, A.L. Rogach, K. Hoppe, E.V. Shevchenko, A. Kornowski, A. Eychmüller, H. Weller, Thiol-capping of CdTe nanocrystals: An alternative to organometallic synthetic routes, J. Phys. Chem. B. 106 (2002) 7177–7185, https://doi.org/10.1021/jp025541k.
[47] G. Manfredi, P. Lova, F. Di Stasio, R. Krahne, D. Comoretto, Directional fluorescence spectral narrowing in all-polymer microcavities doped with CdSe/CdS dot-in-rod nanocrystals, ACS Photonics 4 (2017) 1761–1769, https://doi.org/10.1021/acsphotonics.7b00330.
[48] S.-H. Choi, H. Song, I.K. Park, J.-H. Yum, S.-S. Kim, S. Lee, Y.-E. Sung, Synthesis of size-controlled CdSe quantum dots and characterization of CdSe-conjugated polymer blends for hybrid solar cells, J. Photochem. Photobiol. A: Chem. 179 (2006) 135–141, https://doi.org/10.1016/j.jphotochem.2005.08.004.
[49] S. Chinnathambi, N. Hanagata, Photostability of quantum dot micelles under ultraviolet irradiation, Luminescence 34 (2019) 472–479, https://doi.org/10.1002/bio.3618.
[50] M.S. Hosseini, M. Kamali, Synthesis and characterization of aspartic acid-capped CdS/ZnS quantum dots in reverse micelles and its application to Hg(II) determination, J. Lumin. 167 (2015) 51–58, https://doi.org/10.1016/j.jlumin.2015.06.009.
[51] T.-D. Nguyen, W.Y. Hamad, M.J. MacLachlan, CdS quantum dots encapsulated in chiral nematic mesoporous silica: New iridescent and luminescent materials, Adv. Funct. Mater. 24 (2014) 777–783, https://doi.org/10.1002/adfm.201302521.
[52] Y.-J. Yang, X. Tao, Q. Hou, J.-F. Chen, Fluorescent mesoporous silica nanotubes incorporating CdS quantum dots for controlled release of ibuprofen, Acta Biomaterialia. 5 (2009) 3488–3496, https://doi.org/10.1016/j.actbio.2009.05.002.
[53] X. Hu, X. Gao, Silica-polymer dual layer-encapsulated quantum dots with remarkable stability, ACS Nano 4 (2010) 6080–6086, https://doi.org/10.1021/nn1017044.
[54] D.-W. Deng, J.-S. Yu, Y. Pan, Water-soluble CdSe and CdSe/CdS nanocrystals: A greener synthetic route, J. Colloid Interface Sci. 299 (2006) 22–232, https://doi.org/10.1016/j.jcis.2006.01.066.
[55] H. Peng, L. Zhang, C. Soeller, J. Travas-Sejdic, Preparation of water-soluble CdTe/CdS core/shell quantum dots with enhanced photostability, J. Lumin. 127 (2007) 721–726, https://doi.org/10.1016/j.jlumin.2007.04.007.
[56] Z. Wu, Y. Zhao, F. Qiu, Y. li, S. Wang, B. Zhang, B. Yang, Y. Zhang, R. Gao, J. Wang, Synthesis and characterization of water-soluble, stable and highly luminescent itaconic acid/methacrylic acid copolymer-coated CdSe/CdS

quantum dots, J. Lumin. 129 (2009) 1125-1131. https://doi.org/10.1016/j.jlumin.2009.05.014
[57] Z. Li, C. Dong, L. Tang, X. Zhu, H. Chen, J. Ren, Aqueous synthesis of CdTe/CdS/ZnS quantum dots and their optical and chemical properties, Luminescence 26 (2011) 439–448, https://doi.org/10.1002/bio.1250.
[58] Y. Bao, J. Li, Y. Wang, L. Yu, J. Wang, W. Du, L. Lou, Z. Zhu, H. Peng, J. Zhu, Preparation of water soluble CdSe and CdSe/CdS quantum dots and their uses in imaging of cell and blood capillary, Opt. Mater. 34 (2012) 1588–1592, https://doi.org/10.1016/j.optmat.2012.03.033.
[59] Zhimin Yuan, J. Wang, P. Yang, Highly luminescent CdTe/CdS/ZnO core/shell/shell quantum dots fabricated using an aqueous strategy, Luminescence 28 (2013) 169-175. https://doi.org/10.1002/bio.2358.
[60] F. Wei, X. Lu, Y. Wu, Z. Cai, L. Liu, P. Zhou, Q. Hu, Synthesis of highly luminescent CdTe/CdS/ZnS quantum dots by a one-pot capping method, J. Chem. Eng. 226 (2013) 416–422, https://doi.org/10.1016/j.cej.2013.04.027.
[61] W.W. Yu, E. Chang, R. Drezek, V.L. Colvin, Water-soluble quantum dots for biomedical applications, Biochem. Biophys. Res. Commun. 348 (2006) 781–786, https://doi.org/10.1016/j.bbrc.2006.07.160.
[62] P. Samokhvalov, M. Artemyev, I. Nabiev, Basic principles and current trends in colloidal synthesis of highly luminescent semiconductor nanocrystals, Chem. Eur. J. 19 (2013) 1534–1546, https://doi.org/10.1002/chem.201202860.
[63] H. He, M. Feng, J. Hu, C. Chen, J. Wang, X. Wang, H. Xu, J.R. Lu, Designed short RGD peptides for one-pot aqueous synthesis of integrin-binding CdTe and CdZnTe quantum dots, ACS Appl. Mater. Interfaces 4 (2012) 6362–6370, https://doi.org/10.1021/am3020108.
[64] A.L. Rogach, T. Franzl, T.A. Klar, J. Feldmann, N. Gaponik, V. Lesnyak, A. Shavel, A. Eychmüller, Y.P. Rakovich, J.F. Donegan, Aqueous synthesis of thiol-capped CdTe nanocrystals: State-of-the-art, J. Phys. Chem. C. 111 (2007) 14628–14637, https://doi.org/10.1021/jp072463y.
[65] S.F. Wuister, C. de Mello Donegá, A. Meijerink, Influence of thiol capping on the exciton luminescence and decay kinetics of CdTe and CdSe quantum dots, J. Phys. Chem. B. 108 (2004) 17393–17397, https://doi.org/10.1021/jp047078c.
[66] Y. Jiang, H. Shao, H. Xu, J. Yang, Y. Wang, H. Xiong, P. Wang, X. Wang, Ultrafast synthesis of near-infrared-emitting aqueous CdTe/CdS quantum dots with high fluorescence, Mater. Today Chem. 20 (2021), https://doi.org/10.1016/j.mtchem.2021.100447.
[67] W.-C. Law, K.-T. Yong, I. Roy, H. Ding, R. Hu, W. Zhao, P.N. Prasad, Aqueous-phase synthesis of highly luminescent CdTe/ZnTe core/shell quantum dots optimized for targeted bioimaging, Small 5 (2009) 1302–1310, https://doi.org/10.1002/smll.200801555.
[68] J. Wang, Y. Long, Y. Zhang, X. Zhong, L. Zhu, Preparation of highly luminescent CdTe/CdS core/shell quantum dots, ChemPhysChem 10 (2009) 680–685, https://doi.org/10.1002/cphc.200800672.
[69] M. Marandi, B. Emrani, H. Zare, Synthesis of highly luminescent CdTe/CdS core-shell nanocrystals by optimization of the core and shell growth parameters, Opt. Mater. 69 (2017) 358–366, https://doi.org/10.1016/j.optmat.2017.04.058.
[70] E. Irani, E. Yazdani, A. Bayat, Enhancement and tuning of optical properties of CdTe/CdS core/shell quantum dots by tuning shell thickness, Optik. 249 (2022), https://doi.org/10.1016/j.ijleo.2021.168198.
[71] G. Yao, Z. Fu, X. Zhang, X. Zheng, X. Ji, Z. Cui, H. Zhang, Ultrafast carrier dynamics in CdSe/CdS/ZnS quantum dots, Chinese, J. Chem. Phys. 24 (2011) 640–646, https://doi.org/10.1088/1674-0068/24/06/640-646.
[72] R. Ghosh Chaudhuri, S. Paria, Core/shell nanoparticles: Classes, properties, synthesis mechanisms, characterization, and applications, Chem. Rev. 112 (2012) 2373–2433, https://doi.org/10.1021/cr100449n.
[73] C. Yan, F. Tang, L. Li, H. Li, X. Huang, D. Chen, X. Meng, J. Ren, Synthesis of aqueous CdTe/CdS/ZnS core/shell/shell quantum dots by a chemical aerosol flow method, Nanoscale Res. Lett. 5 (2010) 189, https://doi.org/10.1007/s11671-009-9464-x.
[74] R.K. Ratnesh, M.S. Mehata, Synthesis and optical properties of core-multi-shell CdSe/CdS/ZnS quantum dots: Surface modifications, Opt. Mater. 64 (2017) 250–256, https://doi.org/10.1016/j.optmat.2016.11.043.
[75] S. Parani, G. Bupesh, E. Manikandan, K. Pandian, O.S. Oluwafemi, Facile synthesis of mercaptosuccinic acid-capped CdTe/CdS/ZnS core/double shell quantum dots with improved cell viability on different cancer cells and normal cells, J. Nanopart. Res. 18 (2016) 347, https://doi.org/10.1007/s11051-016-3663-z.
[76] D.V. Talapin, I. Mekis, S. Götzinger, A. Kornowski, O. Benson, H. Weller, CdSe/CdS/ZnS and CdSe/ZnSe/ZnS core-shell-shell nanocrystals, J. Phys. Chem. B. 108 (2004) 18826–18831, https://doi.org/10.1021/jp046481g.
[77] S. Xu, H. Shen, C. Zhou, H. Yuan, C. Liu, H. Wang, L. Ma, L.S. Li, Effect of shell thickness on the optical properties in CdSe/CdS/$Zn_{0.5}$ $Cd_{0.5}$S/ZnS and CdSe/CdS/Zn_x Cd_{1-x} S/ZnS core/multishell nanocrystals, J. Phys. Chem. C. 115 (2011) 20876-20881. https://doi.org/10.1021/jp204831y.
[78] Y. Niu, C. Pu, R. Lai, R. Meng, W. Lin, H. Qin, X. Peng, One-pot/three-step synthesis of zinc-blende CdSe/CdS core/shell nanocrystals with thick shells, Nano Res. 10 (2017) 1149–1162, https://doi.org/10.1007/s12274-016-1287-3.
[79] Z. Fang, L. Liu, J. Wang, X. Zhong, Depositing a Zn_x Cd_{1-x} S shell around CdSe core nanocrystals via a noninjection approach in aqueous media, J. Phys. Chem. C. 113 (2009) 4301–4306, https://doi.org/10.1021/jp809653c.
[80] A. Mews, A.V. Kadavanich, U. Banin, A.P. Alivisatos, Structural and spectroscopic investigations of CdS/HgS/CdS quantum-dot quantum wells, Phys. Rev. B. 53 (1996) R13242–R13245, https://doi.org/10.1103/PhysRevB.53.R13242.
[81] H. Borchert, D. Dorfs, C. McGinley, S. Adam, T. Möller, H. Weller, A. Eychmüller, Photoemission study of onion like quantum dot quantum well and double quantum well nanocrystals of CdS and HgS, J. Phys. Chem. B. 107 (2003) 7486–7491, https://doi.org/10.1021/jp027485t.
[82] Y. Xie, J.-J. Xu, J.-S. Yu, H.-Y. Chen, Synthesis and characterization of water-soluble CdSe/ZnS core-shell nanoparticles, Chinese, J. Inorg. Chem. 20 (2004) 663–667.
[83] Y. Zhang, Y. Li, X.-P. Yan, Aqueous Layer-by-Layer Epitaxy of Type-II CdTe/CdSe Quantum Dots with Near-Infrared Fluorescence for Bioimaging Applications, Small. 5 (2008) 185–189, https://doi.org/10.1002/smll.200800473.
[84] S. Taniguchi, M. Green, S.B. Rizvi, A. Seifalian, The one-pot synthesis of core/shell/shell CdTe/CdSe/ZnSe quantum dots in aqueous media for in vivo deep tissue imaging, J. Mater. Chem. 21 (2011) 2877, https://doi.org/10.1039/c0jm03527k.
[85] B. Blackman, D. Battaglia, X. Peng, Bright and water-soluble near IR-emitting CdSe/CdTe/ZnSe type-II/type-I nanocrystals, tuning the efficiency and stability by growth, Chem. Mater. 20 (2008) 4847–4853, https://doi.org/10.1021/cm8000688.
[86] P. Yang, N. Murase, Synthesis of near-infrared-emitting CdTe/CdSe/ZnSe/ZnS heterostructure, J Nanosci. Nanotechnol. 14 (2014) 3147–3154, https://doi.org/10.1166/jnn.2014.8574.
[87] B.C. Fitzmorris, J.K. Cooper, J. Edberg, S. Gul, J. Guo, J.Z. Zhang, Synthesis and structural, optical, and dynamic properties of Core/Shell/Shell CdSe/ZnSe/ZnS quantum dots, J. Phys. Chem. C 116 (2012) 25065–25073, https://doi.org/10.1021/jp3092013.
[88] W. Zhang, G. Chen, J. Wang, B.-C. Ye, X. Zhong, Design and synthesis of highly luminescent near-infrared-emitting water-soluble CdTe/CdSe/ZnS core/shell/shell quantum dots, Inorg. Chem. 48 (2009) 9723–9731, https://doi.org/10.1021/ic9010949.
[89] H. Nishimura, K. Enomoto, Y.-J. Pu, D. Kim, Hydrothermal synthesis of water-soluble Mn- and Cu-doped CdSe quantum dots with multi-shell structures and their photoluminescence properties, RSC Adv. 12 (2022) 6255–6264, https://doi.org/10.1039/D1RA08491G.
[90] D. Deng, J. Xia, J. Cao, L. Qu, J. Tian, Z. Qian, Y. Gu, Z. Gu, Forming highly fluorescent near-infrared emitting PbS quantum dots in water using glutathione as surface-modifying molecule, J. Colloid Interface Sci. 367 (2012) 234–240, https://doi.org/10.1016/j.jcis.2011.09.043.
[91] J. Pichaandi, F.C.J.M. van Veggel, Near-infrared emitting quantum dots: Recent progress on their synthesis and characterization, Coord. Chem. Rev. 263–264 (2014) 138–150, https://doi.org/10.1016/j.ccr.2013.10.011.
[92] F. Yang, B. Zhou, X. Zhang, L. Wang, W. Jiang, Two-phase approach synthesis of high photoluminescence PbS quantum dots, Mater. Lett. 131 (2014) 35–37, https://doi.org/10.1016/j.matlet.2014.05.146.
[93] E.G. Durmusoglu, Y. Turker, H.Y. Acar, Green synthesis of strongly luminescent, ultrasmall PbS and PbSe quantum dots, J. Phys. Chem. C. 121 (2017) 12407–12415, https://doi.org/10.1021/acs.jpcc.7b01083.
[94] J.E. Murphy, M.C. Beard, A.G. Norman, S.P. Ahrenkiel, J.C. Johnson, P. Yu, O.I. Mićić, R.J. Ellingson, A.J. Nozik, PbTe colloidal nanocrystals: Synthesis, characterization, and multiple exciton generation, J. Am. Chem. Soc. 128 (2006) 3241–3247, https://doi.org/10.1021/ja0574973.
[95] A.A. Lipovskii, E.V. Kolobkova, A. Olkhovets, V.D. Petrikov, F. Wise, Synthesis of monodisperse PbS quantum dots in phosphate glass, Physica E Low Dimens. Syst. Nanostruct. 5 (1999) 157–160, https://doi.org/10.1016/S1386-9477(99)00037-5.
[96] C.B. Murray, S. Sun, W. Gaschler, H. Doyle, T.A. Betley, C.R. Kagan, Colloidal synthesis of nanocrystals and nanocrystal superlattices, IBM J. Res. Dev. 45 (2001) 47–56, https://doi.org/10.1147/rd.451.0047.
[97] W. Seo, J.-H. Yun, Y.C. Park, C.-S. Han, J. Lee, S. Jeong, Synthesis and characterization of lead selenide nanocrystal quantum dots and wires, J. Nanosci. Nanotech. 11 (2011) 4347–4350, https://doi.org/10.1166/jnn.2011.3681.
[98] J. Niu, H. Shen, X. Li, W. Xu, H. Wang, L.S. Li, Controlled synthesis of high quality PbSe and PbTe nanocrystals with one-pot method and their self-assemblies, Colloids Surf. A Physicochem. Eng. Asp. 406 (2012) 38, https://doi.org/10.1016/j.colsurfa.2012.04.046.
[99] A. Sashchiuk, L. Langof, R. Chaim, E. Lifshitz, Synthesis and characterization of PbSe and PbSe/PbS core-shell colloidal nanocrystals, J. Cryst. Growth 240 (2002) 431–438, https://doi.org/10.1016/S0022-0248(02)01156-9.
[100] T.M. Abeywickrama, A. Hassan, P.T. Snee, Colloidal synthesis of bulk-bandgap lead selenide nanocrystals, Front. Chem. 6 (2018) 562, https://doi.org/10.3389/fchem.2018.00562.
[101] M.A. Hines, G.D. Scholes, Colloidal PbS nanocrystals with size-tunable Near-infrared emission: Observation of post-synthesis self-narrowing of the particle size distribution, Adv. Mater. 15 (2003) 1844–1849, https://doi.org/10.1002/adma.200305395.
[102] C.M. Evans, L. Guo, J.J. Peterson, S. Maccagnano-Zacher, T.D. Krauss, Ultrabright PbSe magic-sized clusters, Nano Lett. 8 (2008) 2896–2899, https://doi.org/10.1021/nl801685a.
[103] Z. Lingley, S. Lu, A. Madhukar, A high quantum efficiency preserving approach to ligand exchange on lead sulfide quantum dots and interdot resonant energy transfer, Nano Lett. 11 (2011) 2887–2891, https://doi.org/10.1021/nl201351f.

[104] H.Y. Kim, D.-E. Yoon, J. Jang, D. Lee, G.-M. Choi, J.H. Chang, J.Y. Lee, D.C. Lee, B.-S. Bae, Quantum dot/siloxane composite film exceptionally stable against oxidation under heat and moisture, J. Am. Chem. Soc. 138 (2016) 16478–16485, https://doi.org/10.1021/jacs.6b10681.
[105] J. Aldana, Y.A. Wang, X. Peng, Photochemical instability of CdSe nanocrystals coated by hydrophilic thiols, J. Am. Chem. Soc. 123 (2001) 8844–8850, https://doi.org/10.1021/ja016424q.
[106] A. Shrestha, M. Batmunkh, A. Tricoli, S.Z. Qiao, S. Dai, Near-infrared active lead chalcogenide quantum dots: Preparation, post-synthesis ligand exchange, and applications in solar cells, Angew. Chem. Int. Ed. 58 (2019) 5202–5224, https://doi.org/10.1002/anie.201804053.
[107] D. Yanover, R.K. Čapek, A. Rubin-Brusilovski, R. Vaxenburg, N. Grumbach, G.I. Maikov, O. Solomeshch, A. Sashchiuk, E. Lifshitz, Small-sized PbSe/PbS core/shell colloidal quantum dots, Chem. Mater. 24 (2012) 4417–4423, https://doi.org/10.1021/cm302793k.
[108] B.-R. Hyun, M. Marus, H. Zhong, D. Li, H. Liu, Y. Xie, W. Koh, B. Xu, Y. Liu, X.W. Sun, Infrared light-emitting diodes based on colloidal PbSe/PbS core/shell nanocrystals, Chinese Phys. B. 29 (2020), https://doi.org/10.1088/1674-1056/ab5fb7.
[109] G. Zaiats, D. Yanover, R. Vaxenburg, J. Tilchin, A. Sashchiuk, E. Lifshitz, PbSe-based colloidal core/shell heterostructures for optoelectronic applications, Materials 7 (2014) 7243–7275, https://doi.org/10.3390/ma7117243.
[110] A. Kigel, M. Brumer, A. Sashchiuk, L. Amirav, E. Lifshitz, PbSe/PbSexS$_{1-x}$ core-alloyed shell nanocrystals, Mater. Sci. Eng. C. 25 (2005) 604–608, https://doi.org/10.1016/j.msec.2005.06.010.
[111] M. Brumer, A. Kigel, L. Amirav, A. Sashchiuk, O. Solomesch, N. Tessler, E. Lifshitz, PbSe/PbS and PbSe/PbSexS$_{1-x}$ Core/shell nanocrystals, Adv. Funct. Mater. 15 (2005) 1111–1116, https://doi.org/10.1002/adfm.200400620.
[112] Y. Zhang, Q. Dai, X. Li, Q. Cui, Z. Gu, B. Zou, Y. Wang, W.W. Yu, Formation of PbSe/CdSe core/shell nanocrystals for stable near-infrared high photoluminescence emission, Nanoscale Res. Lett. 5 (2010) 1279–1283, https://doi.org/10.1007/s11671-010-9637-7.
[113] Y. Du, B. Xu, T. Fu, M. Cai, F. Li, Y. Zhang, Q. Wang, Near-infrared photoluminescent Ag_2S quantum dots from a single source precursor, J. Am. Chem. Soc. 132 (2010) 1470–1471, https://doi.org/10.1021/ja909490r.
[114] P. Jiang, Z.-Q. Tian, C.-N. Zhu, Z.-L. Zhang, D.-W. Pang, Emission-tunable near-infrared Ag_2S quantum dots, Chem. Mater. 24 (2012) 3–5, https://doi.org/10.1021/cm202543m.
[115] P. Jiang, C.-N. Zhu, Z.-L. Zhang, Z.-Q. Tian, D.-W. Pang, Water-soluble Ag_2S quantum dots for near-infrared fluorescence imaging in vivo, Biomaterials 33 (2012) 5130–5135, https://doi.org/10.1016/j.biomaterials.2012.03.059.
[116] Y. Wang, X.-P. Yan, Fabrication of vascular endothelial growth factor antibody bioconjugated ultrasmall near-infrared fluorescent Ag_2S quantum dots for targeted cancer imaging in vivo, Chem. Commun. 49 (2013) 3324, https://doi.org/10.1039/c3cc41141a.
[117] N.J. Hunt, G.P. Lockwood, F.H. Le Couteur, P.A.G. McCourt, N. Singla, S.W.S. Kang, A. Burgess, Z. Kuncic, D.G. Le Couteur, V.C. Cogger, Rapid intestinal uptake and targeted delivery to the liver endothelium using orally administered silver sulfide quantum dots, ACS Nano 14 (2020) 1492–1507, https://doi.org/10.1021/acsnano.9b06071.
[118] C. Wang, Y. Wang, L. Xu, D. Zhang, M. Liu, X. Li, H. Sun, Q. Lin, B. Yang, Facile aqueous-phase synthesis of biocompatible and fluorescent Ag_2S nanoclusters for bioimaging: Tunable photoluminescence from red to near infrared, Small 8 (2012) 3137–3142, https://doi.org/10.1002/smll.201200376.
[119] H.-Y. Yang, Y.-W. Zhao, Z.-Y. Zhang, H.-M. Xiong, S.-N. Yu, One-pot synthesis of water-dispersible Ag_2S quantum dots with bright fluorescent emission in the second near-infrared window, Nanotechnol. 24 (2013), https://doi.org/10.1088/0957-4484/24/5/055706.
[120] J. Gao, C. Wu, D. Deng, P. Wu, C. Cai, Direct synthesis of water-soluble aptamer-Ag_2S Quantum dots at ambient temperature for specific imaging and photothermal therapy of cancer, Adv. Healthc. Mater. 5 (2016) 2437–2449, https://doi.org/10.1002/adhm.201600545.
[121] C.-N. Zhu, P. Jiang, Z.-L. Zhang, D.-L. Zhu, Z.-Q. Tian, D.-W. Pang, Ag_2Se quantum dots with tunable emission in the second near-infrared window, ACS Appl. Mater. Interfaces. 5 (2013) 1186–1189, https://doi.org/10.1021/am303110x.
[122] A. Sahu, A. Khare, D.D. Deng, D.J. Norris, Quantum confinement in silver selenide semiconductor nanocrystals, Chem. Commun. 48 (2012) 5458, https://doi.org/10.1039/c2cc30539a.
[123] C. Chen, X. He, L. Gao, N. Ma, Cation exchange-based facile aqueous synthesis of small, stable, and nontoxic near-infrared Ag_2Te/ZnS core/shell quantum dots emitting in the second biological window, ACS Appl. Mater. Interfaces. 5 (2013) 1149–1155, https://doi.org/10.1021/am302933x.
[124] S. Gholamrezaei, M. Salavati-Niasari, D. Ghanbari, S. Bagheri, Hydrothermal preparation of silver telluride nanostructures and photo-catalytic investigation in degradation of toxic dyes, Sci. Rep. 6 (2016) 20060, https://doi.org/10.1038/srep20060.
[125] M. Yang, R. Gui, H. Jin, Z. Wang, F. Zhang, J. Xia, S. Bi, Y. Xia, Ag_2Te quantum dots with compact surface coatings of multivalent polymers: Ambient one-pot aqueous synthesis and the second near-infrared bioimaging, Colloids Surf. B: Biointerfaces. 126 (2015) 115–120, https://doi.org/10.1016/j.colsurfb.2014.11.030.
[126] H. Doh, S. Hwang, S. Kim, Size-tunable synthesis of nearly monodisperse Ag_2S nanoparticles and size-dependent fate of the crystal structures upon cation exchange to $AgInS_2$ nanoparticles, Chem. Mater. 28 (2016) 8123–8127, https://doi.org/10.1021/acs.chemmater.6b04011.
[127] J. Hu, Q. Lu, K. Tang, Y. Qian, J. Hu, Q. Lu, K. Tang, Y. Qian, G. Zhou, X. Liu, Solvothermal reaction route to nanocrystalline semiconductors $AgMS_2$ (M=Ga, In), Chem. Commun. (1999) 1093–1094, https://doi.org/10.1039/a902218j.
[128] X. Tang, K. Yu, Q. Xu, E.S.G. Choo, G.K.L. Goh, J. Xue, Synthesis and characterization of $AgInS_2$-ZnS heterodimers with tunable photoluminescence, J. Mater. Chem. 21 (2011) 11239, https://doi.org/10.1039/c1jm11346a.
[129] M. Mousavi-Kamazani, M. Salavati-Niasari, A simple microwave approach for synthesis and characterization of Ag_2S-$AgInS_2$ nanocomposites, Compos.B. Eng. 56 (2014) 490–496, https://doi.org/10.1016/j.compositesb.2013.08.066.
[130] W. Zhang, D. Li, Z. Chen, M. Sun, W. Li, Q. Lin, X. Fu, Microwave hydrothermal synthesis of $AgInS_2$ with visible light photocatalytic activity, Mater. Res. Bull. 46 (2011) 975–982, https://doi.org/10.1016/j.materresbull.2011.03.026.
[131] H. Shi, L. Jia, C. Wang, E. Liu, Z. Ji, J. Fan, A high sensitive and selective fluorescent probe for dopamine detection based on water soluble $AgInS_2$ quantum dots, Opt. Mat. 99 (2020), https://doi.org/10.1016/j.optmat.2019.109549.
[132] B. Yuan, X. Cai, X. Fang, D. Wang, S. Cao, R. Zhu, J. Liu, Synthesis of water-soluble quantum dots from Ag_2S and $AgInS_2$ QDs, Cryst. Growth Des. 20 (2020) 4204–4211, https://doi.org/10.1021/acs.cgd.0c00108.
[133] M.T. Ng, C.B. Boothroyd, J.J. Vittal, One-pot synthesis of new-phase $AgInSe_2$ nanorods, J. Am. Chem. Soc. 128 (2006) 7118–7119, https://doi.org/10.1021/ja060543u.
[134] O. Raievska, O. Stroyuk, V. Dzhagan, D. Solonenko, D.R.T. Zahn, Ultra-small aqueous glutathione-capped Ag-In-Se quantum dots: Luminescence and vibrational properties, RSC Adv. 10 (2020) 42178–42193, https://doi.org/10.1039/D0RA07706B.
[135] M.-A. Langevin, T. Pons, A. M. Ritcey, C. Nì. Allen, Near-infrared emitting $AgInTe_2$ and Zn-Ag-In-Te colloidal nanocrystals, Nanoscale Res. Lett. 10 (2015) 255. https://doi.org/10.1186/s11671-015-0951-y. Z. P. Aguilar, H. Xu, A. Wang, Blocking nonspecific uptake of engineered nanomaterials, ECS Meet. Abstr. MA2009-02 (2009) 3134–3134. https://doi.org/10.1149/ma2009-02/42/3134
[136] Z.P. Aguilar, H. Xu, A. Wang, Blocking nonspecific uptake of engineered nanomaterials, ECS, Meet. Abstr. MA2009-02 (2009) 3134, https://doi.org/10.1149/ma2009-02/42/3134.
[137] M. Borovaya, A. Naumenko, I. Horiunova, S. Plokhovska, Y. Blume, A. Yemets, "Green" synthesis of Ag_2S nanoparticles, study of their properties and bioimaging applications, Appl. Nanosci. 10 (2020) 4931–4940, https://doi.org/10.1007/s13204-020-01365-3.
[138] T.S. Alomar, N. AlMasoud, M.A. Awad, M.F. El-Tohamy, D.A. Soliman, An eco-friendly plant-mediated synthesis of silver nanoparticles: Characterization, pharmaceutical and biomedical applications, Mater. Chem. Phys. 249 (2020), https://doi.org/10.1016/j.matchemphys.2020.123007.
[139] V. G. Debabov, T. A. Voeikova, A. S. Shebanova, K. V. Shaitan, L. K. Emel'yanova, L. M. Novikova, M. P. Kirpichnikov, Bacterial synthesis of silver sulfide nanoparticles, Nanotechnol Russ. 8 (2013) 269-276. https://doi.org/10.1134/S1995078013020043
[140] I. L. Plastun, A. A. Zakharov, A. A. Naumov, Features of silver sulfide nanoparticles bacterial synthesis: Molecular modeling, in: 2020 International Conference on Actual Problems of Electron Devices Engineering (APEDE), IEEE, Saratov, Russia, 2020. 318-322. https://doi.org/10.1109/APEDE48864.2020.9255570
[141] D. Ayodhya, G. Veerabhadram, Green synthesis, characterization, photocatalytic, fluorescence and antimicrobial activities of Cochlospermum gossypium capped Ag_2S nanoparticles, J. Photochem. Photobiol. B: Biol. 157 (2016) 57–69, https://doi.org/10.1016/j.jphotobiol.2016.02.002.
[142] M. Zahedifar, M. Shirani, A. Akbari, N. Seyedi, Green synthesis of Ag_2S nanoparticles on cellulose/Fe_3O_4 nanocomposite template for catalytic degradation of organic dyes, Cellulose 26 (2019) 6797–6812, https://doi.org/10.1007/s10570-019-02550-6.
[143] J. Liu, D. Zheng, L. Zhong, A. Gong, S. Wu, Z. Xie, Biosynthesis of biocompatibility Ag_2Se quantum dots in Saccharomyces cerevisiae and its application, Biochem. Biophys. Res. Commun. 544 (2021) 60–64, https://doi.org/10.1016/j.bbrc.2021.01.071.
[144] Y. Delgado-Beleño, C.E. Martinez-Nuñez, M. Cortez-Valadez, N.S. Flores-López, M. Flores-Acosta, Optical properties of silver, silver sulfide and silver selenide nanoparticles and antibacterial applications, Mater. Res. Bull. 99 (2018) 385–392, https://doi.org/10.1016/j.materresbull.2017.11.015.
[145] F. Erogbogbo, K.-T. Yong, I. Roy, R. Hu, W.-C. Law, W. Zhao, H. Ding, F. Wu, R. Kumar, M.T. Swihart, P.N. Prasad, In vivo targeted cancer imaging, sentinel lymph node mapping and multi-channel imaging with biocompatible silicon nanocrystals, ACS Nano 5 (2011) 413–423, https://doi.org/10.1021/nn1018945.
[146] P. Shen, S. Ohta, S. Inasawa, Y. Yamaguchi, Selective labeling of the endoplasmic reticulum in live cells with silicon quantum dots, Chem. Commun. 47 (2011) 8409, https://doi.org/10.1039/c1cc12713f.
[147] A. Shiohara, S. Prabakar, A. Faramus, C.-Y. Hsu, P.-S. Lai, P.T. Northcote, R.D. Tilley, Sized controlled synthesis, purification, and cell studies with silicon quantum dots, Nanoscale 3 (2011) 3364, https://doi.org/10.1039/c1nr10458f.
[148] X. Bai, F. Purcell-Milton, Y. Gun'ko, Optical properties, synthesis, and potential applications of Cu-based ternary or quaternary anisotropic quantum dots, polytypic nanocrystals, and core/shell heterostructures, Nanomaterials 9 (2019) 85, https://doi.org/10.3390/nano9010085.

[149] C. Coughlan, M. Ibáñez, O. Dobrozhan, A. Singh, A. Cabot, K.M. Ryan, Compound copper chalcogenide nanocrystals, Chem. Rev. 117 (2017) 5865–6109, https://doi.org/10.1021/acs.chemrev.6b00376.
[150] O. Yarema, M. Yarema, V. Wood, Tuning the composition of multicomponent semiconductor nanocrystals: The case of I-III-VI materials, Chem. Mater. 16 (2018), https://doi.org/10.1021/acs.chemmater.7b04710.
[151] S.L. Castro, S.G. Bailey, R.P. Raffaelle, K.K. Banger, A.F. Hepp, Synthesis and characterization of colloidal $CuInS_2$ nanoparticles from a molecular single-source precursor, J. Phys. Chem. B. 108 (2004) 12429–12435, https://doi.org/10.1021/jp049107p.
[152] R. Xie, M. Rutherford, X. Peng, Formation of high-quality I-III-VI semiconductor nanocrystals by tuning relative reactivity of cationic precursors, J. Am. Chem. Soc. 131 (2009) 5691–5697, https://doi.org/10.1021/ja9005767.
[153] R.C. Fitzmorris, R.P. Oleksak, Z. Zhou, B.D. Mangum, J.N. Kurtin, G.S. Herman, Structural and optical characterization of $CuInS_2$ quantum dots synthesized by microwave-assisted continuous flow methods, J Nanopart. Res. 17 (2015) 319, https://doi.org/10.1007/s11051-015-3123-1.
[154] A. Arshad, H. Chen, X. Bai, S. Xu, L. Wang, One-pot aqueous synthesis of highly biocompatible near infrared $CuInS_2$ quantum dots for target cell imaging, Chin. J. Chem. 34 (2016) 576–582, https://doi.org/10.1002/cjoc.201500777.
[155] C. Xia, W. Wu, T. Yu, X. Xie, C. van Oversteeg, H.C. Gerritsen, C. de Mello Donega, Size-dependent band-gap and molar absorption coefficients of colloidal $CuInS_2$ quantum dots, ACS Nano 12 (2018) 8350–8361, https://doi.org/10.1021/acsnano.8b03641.
[156] R. Marin, A. Vivian, A. Skripka, A. Migliori, V. Morandi, F. Enrichi, F. Vetrone, P. Ceroni, C. Aprile, P. Canton, Mercaptosilane-passivated $CuInS_2$ quantum dots for luminescence thermometry and luminescent labels, ACS Appl. Nano Mater. 2 (2019) 2426–2436, https://doi.org/10.1021/acsanm.9b00317.
[157] E. Witt, J. Kolny-Olesiak, Recent developments in colloidal synthesis of $CuInSe_2$ nanoparticles, Chem. Eur. J. 19 (2013) 9746–9753, https://doi.org/10.1002/chem.201301076.
[158] E. Cassette, T. Pons, C. Bouet, M. Helle, L. Bezdetnaya, F. Marchal, B. Dubertret, Synthesis and characterization of near-infrared Cu-In-Se/ZnS core/shell quantum dots for in vivo imaging, Chem. Mater. 22 (2010) 6117–6124, https://doi.org/10.1021/cm101881b.
[159] S.L. Castro, S.G. Bailey, R.P. Raffaelle, K.K. Banger, A.F. Hepp, Nanocrystalline chalcopyrite materials ($CuInS_2$ and $CuInSe_2$) via low-temperature pyrolysis of molecular single-source precursors, Chem. Mater. 15 (2003) 3142–3147, https://doi.org/10.1021/cm034161o.
[160] Q. Guo, S.J. Kim, M. Kar, W.N. Shafarman, R.W. Birkmire, E.A. Stach, R. Agrawal, H.W. Hillhouse, Development of $CuInSe_2$ nanocrystal and nanoring Inks for low-cost solar cells, Nano Lett. 8 (2008) 2982–2987, https://doi.org/10.1021/nl802042g.
[161] M.G. Panthani, V. Akhavan, B. Goodfellow, J.P. Schmidtke, L. Dunn, A. Dodabalapur, P.F. Barbara, B.A. Korgel, Synthesis of CuInS2, CuInSe2, and Cu (In x Ga1- x)Se2 (CIGS) nanocrystal "inks" for printable photovoltaics, J. Am. Chem. Soc. 130 (2008) 16770–16777, https://doi.org/10.1021/ja805845q.
[162] J. Tang, S. Hinds, S.O. Kelley, E.H. Sargent, Synthesis of colloidal CuGaSe2, CuInSe2, and Cu(InGa)Se2 nanoparticles, Chem. Mater. 20 (2008) 6906–6910, https://doi.org/10.1021/cm801655w.
[163] M.G. Panthani, C.J. Stolle, D.K. Reid, D.J. Rhee, T.B. Harvey, V.A. Akhavan, Y. Yu, B.A. Korgel, $CuInSe_2$ Quantum dot solar cells with high open-circuit voltage, J. Phys. Chem. Lett. 4 (2013) 2030–2034, https://doi.org/10.1021/jz4010015.
[164] O. Yarema, D. Bozyigit, I. Rousseau, L. Nowack, M. Yarema, W. Heiss, V. Wood, Highly luminescent, size- and shape-tunable copper indium selenide-based colloidal nanocrystals, Chem. Mater. 25 (2013) 3753–3757, https://doi.org/10.1021/cm402306q.
[165] P.M. Allen, M.G. Bawendi, Ternary I-III-VI quantum dots luminescent in the red to near-infrared, J. Am. Chem. Soc. 130 (2008) 9240–9241, https://doi.org/10.1021/ja8036349.
[166] J. Park, C. Dvoracek, K.H. Lee, J.F. Galloway, H.C. Bhang, M.G. Pomper, P.C. Searson, CuInSe/ZnS core/shell NIR quantum dots for biomedical imaging, Small 7 (2011) 3148–3152, https://doi.org/10.1002/smll.201101558.
[167] H. Shen, X.-D. Jiang, S. Wang, Y. Fu, C. Zhou, L.S. Li, Facile preparation of metal telluride nanocrystals using di-n-octylphosphine oxide (DOPO) as an air-stable and less toxic alternative to the common tri-alkylphosphines, J. Mater. Chem. 22 (2012) 25050, https://doi.org/10.1039/c2jm35598a.
[168] O. Yarema, M. Yarema, W.M.M. Lin, V. Wood, Cu-In-Te and Ag-In-Te colloidal nanocrystals with tunable composition and size, Chem. Commun. 52 (2016) 10878–10881, https://doi.org/10.1039/C6CC05571K.
[169] W. van der Stam, E. Bladt, F.T. Rabouw, S. Bals, C. de Mello Donega, Near-infrared emitting $CuInSe_2/CuInS_2$ dot core/rod shell heteronanorods by sequential cation exchange, ACS Nano 9 (2015) 11430–11438, https://doi.org/10.1021/acsnano.5b05496.
[170] L. Li, A. Pandey, D.J. Werder, B.P. Khanal, J.M. Pietryga, V.I. Klimov, Efficient synthesis of highly luminescent copper indium sulfide-based core/shell nanocrystals with surprisingly long-lived emission, J. Am. Chem. Soc. 133 (2011) 1176–1179, https://doi.org/10.1021/ja108261h.
[171] K.J. McHugh, L. Jing, S.Y. Severt, M. Cruz, M. Sarmadi, H.S.N. Jayawardena, C.F. Perkinson, F. Larusson, S. Rose, S. Tomasic, T. Graf, S.Y. Tzeng, J.L. Sugarman, D. Vlasic, M. Peters, N. Peterson, L. Wood, W. Tang, J. Yeom, J. Collins, P.A. Welkhoff, A. Karchin, M. Tse, M. Gao, M.G. Bawendi, R. Langer, A. Jaklenec, Biocompatible near-infrared quantum dots delivered to the skin by microneedle patches record vaccination, Sci. Transl. Med. 11 (2019) 7162, https://doi.org/10.1126/scitranslmed.aay7162.
[172] R.L. Wells, S.R. Aubuchon, S.S. Kher, M.S. Lube, P.S. White, Synthesis of nanocrystalline indium arsenide and indium phosphide from indium(III) halides and tris(trimethylsilyl)pnicogens. Synthesis, characterization, and decomposition behavior of I3In.cntdot.P($SiMe_3$)3, Chem. Mater. 7 (1995) 793–800, https://doi.org/10.1021/cm00052a027.
[173] A.A. Guzelian, U. Banin, A.V. Kadavanich, X. Peng, A.P. Alivisatos, Colloidal chemical synthesis and characterization of InAs nanocrystal quantum dots, Appl. Phys. Lett. 69 (1996) 1432–1434, https://doi.org/10.1063/1.117605.
[174] D. Battaglia, X. Peng, Formation of high quality InP and InAs nanocrystals in a noncoordinating solvent, Nano Lett. 2 (2002) 1027–1030, https://doi.org/10.1021/nl025687v.
[175] R. Xie, X. Peng, Synthetic scheme for high-quality InAs nanocrystals based on self-focusing and one-pot synthesis of InAs-based core-shell nanocrystals, Angew. Chem. Int. Ed. 47 (2008) 7677–7680, https://doi.org/10.1002/anie.200802867.
[176] M. D. Healy, P. E. Laibinis, P. D. Stupik, A. R. Barron, The reaction of indium(iii) chloride with tris(trimethylsily1)phosphine: A novel route to indium phosphide, J. Chem. Soc., Chem. Commun. 6(1989) 359-360 https://doi.org/10.1039/C39890000359.
[177] O.I. Micic, C.J. Curtis, K.M. Jones, J.R. Sprague, A.J. Nozik, Synthesis and characterization of InP quantum dots, J. Phys. Chem. 98 (1994) 4966–4969, https://doi.org/10.1021/j100070a004.
[178] A.A. Guzelian, J.E.B. Katari, A.V. Kadavanich, U. Banin, K. Hamad, E. Juban, A.P. Alivisatos, R.H. Wolters, C.C. Arnold, J.R. Heath, Synthesis of size-selected, surface-passivated InP nanocrystals, J. Phys. Chem. 100 (1996) 7212–7219, https://doi.org/10.1021/jp953719f.
[179] M.D. Tessier, K. De Nolf, D. Dupont, D. Sinnaeve, J. De Roo, Z. Hens, Aminophosphines: A double role in the synthesis of colloidal indium phosphide quantum dots, J. Am. Chem. Soc. 138 (2016) 5923–5929, https://doi.org/10.1021/jacs.6b01254.
[180] J. van Embden, A.S.R. Chesman, J.J. Jasieniak, The heat-up synthesis of colloidal nanocrystals, Chem. Mater. 27 (2015) 2246–2285, https://doi.org/10.1021/cm5028964.
[181] M. Green, P. O'Brien, The synthesis of III-V semiconductor nanoparticles using indium and gallium diorganophosphides as single-molecular precursors, J. Mater. Chem. 14 (2004) 629–636, https://doi.org/10.1039/B304000N.
[182] C. Li, M. Ando, H. Enomoto, N. Murase, Highly luminescent water-soluble InP/ZnS nanocrystals prepared via reactive phase transfer and photochemical processing, J. Phys. Chem. C. 112 (2008) 20190–20199, https://doi.org/10.1021/jp805491b.
[183] H.-J. Byun, J.C. Lee, H. Yang, Solvothermal synthesis of InP quantum dots and their enhanced luminescent efficiency by post-synthetic treatments, J Colloid Interface Sci. 355 (2011) 35–41, https://doi.org/10.1016/j.jcis.2010.12.013.
[184] P. Ramasamy, K.-J. Ko, J.-W. Kang, J.-S. Lee, Two-step "seed-mediated" synthetic approach to colloidal indium phosphide quantum dots with high-purity photo- and electroluminescence, Chem. Mater. 30 (2018) 3643–3647, https://doi.org/10.1021/acs.chemmater.8b02049.
[185] U. Cao, Banin, Growth and properties of semiconductor core/shell nanocrystals with InAs cores, J. Am. Chem. Soc. 122 (2000) 9692–9702, https://doi.org/10.1021/ja001386g.
[186] D. Franke, D.K. Harris, O. Chen, O.T. Bruns, J.A. Carr, M.W.B. Wilson, M.G. Bawendi, Continuous injection synthesis of indium arsenide quantum dots emissive in the short-wavelength infrared, Nat. Commun. 7 (2016) 12749, https://doi.org/10.1038/ncomms12749.
[187] S. Haubold, M. Haase, A. Kornowski, H. Weller, Strongly luminescent InP/ZnS core-shell nanoparticles, ChemPhysChem 2 (2001) 331–334, https://doi.org/10.1002/1439-7641(20010518)2:5<331::AID-CPHC331>3.0.CO;2-0.
[188] R. Xie, D. Battaglia, X. Peng, Colloidal InP nanocrystals as efficient emitters covering blue to near-infrared, J. Am. Chem. Soc. 129 (2007) 15432–15433, https://doi.org/10.1021/ja076363h.
[189] L. Li, M. Protière, P. Reiss, Economic synthesis of high quality InP nanocrystals using calcium phosphide as the phosphorus precursor, Chem. Mater. 20 (2008) 2621–2623, https://doi.org/10.1021/cm7035579.
[190] S. Xu, J. Ziegler, T. Nann, Rapid synthesis of highly luminescent InP and InP/ZnS nanocrystals, J. Mater. Chem. 18 (2008) 2653, https://doi.org/10.1039/b803263g.
[191] Y.-H. Won, O. Cho, T. Kim, D.-Y. Chung, T. Kim, H. Chung, H. Jang, J. Lee, D. Kim, E. Jang, Highly efficient and stable InP/ZnSe/ZnS quantum dot light-emitting diodes, Nature 575 (2019) 634–638, https://doi.org/10.1038/s41586-019-1771-5.
[192] V. Biju, T. Itoh, M. Ishikawa, Delivering quantum dots to cells: bioconjugated quantum dots for targeted and nonspecific extracellular and intracellular imaging, Chem. Soc. Rev. 39 (2010) 3031, https://doi.org/10.1039/b926512k.
[193] Y.Z. Hu, S.W. Koch, N. Peyghambarian, Strongly confined semiconductor quantum dots: Pair excitations and optical properties, J. Lumin. 70 (1996) 185–202, https://doi.org/10.1016/0022-2313(96)00054-3.
[194] D.W. Ayele, W.-N. Su, H.-L. Chou, C.-J. Pan, B.-J. Hwang, Composition-controlled optical properties of colloidal CdSe quantum dots, Appl. Surf. Sci. 322 (2014) 177–184, https://doi.org/10.1016/j.apsusc.2014.10.079.
[195] M.G. Bawendi, M.L. Steigerwald, L.E. Brus, The quantum mechanics of larger semiconductor clusters ("quantum dots"), Annu. Rev. Phys. Chem. 41 (1990) 477–496, https://doi.org/10.1146/annurev.pc.41.100190.002401.
[196] B. Bajorowicz, M.P. Kobylański, A. Gołąbiewska, J. Nadolna, A. Zaleska-Medynska, A. Malankowska, Quantum dot-decorated semiconductor micro- and nanoparticles: A review of their synthesis, characterization and

application in photocatalysis, Adv. Colloid Interface Sci. 256 (2018) 352–372, https://doi.org/10.1016/j.cis.2018.02.003.
[197] Y. Ma, Y. Zhang, W.W. Yu, Near infrared emitting quantum dots: synthesis, luminescence properties and applications, J. Mater. Chem. C. 7 (2019) 13662–13679, https://doi.org/10.1039/C9TC04065J.
[198] W.R. Algar, M. Massey, K. Rees, R. Higgins, K.D. Krause, G.H. Darwish, W.J. Peveler, Z. Xiao, H.-Y. Tsai, R. Gupta, K. Lix, M.V. Tran, H. Kim, Photoluminescent nanoparticles for chemical and biological analysis and imaging, Chem. Rev. 121 (2021) 9243–9358, https://doi.org/10.1021/acs.chemrev.0c01176.
[199] A.B. Greytak, P.M. Allen, W. Liu, J. Zhao, E.R. Young, Z. Popović, B.J. Walker, D. G. Nocera, M.G. Bawendi, Alternating layer addition approach to CdSe/CdS core/shell quantum dots with near-unity quantum yield and high on-time fractions, Chem. Sci. 3 (2012) 2028, https://doi.org/10.1039/c2sc00561a.
[200] J. McBride, J. Treadway, L.C. Feldman, S.J. Pennycook, S.J. Rosenthal, Structural basis for near unity quantum yield core/shell nanostructures, Nano Lett. 6 (2006) 1496–1501, https://doi.org/10.1021/nl060993k.
[201] W.W. Yu, L. Qu, W. Guo, X. Peng, Experimental determination of the extinction coefficient of CdTe, CdSe, and CdS nanocrystals, Chem. Mater. 15 (2003) 2854–2860, https://doi.org/10.1021/cm034081k.
[202] S.J. Rosenthal, J.C. Chang, O. Kovtun, J.R. McBride, I.D. Tomlinson, Biocompatible quantum dots for biological applications, Chem. Biol. 18 (2011) 10–24, https://doi.org/10.1016/j.chembiol.2010.11.013.
[203] S. Maćkowski, G. Karczewski, J. Kossut, G. Sęk, J. Misiewicz, G. Prechtl, W. Heiss, Optical properties of CdTe/ZnTe quantum dot superlattices, Physica E Low Dimens. Syst. Nanostruct. 12 (2002) 503–506, https://doi.org/10.1016/S1386-9477(01)00343-5.
[204] S. Aryal, R. Pati, PbTe(core)/PbS(shell) nanowire: Electronic structure, thermodynamic stability, and mechanical and optical properties, J. Phys. Chem. C. 125 (2021) 22660–22667, https://doi.org/10.1021/acs.jpcc.1c06577.
[205] Y. Zhang, Y. Liu, C. Li, X. Chen, Q. Wang, Controlled synthesis of Ag_2S quantum dots and experimental determination of the exciton Bohr radius, J. Phys. Chem. C. 118 (2014) 4918–4923, https://doi.org/10.1021/jp501266d.
[206] J. Zhang, J. Gao, E.M. Miller, J.M. Luther, M.C. Beard, Diffusion-controlled synthesis of PbS and PbSe quantum dots with *in situ* halide passivation for quantum dot solar cells, ACS Nano 8 (2014) 614–622, https://doi.org/10.1021/nn405236k.
[207] B.L. Wehrenberg, C. Wang, P. Guyot-Sionnest, Interband and intraband optical studies of PbSe colloidal quantum dots, J. Phys. Chem. B. 106 (2002) 10634–10640, https://doi.org/10.1021/jp021187e.
[208] S. Hinds, S. Myrskog, L. Levina, G. Koleilat, J. Yang, S.O. Kelley, E.H. Sargent, NIR-emitting colloidal quantum dots having 26 % luminescence quantum yield in buffer solution, J. Am. Chem. Soc. 129 (2007) 7218–7219, https://doi.org/10.1021/ja070525s.
[209] D. Deng, W. Zhang, X. Chen, F. Liu, J. Zhang, Y. Gu, J. Hong, Facile synthesis of high-quality, water-soluble, near-infrared-emitting PbS quantum dots, Eur. J. Inorg. Chem. 2009 (2009) 3440–3446, https://doi.org/10.1002/ejic.200900227.
[210] I. Moreels, K. Lambert, D. Smeets, D. De Muynck, T. Nollet, J.C. Martins, F. Vanhaecke, A. Vantomme, C. Delerue, G. Allan, Z. Hens, Size-dependent optical properties of colloidal PbS quantum dots, ACS Nano 3 (2009) 3023–3030, https://doi.org/10.1021/nn900863a.
[211] K. Bian, B.T. Richards, H. Yang, W. Bassett, F.W. Wise, Z. Wang, T. Hanrath, Optical properties of PbS nanocrystal quantum dots at ambient and elevated pressure, Phys. Chem. Chem. Phys. 16 (2014) 8515–8520, https://doi.org/10.1039/C4CP00395K.
[212] C. Cheng, J. Li, X. Cheng, Photoluminescence lifetime and absorption spectrum of PbS nanocrystal quantum dots, J. Lumin. 188 (2017) 252–257, https://doi.org/10.1016/j.jlumin.2017.04.037.
[213] H. Liu, P. Guyot-Sionnest, Photoluminescence lifetime of lead selenide colloidal quantum dots, J. Phys. Chem. C. 114 (2010) 14860–14863, https://doi.org/10.1021/jp105818e.
[214] B. Bai, M. Xu, N. Li, W. Chen, J. Liu, J. Liu, H. Rong, D. Fenske, J. Zhang, Semiconductor nanocrystal engineering by applying thiol- and solvent-coordinated cation exchange kinetics, Angew. Chem. Int. Ed. 58 (2019) 4852–4857, https://doi.org/10.1002/anie.201807695.
[215] G. Xu, S. Zeng, B. Zhang, M.T. Swihart, K.-T. Yong, P.N. Prasad, New generation cadmium-free quantum dots for biophotonics and nanomedicine, Chem. Rev. 116 (2016) 12234–12327, https://doi.org/10.1021/acs.chemrev.6b00290.
[216] Y. Kayanuma, Quantum-size effects of interacting electrons and holes in semiconductor microcrystals with spherical shape, Phys. Rev. B. 38 (1988) 9797–9805, https://doi.org/10.1103/PhysRevB.38.9797.
[217] J. Mirzaei, M. Reznikov, T. Hegmann, Quantum dots as liquid crystal dopants, J. Mater. Chem. 22 (2012) 22350, https://doi.org/10.1039/c2jm33274d.
[218] Z.-Y. Liu, A.-A. Liu, H. Fu, Q.-Y. Cheng, M.-Y. Zhang, M.-M. Pan, L.-P. Liu, M.-Y. Luo, B. Tang, W. Zhao, J. Kong, X. Shao, D.-W. Pang, Breaking through the Size control dilemma of silver chalcogenide quantum dots via trialkylphosphine-induced ripening: Leading to Ag_2Te emitting from 950 to 2100 nm, J. Am. Chem. Soc. 143 (2021) 12867–12877, https://doi.org/10.1021/jacs.1c06661.
[219] I. Hocaoglu, M.N. Çizmeciyan, R. Erdem, C. Ozen, A. Kurt, A. Sennaroglu, H.Y. Acar, Development of highly luminescent and cytocompatible near-IR-emitting aqueous Ag_2S quantum dots, J. Mater. Chem. 22 (2012) 14674, https://doi.org/10.1039/c2jm31959d.
[220] Y. Zhang, G. Hong, Y. Zhang, G. Chen, F. Li, H. Dai, Q. Wang, Ag_2S Quantum dot: A bright and biocompatible fluorescent nanoprobe in the second near-infrared window, ACS Nano 6 (2012) 3695–3702, https://doi.org/10.1021/nn301218z.
[221] J.-Z. Zhang, H. Tang, X.-Z. Chen, Q. Su, W.-S. Xi, Y.-Y. Liu, Y. Liu, A. Cao, H. Wang, In vivo fate of Ag_2Te quantum dot and comparison with other NIR-II silver chalcogenide quantum dots, J Nanopart. Res. 22 (2020) 287, https://doi.org/10.1007/s11051-020-04992-7.
[222] T. Ogawa, T. Kuzuya, Y. Hamanaka, K. Sumiyama, Synthesis of Ag-In binary sulfide nanoparticles-structural tuning and their photoluminescence properties, J. Mater. Chem. 20 (2010) 2226, https://doi.org/10.1039/b920732e.
[223] T. Bai, C. Li, F. Li, L. Zhao, Z. Wang, H. Huang, C. Chen, Y. Han, Z. Shi, S. Feng, A simple solution-phase approach to synthesize high quality ternary $AgInSe_2$ and band gap tunable quaternary $AgIn(S_{1-x}Se_x)_2$ nanocrystals, Nanoscale 6 (2014) 6782, https://doi.org/10.1039/c4nr00233d.
[224] A.M. Smith, M.C. Mancini, S. Nie, Second window for in vivo imaging, Nat. Nanotechnol. 4 (2009) 710–711, https://doi.org/10.1038/nnano.2009.326.
[225] M. Dai, S. Ogawa, T. Kameyama, K. Okazaki, A. Kudo, S. Kuwabata, Y. Tsuboi, T. Torimoto, Tunable photoluminescence from the visible to near-infrared wavelength region of non-stoichiometric $AgInS_2$ nanoparticles, J. Mater. Chem. 22 (2012) 12851, https://doi.org/10.1039/c2jm31463k.
[226] T. Kameyama, Y. Ishigami, H. Yukawa, T. Shimada, Y. Baba, T. Ishikawa, S. Kuwabata, T. Torimoto, Crystal phase-controlled synthesis of rod-shaped $AgInTe_2$ nanocrystals for in vivo imaging in the near-infrared wavelength region, Nanoscale 8 (2016) 5435–5440, https://doi.org/10.1039/C5NR07532G.
[227] L. Canham, Introductory lecture: origins and applications of efficient visible photoluminescence from silicon-based nanostructures, Faraday Discuss. 222 (2020) 10–81, https://doi.org/10.1039/D0FD00018C.
[228] T. Takagahara, K. Takeda, Theory of the quantum confinement effect on excitons in quantum dots of indirect-gap materials, Phys. Rev. B. 46 (1992) 15578–15581, https://doi.org/10.1103/PhysRevB.46.15578.
[229] M. Montalti, A. Cantelli, G. Battistelli, Nanodiamonds and silicon quantum dots: ultrastable and biocompatible luminescent nanoprobes for long-term bioimaging, Chem. Soc. Rev. 44 (2015) 4853–4921, https://doi.org/10.1039/C4CS00486H.
[230] W.M. Girma, M.Z. Fahmi, A. Permadi, M.A. Abate, J.-Y. Chang, Synthetic strategies and biomedical applications of I-III-VI ternary quantum dots, J. Mater. Chem. B. 5 (2017) 6193–6216, https://doi.org/10.1039/C7TB01156C.
[231] A.M. Smith, S. Nie, Chemical analysis and cellular imaging with quantum dots, Analyst. 129 (2004) 672, https://doi.org/10.1039/b404498n.
[232] J. Kolny-Olesiak, H. Weller, Synthesis and application of colloidal $CuInS_2$ semiconductor nanocrystals, ACS Appl. Mater. Interfaces. 5 (2013) 12221–12237, https://doi.org/10.1021/am404084d.
[233] T. Omata, K. Nose, S. Otsuka-Yao-Matsuo, Size dependent optical band gap of ternary I-III-VI_2 semiconductor nanocrystals, J. Appl. Phys. 105 (2009), https://doi.org/10.1063/1.3103768.
[234] M. Booth, A.P. Brown, S.D. Evans, K. Critchley, Determining the concentration of $CuInS_2$ quantum dots from the size-dependent molar extinction coefficient, Chem. Mater. 24 (2012) 2064–2070, https://doi.org/10.1021/cm300227b.
[235] L. Qin, D. Li, Z. Zhang, K. Wang, H. Ding, R. Xie, W. Yang, The determination of extinction coefficient of $CuInS_2$, and $ZnCuInS_3$ multinary nanocrystals, Nanoscale 4 (2012) 6360, https://doi.org/10.1039/c2nr31794j.
[236] J.S. Niezgoda, M.A. Harrison, J.R. McBride, S.J. Rosenthal, Novel synthesis of chalcopyrite $Cu_xIn_yS_2$ quantum dots with tunable localized surface plasmon resonances, Chem. Mater. 24 (2012) 3294–3298, https://doi.org/10.1021/cm3021462.
[237] G. Morselli, M. Villa, A. Fermi, K. Critchley, P. Ceroni, Luminescent copper indium sulfide (CIS) quantum dots for bioimaging applications, Nanoscale Horiz. 6 (2021) 676–695, https://doi.org/10.1039/D1NH00260K.
[238] S.O.M. Hinterding, M.J.J. Mangnus, P.T. Prins, H.J. Jöbsis, S. Busatto, D. Vanmaekelbergh, C. de Mello Donega, F.T. Rabouw, Unusual spectral diffusion of single $CuInS_2$ quantum dots sheds light on the mechanism of radiative decay, Nano Lett. 21 (2021) 658–665, https://doi.org/10.1021/acs.nanolett.0c04239.
[239] K.E. Knowles, H.D. Nelson, T.B. Kilburn, D.R. Gamelin, Singlet-triplet splittings in the luminescent excited states of colloidal Cu^+ :CdSe, Cu^+ :InP, and $CuInS_2$ nanocrystals: Charge-transfer configurations and self-trapped excitons, J. Am. Chem. Soc. 137 (2015) 13138–13147, https://doi.org/10.1021/jacs.5b08547.
[240] A. Anand, M.L. Zaffalon, G. Gariano, A. Camellini, M. Gandini, R. Brescia, C. Capitani, F. Bruni, V. Pinchetti, M. Zavelani-Rossi, F. Meinardi, S.A. Crooker, S. Brovelli, Evidence for the band-edge exciton of $CuInS_2$ nanocrystals enables record efficient large-area luminescent solar concentrators, Adv. Funct. Mater. 30 (2020) 1906629, https://doi.org/10.1002/adfm.201906629.
[241] A.D.P. Leach, J.E. Macdonald, Optoelectronic properties of $CuInS_2$ nanocrystals and their origin, J. Phys. Chem. Lett. 7 (2016) 572–583, https://doi.org/10.1021/acs.jpclett.5b02211.
[242] A. Skripka, D. Mendez-Gonzalez, R. Marin, E. Ximendes, B. del Rosal, D. Jaque, P. Rodríguez-Sevilla, Near infrared bioimaging and biosensing with semiconductor and rare-earth nanoparticles: Recent developments in multifunctional nanomaterials, Nanoscale Adv. 3 (2021) 6310–6329, https://doi.org/10.1039/D1NA00502B.
[243] P. Reiss, M. Carrière, C. Lincheneau, L. Vaure, S. Tamang, synthesis of semiconductor nanocrystals, focusing on nontoxic and earth-abundant

materials, Chem. Rev. 116 (2016) 10731–10819, https://doi.org/10.1021/acs.chemrev.6b00116.
[244] S. Adam, D.V. Talapin, H. Borchert, A. Lobo, C. McGinley, A.R.B. de Castro, M. Haase, H. Weller, T. Möller, The effect of nanocrystal surface structure on the luminescence properties: Photoemission study of HF-etched InP nanocrystals, J. Chem. Phys. 123 (2005), https://doi.org/10.1063/1.2004901.
[245] Y. Kim, S. Ham, H. Jang, J.H. Min, H. Chung, J. Lee, D. Kim, E. Jang, Bright and uniform green light emitting InP/ZnSe/ZnS quantum dots for wide color gamut displays, ACS Appl. Nano Mater. 2 (2019) 1496–1504, https://doi.org/10.1021/acsanm.8b02063.
[246] H. Lu, G.M. Carroll, N.R. Neale, M.C. Beard, Infrared quantum dots: Progress, challenges, and opportunities, ACS Nano (2019), https://doi.org/10.1021/acsnano.8b09815.
[247] N. Órdenes-Aenishanslins, G. Anziani-Ostuni, C.P. Quezada, R. Espinoza-González, D. Bravo, J.M. Pérez-Donoso, Biological synthesis of CdS/CdSe core/shell nanoparticles and its application in quantum dot sensitized solar cells, Front. Microbiol. 10 (2019) 1587, https://doi.org/10.3389/fmicb.2019.01587.
[248] G. Yordanov, M. Simeonova, R. Alexandrova, H. Yoshimura, C. Dushkin, Quantum dots tagged poly(alkylcyanoacrylate) nanoparticles intended for bioimaging applications, Colloids Surf. A Physicochem. Eng. Asp. 339 (2009) 199–205, https://doi.org/10.1016/j.colsurfa.2009.02.027.
[249] V. Biju, D. Muraleedharan, K. Nakayama, Y. Shinohara, T. Itoh, Y. Baba, M. Ishikawa, Quantum dot-insect neuropeptide conjugates for fluorescence imaging, transfection, and nucleus targeting of living cells, Langmuir 23 (2007) 10254–10261, https://doi.org/10.1021/la7012705.
[250] A. Anas, T. Okuda, N. Kawashima, K. Nakayama, T. Itoh, M. Ishikawa, V. Biju, Clathrin-mediated endocytosis of quantum dot− peptide conjugates in living cells, ACS Nano 3 (2009) 2419–2429, https://doi.org/10.1021/nn900663r.
[251] N. Kawashima, K. Nakayama, K. Itoh, T. Itoh, M. Ishikawa, V. Biju, Reversible dimerization of EGFR revealed by single-molecule fluorescence imaging using quantum dots, Chem. Eur. J. 16 (2010) 1186–1192, https://doi.org/10.1002/chem.200902963.
[252] A. Anas, H. Akita, H. Harashima, T. Itoh, M. Ishikawa, V. Biju, Photosensitized breakage and damage of DNA by CdSe− ZnS quantum dots, J. Phys. Chem. B 112 (2008) 10005–10011, https://doi.org/10.1021/jp8018606.
[253] V. Biju, A. Anas, H. Akita, E.S. Shibu, T. Itoh, H. Harashima, M. Ishikawa, FRET from quantum dots to photodecompose undesired acceptors and report the condensation and decondensation of plasmid DNA, ACS Nano 6 (2012) 3776–3788, https://doi.org/10.1021/nn2048608.
[254] E.S. Shibu, K. Ono, S. Sugino, A. Nishioka, A. Yasuda, Y. Shigeri, S. Wakida, M. Sawada, V. Biju, Photouncaging nanoparticles for MRI and fluorescence imaging in vitro and in vivo, ACS Nano 7 (2013) 9851–9859, https://doi.org/10.1021/nn4043699.
[255] V. Biju, M. Hamada, K. Ono, S. Sugino, T. Ohnishi, E.S. Shibu, S. Yamamura, M. Sawada, S. Nakanishi, Y. Shigeri, S. Wakida, Nanoparticles speckled by ready-to-conjugate lanthanide complexes for multimodal imaging, Nanoscale 7 (2015) 14829–14837, https://doi.org/10.1039/C5NR00959F.
[256] J. Riegler, T. Nann, Application of luminescent nanocrystals as labels for biological molecules, Anal. Bioanal. Chem. 379 (2004), https://doi.org/10.1007/s00216-004-2706-y.
[257] S. Jung, X. Chen, Quantum dot-dye conjugates for biosensing, imaging, and therapy, Adv. Healthcare Mater. 7 (2018) 1800252, https://doi.org/10.1002/adhm.201800252.
[258] K.-T. Yong, W.-C. Law, I. Roy, Z. Jing, H. Huang, M.T. Swihart, P.N. Prasad, Aqueous phase synthesis of CdTe quantum dots for biophotonics, J. Biophoton. 4 (2011) 9–20, https://doi.org/10.1002/jbio.201000080.
[259] L.L. Chen, L. Zhao, Z.G. Wang, S.L. Liu, D.W. Pang, Near-infrared-II quantum dots for in Vivo imaging and cancer therapy, Small 18 (2022), https://doi.org/10.1002/SMLL.202104567.
[260] N. Xu, M. Piao, K. Arkin, L. Ren, J. Zhang, J. Hao, Y. Zheng, Q. Shang, Imaging of water soluble CdTe/CdS core-shell quantum dots in inhibiting multidrug resistance of cancer cells, Talanta. 201 (2019) 309–316, https://doi.org/10.1016/j.talanta.2019.04.021.
[261] J. Wang, H. Han, Hydrothermal synthesis of high-quality type-II CdTe/CdSe quantum dots with near-infrared fluorescence, J Colloid. Interface Sci. 351 (2010) 83–87, https://doi.org/10.1016/j.jcis.2010.07.025.
[262] M. Alizadeh-Ghodsi, M. Pourhassan-Moghaddam, A. Zavari-Nematabad, B. Walker, N. Annabi, A. Akbarzadeh, State-of-the-art and trends in synthesis, properties, and application of quantum dots-based nanomaterials, Part. Part. Syst. Charact. 36 (2019) 1800302, https://doi.org/10.1002/ppsc.201800302.
[263] V. Biju, S. Mundayoor, R.V. Omkumar, A. Anas, M. Ishikawa, Bioconjugated quantum dots for cancer research: present status, prospects and remaining issues, Biotechnol. Adv. 28 (2010) 199–213, https://doi.org/10.1016/j.biotechadv.2009.11.007.
[264] E.S. Shibu, M. Hamada, N. Murase, V. Biju, Nanomaterials formulations for photothermal and photodynamic therapy of cancer, J. Photochem. Photobiol. C: Photochem. Rev. 15 (2013) 53–72.
[265] A.-L. Sun, Y.-F. Zhang, X.-N. Wang, Sensitive voltammetric determination of DNA via a target-induced strand-displacement reaction using quantum dot-labeled probe DNA, Microchim Acta. 182 (2015) 1403–1410, https://doi.org/10.1007/s00604-015-1467-y.
[266] L. Shi, V. De Paoli, N. Rosenzweig, Z. Rosenzweig, Synthesis and application of quantum dots FRET-based protease sensors, J. Am. Chem. Soc. 128 (2006) 10378–10379, https://doi.org/10.1021/ja063509o.
[267] Ł. Rodzik-Czałka, J. Lewandowska-Łańcucka, V. Gatta, I. Venditti, I. Fratoddi, M. Szuwarzyński, M. Romek, M. Nowakowska, Nucleobases functionalized quantum dots and gold nanoparticles bioconjugates as a fluorescence resonance energy transfer (FRET) system-synthesis, characterization and potential applications, J Colloid. Interface Sci. 514 (2018) 479–490, https://doi.org/10.1016/j.jcis.2017.12.060.
[268] A. Banerjee, T. Pons, N. Lequeux, B. Dubertret, Quantum dots–DNA bioconjugates: Synthesis to applications, Interface Focus 6 (2016) 20160064, https://doi.org/10.1098/rsfs.2016.0064.
[269] E. Sharon, R. Freeman, I. Willner, CdSe/ZnS quantum dots-G-quadruplex/hemin hybrids as optical DNA sensors and aptasensors, Anal. Chem. 82 (2010) 7073–7077, https://doi.org/10.1021/ac101456x.
[270] G.-L. Wang, P.-P. Yu, J.-J. Xu, H.-Y. Chen, A label-free photoelectrochemical immunosensor based on water-soluble CdS quantum dots, J. Phys. Chem. C. 113 (2009) 11142–11148, https://doi.org/10.1021/jp902069s.
[271] Z. Yin, R. Cui, Y. Liu, L. Jiang, J.-J. Zhu, Ultrasensitive electrochemical immunoassay based on cadmium ion-functionalized PSA@PAA nanospheres, Biosens. Bioelectron. 25 (2010) 1319–1324, https://doi.org/10.1016/j.bios.2009.10.021.
[272] S. Singh, V. Kaur, N. Kumar, M. Garg, S.K. Pandey, V.K. Meena, Cadmium chalcogenide derived fluorescent quanta-sensor for melamine detection, Sens. Actuators B Chem. 273 (2018) 505–510, https://doi.org/10.1016/j.snb.2018.06.063.
[273] D. Tiwari, S.-I. Tanaka, Y. Inouye, K. Yoshizawa, T. Watanabe, T. Jin, Synthesis and characterization of anti-HER2 antibody conjugated CdSe/CdZnS quantum dots for fluorescence imaging of breast cancer cells, Sens. 9 (2009) 9332–9354, https://doi.org/10.3390/s91109332.
[274] J.K. Jaiswal, H. Mattoussi, J.M. Mauro, S.M. Simon, Long-term multiple color imaging of live cells using quantum dot bioconjugates, Nat. Biotechnol. 21 (2003) 47–51, https://doi.org/10.1038/nbt767.
[275] G. Singh, M. Kumar, U. Soni, V. Arora, V. Bansal, D. Gupta, M. Bhat, A.K. Dinda, S. Sapra, H. Singh, Cancer cell targeting using folic acid/anti-HER2 antibody conjugated fluorescent CdSe/CdS/ZnS-mercaptopropionic acid and CdTe-mercaptosuccinic acid quantum dots, J Nanosci. Nanotechnol. 16 (2016) 130–143, https://doi.org/10.1166/jnn.2016.10825.
[276] H.-X. Xia, X.-Q. Yang, J.-T. Song, J. Chen, M.-Z. Zhang, D.-M. Yan, L. Zhang, M.-Y. Qin, L.-Y. Bai, Y.-D. Zhao, Z.-Y. Ma, Folic acid-conjugated silica-coated gold nanorods and quantum dots for dual-modality CT and fluorescence imaging and photothermal therapy, J. Mater. Chem. B. 2 (2014) 1945, https://doi.org/10.1039/c3tb21591a.
[277] R.G. Aswathy, Y. Yoshida, T. Maekawa, D.S. Kumar, Near-infrared quantum dots for deep tissue imaging, Anal. Bioanal. Chem. 397 (2010) 1417–1435, https://doi.org/10.1007/s00216-010-3643-6.
[278] F.P. García de Arquer, D.V. Talapin, V.I. Klimov, Y. Arakawa, M. Bayer, E.H. Sargent, Semiconductor quantum dots: Technological progress and future challenges, Science 373 (2021) eaaz8541, https://doi.org/10.1126/science.aaz8541.
[279] W. Wang, Z. Liu, X. Lan, Quantum dot-based simultaneous multicolor imaging, mol imaging Biol. 22 (2020) 820–831, https://doi.org/10.1007/s11307-019-01432-4.
[280] J.S. Kim, K.J. Cho, T.H. Tran, M.d. Nurunnabi, T.H. Moon, S.M. Hong, Y. Lee, In vivo NIR imaging with CdTe/CdSe quantum dots entrapped in PLGA nanospheres, J. Colloid Interface Sci. 353 (2011) 363–371, https://doi.org/10.1016/j.jcis.2010.08.053.
[281] M. Walling, J. Novak, J.R.E. Shepard, Quantum dots for live cell and in vivo imaging, Int. J. Mol. Sci. 10 (2009) 441–491, https://doi.org/10.3390/ijms10020441.
[282] Q. Bai, Z. Zhao, H. Sui, J. Chen, X. Xie, F. Wen, The preparation and application of dendrimer modified CdTe/CdS near infrared quantum dots for brain cancer cells imaging, Appl. Sci. 5 (2015) 1076–1085, https://doi.org/10.3390/app5041076.
[283] M. Zhang, J. Yue, R. Cui, Z. Ma, H. Wan, F. Wang, S. Zhu, Y. Zhou, Y. Kuang, Y. Zhong, D.-W. Pang, H. Dai, Bright quantum dots emitting at ~1,600 nm in the NIR-IIb window for deep tissue fluorescence imaging, Proc. Natl. Acad. Sci. U. S.A. 115 (2018) 6590–6595, https://doi.org/10.1073/pnas.1806153115.
[284] W. Cai, D.-W. Shin, K. Chen, O. Gheysens, Q. Cao, S.X. Wang, S.S. Gambhir, X. Chen, Peptide-labeled near-infrared quantum dots for imaging tumor vasculature in living subjects, Nano Lett. 6 (2006) 669–676, https://doi.org/10.1021/nl052405t.
[285] V. Biju, T. Itoh, A. Anas, A. Sujith, M. Ishikawa, Semiconductor quantum dots and metal nanoparticles: Syntheses, optical properties, and biological applications, Anal. Bioanal. Chem. 391 (2008) 2469–2495, https://doi.org/10.1007/s00216-008-2185-7.
[286] H. M. Gil, T. W. Price, K. Chelani, J.-S.G. Bouillard, S. D. J. Calaminus, G. J. Stasiuk, NIR-quantum dots in biomedical imaging and their future, iScience 24 (2021) 102189. https://doi.org/10.1016/j.isci.2021.102189.
[287] N.J. Hunt, G.P. Lockwood, S.W.S. Kang, L.J. Westwood, C. Limantoro, W. Chrzanowski, P.A.G. McCourt, Z. Kuncic, D.G. Le Couteur, V.C. Cogger, Quantum dot nanomedicine formulations dramatically improve pharmacological properties and alter uptake pathways of metformin and nicotinamide mononucleotide in aging mice, ACS Nano 15 (2021) 4710–4727, https://doi.org/10.1021/acsnano.0c09278.
[288] R. Tang, J. Xue, B. Xu, D. Shen, G.P. Sudlow, S. Achilefu, Tunable ultrasmall visible-to-extended near-infrared emitting silver sulfide quantum dots for integrin-targeted cancer imaging, ACS Nano 9 (2015) 220–230, https://doi.org/10.1021/nn5071183.
[289] C.-N. Zhu, G. Chen, Z.-Q. Tian, W. Wang, W.-Q. Zhong, Z. Li, Z.-L. Zhang, D.-W. Pang, Near-infrared fluorescent Ag_2Se-cetuximab nanoprobes for targeted

imaging and therapy of cancer, Small 13 (2017) 1602309, https://doi.org/10.1002/smll.201602309.
[290] X.-L. Ge, B. Huang, Z.-L. Zhang, X. Liu, M. He, Z. Yu, B. Hu, R. Cui, X.-J. Liang, D.-W. Pang, Glucose-functionalized near-infrared Ag_2Se quantum dots with renal excretion ability for long-term *in vivo* tumor imaging, J. Mater. Chem. B. 7 (2019) 5782–5788, https://doi.org/10.1039/C9TB01112A.
[291] J. Zhang, Y. Lin, H. Zhou, H. He, J. Ma, M. Luo, Z. Zhang, D. Pang, Cell membrane-camouflaged NIR II fluorescent Ag_2Te quantum dots-based nanobioprobes for enhanced in vivo homotypic tumor imaging, Adv. Healthcare Mater. 8 (2019) 1900341, https://doi.org/10.1002/adhm.201900341.
[292] Y. Ogihara, H. Yukawa, T. Kameyama, H. Nishi, D. Onoshima, T. Ishikawa, T. Torimoto, Y. Baba, Labeling and in vivo visualization of transplanted adipose tissue-derived stem cells with safe cadmium-free aqueous ZnS coating of ZnS-$AgInS_2$ nanoparticles, Sci. Rep. 7 (2017) 40047, https://doi.org/10.1038/srep40047.
[293] C. Li, W. Li, H. Liu, Y. Zhang, G. Chen, Z. Li, Q. Wang, An activatable NIR-II nanoprobe for in vivo Eerly real-time diagnosis of traumatic brain injury, Angew. Chem. Int. Ed. 59 (2020) 247–252, https://doi.org/10.1002/anie.201911803.
[294] S. Sarkar, P. Le, J. Geng, Y. Liu, Z. Han, M.U. Zahid, D. Nall, Y. Youn, P.R. Selvin, A.M. Smith, Short-wave infrared quantum dots with compact sizes as molecular probes for fluorescence microscopy, J. Am. Chem. Soc. 142 (2020) 3449–3462, https://doi.org/10.1021/jacs.9b11567.
[295] G.-T. Yu, M.-Y. Luo, H. Li, S. Chen, B. Huang, Z.-J. Sun, R. Cui, M. Zhang, Molecular targeting nanoprobes with non-overlap emission in the second near-infrared window for *in Vivo* two-color colocalization of immune cells, ACS Nano 13 (2019) 12830–12839, https://doi.org/10.1021/acsnano.9b05038.
[296] W. Jeong, J. Bu, L.J. Kubiatowicz, S.S. Chen, Y. Kim, S. Hong, Peptide-nanoparticle conjugates: A next generation of diagnostic and therapeutic platforms?, Nano Converg 5 (2018) 38, https://doi.org/10.1186/s40580-018-0170-1.
[297] B. Purushothaman, J.M. Song, Ag_2S quantum dot theragnostics, Biomater. Sci. 9 (2021) 51–69, https://doi.org/10.1039/D0BM01576H.
[298] C.M. Dundas, D. Demonte, S. Park, Streptavidin–biotin technology: Improvements and innovations in chemical and biological applications, Appl. Microbiol. Biotechnol. 97 (2013) 9343–9353, https://doi.org/10.1007/s00253-013-5232-z.
[299] J. Choi, N.S. Wang, V. Reipa, Conjugation of the photoluminescent silicon nanoparticles to streptavidin, Bioconjugate Chem. 19 (2008) 680–685, https://doi.org/10.1021/bc700373y.
[300] C. Ding, Y. Huang, Z. Shen, X. Chen, Synthesis and bioapplications of Ag_2S quantum dots with near-infrared fluorescence, Adv. Mater. 33 (2021) 2007768, https://doi.org/10.1002/adma.202007768.
[301] F.D. Duman, I. Hocaoglu, D.G. Ozturk, D. Gozuacik, A. Kiraz, H. Yagci Acar, Highly luminescent and cytocompatible cationic Ag_2S NIR-emitting quantum dots for optical imaging and gene transfection, Nanoscale 7 (2015) 11352–11362, https://doi.org/10.1039/C5NR00189G.
[302] D. Yan, Y. He, Y. Ge, G. Song, Fluorescence "turn on-off" detection of heparin and heparinase I based on the near-infrared emission polyethyleneimine capped Ag_2S quantum dots, Sens. Actuators B Chem. 240 (2017) 863–869, https://doi.org/10.1016/j.snb.2016.09.058.
[303] Y. Peng, Y.P. Dong, M.M. Ai, H.C. Ding, Electrogenerated chemiluminescence of Ag_2Te quantum dots and its application in sensitive detection of catechol, J. Lumin. 190 (2017) 221–227, https://doi.org/10.1016/j.jlumin.2017.05.051.
[304] B.M.M. May, S. Parani, O.S. Oluwafemi, Detection of ascorbic acid using green synthesized $AgInS_2$ quantum dots, Mat. Lett. 236 (2019) 432–435, https://doi.org/10.1016/j.matlet.2018.10.155.
[305] S. Yan, L. Zhang, Y. Tang, Y. Lv, Synthesis of water-soluble Ag_2Se QDs as a novel resonance Rayleigh scattering sensor for highly sensitive and selective ConA detection, Analyst. 139 (2014) 4210–4215, https://doi.org/10.1039/C4AN00579A.
[306] E. Bagheri, L. Ansari, K. Abnous, S.M. Taghdisi, P. Ramezani, M. Ramezani, M. Alibolandi, Silica-quantum dot nanomaterials as a versatile sensing platform, Crit. Rev. Anal. Chem. 51 (2021) 687–708, https://doi.org/10.1080/10408347.2020.1768358.
[307] Z. Wang, Y. Ma, X. Yu, Q. Niu, Z. Han, H. Wang, T. Li, D. Fu, S. Achilefu, Z. Qian, Y. Gu, Targeting CXCR4-CXCL12 axis for visualizing, predicting, and inhibiting breast cancer metastasis with theranostic AMD3100-Ag_2S quantum dot probe, Adv. Funct. Mater. 28 (2018) 1800732, https://doi.org/10.1002/adfm.201800732.
[308] Z. Zhang, C. Ni, W. Chen, P. Wu, Z. Wang, J. Yin, J. Huang, F. Qiu, Expression of CXCR4 and breast cancer prognosis: A systematic review and meta-analysis, BMC Cancer 14 (2014) 49, https://doi.org/10.1186/1471-2407-14-49.
[309] Y. Xing, Q. Chaudry, C. Shen, K.Y. Kong, H.E. Zhau, L.W. Chung, J.A. Petros, R.M. O'Regan, M.V. Yezhelyev, J.W. Simons, M.D. Wang, S. Nie, Bioconjugated quantum dots for multiplexed and quantitative immunohistochemistry, Nat. Protoc. 2 (2007) 1152–1165, https://doi.org/10.1038/nprot.2007.107.
[310] M.Z. Fahmi, J.-Y. Chang, Potential application of oleylamine-encapsulated $AgInS_2$-ZnS quantum dots for cancer cell labeling, Procedia Chem. 18 (2016) 112–121, https://doi.org/10.1016/j.proche.2016.01.018.
[311] M. Kamimura, Semiconductor quantum dots for NIR bioimaging, in: K. Soga, M. Umezawa, K. Okubo (Eds.), Transparency in Biology, Springer Singapore, Singapore, 2021, pp. 73–84, https://doi.org/10.1007/978-981-15-9627-8_4.
[312] A.J.A. KerÃ, The biotin synthesis of HeLa cells in vitro, Cancer Res. 32 (1972) 119–124.
[313] H. Chen, B. Li, M. Zhang, K. Sun, Y. Wang, K. Peng, M. Ao, Y. Guo, Y. Gu, Characterization of tumor-targeting Ag_2S quantum dots for cancer imaging and therapy in vivo, Nanoscale 6 (2014) 12580–12590, https://doi.org/10.1039/C4NR03613A.
[314] R. Tian, Z. Shen, Z. Zhou, J. Munasinghe, X. Zhang, O. Jacobson, M. Zhang, G. Niu, D. Pang, R. Cui, S. Zhu, X. Chen, Ultrasmall quantum dots with broad-spectrum metal doping ability for trimodal molecular imaging, Adv. Funct. Mater. 29 (2019) 1901671, https://doi.org/10.1002/adfm.201901671.
[315] Q. Wen, Y. Zhang, C. Li, S. Ling, X. Yang, G. Chen, Y. Yang, Q. Wang, NIR-II fluorescent self-assembled peptide nanochain for ultrasensitive detection of peritoneal metastasis, Angew. Chem. 131 (2019) 11117–11122, https://doi.org/10.1002/ange.201905643.
[316] X. Yin, X. Li, C. Zhu, X. Lin, Z. Xie, Integration of fluorescence/photoacoustic imaging and targeted chemo/photothermal therapy with Ag_2Se@BSA-RGD nanodots, New J. Chem. 44 (2020) 4850–4857, https://doi.org/10.1039/D0NJ00240B.
[317] Y.-P. Gu, R. Cui, Z.-L. Zhang, Z.-X. Xie, D.-W. Pang, Ultrasmall near-infrared Ag_2Se quantum dots with tunable fluorescence for *in vivo* imaging, J. Am. Chem. Soc. 134 (2012) 79–82, https://doi.org/10.1021/ja2089553.
[318] T. Kameyama, H. Yamauchi, T. Yamamoto, T. Mizumaki, H. Yukawa, M. Yamamoto, S. Ikeda, T. Uematsu, Y. Baba, S. Kuwabata, T. Torimoto, Tailored photoluminescence properties of Ag(In, Ga)S_e2 quantum dots for near-infrared *in vivo* imaging, ACS Appl. Nano Mater. 3 (2020) 3275–3287, https://doi.org/10.1021/acsanm.9b02608.
[319] K. Li, W. Dong, Q. Liu, G. Lv, M. Xie, X. Sun, L. Qiu, J. Lin, A biotin receptor-targeted silicon(IV) phthalocyanine for in vivo tumor imaging and photodynamic therapy, J. Photochem. Photobiol. B, Biol. 190 (2019) 1–7, https://doi.org/10.1016/j.jphotobiol.2018.09.001.
[320] F. Erogbogbo, K.-T. Yong, I. Roy, G. Xu, P.N. Prasad, M.T. Swihart, Biocompatible luminescent silicon quantum dots for imaging of cancer cells, ACS Nano 2 (2008) 873–878, https://doi.org/10.1021/nn700319z.
[321] M. Rosso-Vasic, E. Spruijt, Z. Popović, K. Overgaag, B. van Lagen, B. Grandidier, D. Vanmaekelbergh, D. Domínguez-Gutiérrez, L. De Cola, H. Zuilhof, Amine-terminated silicon nanoparticles: Synthesis, optical properties and their use in bioimaging, J. Mater. Chem. 19 (2009) 5926, https://doi.org/10.1039/b902671a.
[322] A.D. Frankel, C.O. Pabo, Cellular uptake of the tat protein from human immunodeficiency virus, Cell 55 (1988) 1189–1193, https://doi.org/10.1016/0092-8674(88)90263-2.
[323] S. Futaki, S. Goto, Y. Sugiura, Membrane permeability commonly shared among arginine-rich peptides, J. Mol. Recognit. 16 (2003) 260–264, https://doi.org/10.1002/jmr.635.
[324] X. Gao, X. Liu, Z. Lin, S. Liu, X. Su, $CuInS_2$ quantum dots as a near-infrared fluorescent probe for detecting thrombin in human serum, Analyst. 137 (2012) 5620, https://doi.org/10.1039/c2an35888c.
[325] S. Liu, W. Na, S. Pang, F. Shi, X. Su, A label-free fluorescence detection strategy for lysozyme assay using $CuInS_2$ quantum dots, Analyst. 139 (2014) 3048, https://doi.org/10.1039/c4an00160e.
[326] E.S. Speranskaya, N.V. Beloglazova, S. Abé, T. Aubert, P.F. Smet, D. Poelman, I. Y. Goryacheva, S. De Saeger, Z. Hens, Hydrophilic, Bright $CuInS_2$ quantum dots as Cd-free fluorescent labels in quantitative immunoassay, Langmuir 30 (2014) 7567–7575, https://doi.org/10.1021/la501268b.
[327] X. An, Y. Zhang, J. Wang, D. Kong, X. He, L. Chen, Y. Zhang, The preparation of $CuInS_2$-ZnS-glutathione quantum dots and their application on the sensitive determination of cytochrome *c* and imaging of HeLa cells, ACS Omega 6 (2021) 17501–17509, https://doi.org/10.1021/acsomega.1c01983.
[328] M.F. Foda, L. Huang, F. Shao, H.-Y. Han, Biocompatible and highly luminescent near-infrared $CuInS_2$/ZnS quantum dots embedded silica beads for cancer cell imaging, ACS Appl. Mater. Interfaces. 6 (2014) 2011–2017, https://doi.org/10.1021/am4050772.
[329] C. Zhao, Z. Bai, X. Liu, Y. Zhang, B. Zou, H. Zhong, Small GSH-capped $CuInS_2$ quantum dots: MPA-assisted aqueous phase transfer and bioimaging applications, ACS Appl. Mater. Interfaces. 7 (2015) 17623–17629, https://doi.org/10.1021/acsami.5b05503.
[330] Z. Liu, N. Chen, C. Dong, W. Li, W. Guo, H. Wang, S. Wang, J. Tan, Y. Tu, J. Chang, Facile construction of near infrared fluorescence nanoprobe with amphiphilic protein-polymer bioconjugate for targeted cell imaging, ACS Appl. Mater. Interfaces. 7 (2015) 18997–19005, https://doi.org/10.1021/acsami.5b05406.
[331] L.C. Spangler, R. Chu, L. Lu, C.J. Kiely, B.W. Berger, S. McIntosh, Enzymatic biomineralization of biocompatible $CuInS_2$, (CuInZn)S_2 and $CuInS_2$/ZnS core/shell nanocrystals for bioimaging, Nanoscale 9 (2017) 9340–9351, https://doi.org/10.1039/C7NR02852K.
[332] S. Mallick, P. Kumar, A.L. Koner, Freeze-resistant cadmium-free quantum dots for live-cell imaging, ACS Appl. Nano Mater. 2 (2019) 661–666, https://doi.org/10.1021/acsanm.8b02231.
[333] A. Arshad, R. Akram, S. Iqbal, F. Batool, B. Iqbal, B. Khalid, A.U. Khan, Aqueous synthesis of tunable fluorescent, semiconductor $CuInS_2$ quantum dots for bioimaging, Arab. J. Chem. 12 (2019) 4840–4847, https://doi.org/10.1016/j.arabjc.2016.10.002.
[334] E. Dutková, Z.L. Bujňáková, M. Kello, J. Mojžiš, O. Skurikhina, J. Briančin, Chitosan capped $CuInS_2$ and $CuInS_2$/ZnS by wet stirred media milling: In vitro verification of their potential bio-imaging applications, Appl. Nanosci. 10 (2020) 4661–4671, https://doi.org/10.1007/s13204-020-01530-8.

[335] L. Li, T.J. Daou, I. Texier, T.T. Kim Chi, N.Q. Liem, P. Reiss, Highly luminescent $CuInS_2$/ZnS core/shell nanocrystals: Cadmium-free quantum dots for in vivo imaging, Chem. Mater. 21 (2009) 2422–2429, https://doi.org/10.1021/cm900103b.
[336] K.-T. Yong, I. Roy, R. Hu, H. Ding, H. Cai, J. Zhu, X. Zhang, E.J. Bergey, P.N. Prasad, Synthesis of ternary $CuInS_2$/ZnS quantum dot bioconjugates and their applications for targeted cancer bioimaging, Integr. Biol. 2 (2010) 121, https://doi.org/10.1039/b916663g.
[337] E.-M. Kim, S.T. Lim, M.-H. Sohn, H.-J. Jeong, Facile synthesis of near-infrared $CuInS_2$/ZnS quantum dots and glycol-chitosan coating for in vivo imaging, J. Nanopart. Res. 19 (2017) 251, https://doi.org/10.1007/s11051-017-3944-1.
[338] L. Liu, R. Hu, W.-C. Law, I. Roy, J. Zhu, L. Ye, S. Hu, X. Zhang, K.-T. Yong, Optimizing the synthesis of red- and near-infrared $CuInS_2$ and $AgInS_2$ semiconductor nanocrystals for bioimaging, Analyst. 138 (2013) 6144, https://doi.org/10.1039/c3an01030a.
[339] K. Yu, P. Ng, J. Ouyang, M.B. Zaman, A. Abulrob, T.N. Baral, D. Fatehi, Z.J. Jakubek, D. Kingston, X. Wu, X. Liu, C. Hebert, D.M. Leek, D.M. Whitfield, Low-temperature approach to highly emissive copper indium sulfide colloidal nanocrystals and their bioimaging applications, ACS Appl. Mater. Interfaces. 5 (2013) 2870–2880, https://doi.org/10.1021/am302951k.
[340] M.G. Panthani, T.A. Khan, D.K. Reid, D.J. Hellebusch, M.R. Rasch, J.A. Maynard, B.A. Korgel, In vivo whole animal fluorescence imaging of a microparticle-based oral vaccine containing ($CuInSe_xS_{2-x}$)/ZnS core/shell quantum dots, Nano Lett. 13 (2013) 4294–4298, https://doi.org/10.1021/nl402054w.
[341] W. Lian, D. Tu, P. Hu, X. Song, Z. Gong, T. Chen, J. Song, Z. Chen, X. Chen, Broadband excitable NIR-II luminescent nano-bioprobes based on $CuInSe_2$ quantum dots for the detection of circulating tumor cells, Nano Today 35 (2020), https://doi.org/10.1016/j.nantod.2020.100943.
[342] D.J. Bharali, D.W. Lucey, H. Jayakumar, H.E. Pudavar, P.N. Prasad, Folate-receptor-mediated delivery of InP quantum dots for bioimaging using confocal and two-photon microscopy, J. Am. Chem. Soc. 127 (2005) 11364–11371, https://doi.org/10.1021/ja051455x.
[343] K.-T. Yong, H. Ding, I. Roy, W.-C. Law, E.J. Bergey, A. Maitra, P.N. Prasad, Imaging pancreatic cancer using bioconjugated InP quantum dots, ACS Nano 3 (2009) 502–510, https://doi.org/10.1021/nn8008933.
[344] J. Zhang, J. Wang, T. Yan, Y. Peng, D. Xu, D. Deng, InP/ZnSe/ZnS quantum dots with strong dual emissions: Visible excitonic emission and near-infrared surface defect emission and their application in in vitro and in vivo bioimaging, J. Mater. Chem. B. 5 (2017) 8152–8160, https://doi.org/10.1039/C7TB02324C.
[345] M. Lim, W. Lee, G. Bang, W.J. Lee, Y. Park, Y. Kwon, Y. Jung, S. Kim, J. Bang, Synthesis of far-red- and near-infrared-emitting Cu-doped InP/ZnS (core/shell) quantum dots with controlled doping steps and their surface functionalization for bioconjugation, Nanoscale 11 (2019) 10463–10471, https://doi.org/10.1039/C9NR02192B.
[346] J.P. Zimmer, S.-W. Kim, S. Ohnishi, E. Tanaka, J.V. Frangioni, M.G. Bawendi, Size series of small indium arsenide-zinc selenide core-shell nanocrystals and their application to in vivo imaging, J. Am. Chem. Soc. 128 (2006) 2526–2527, https://doi.org/10.1021/ja0579816.
[347] P.M. Allen, W. Liu, V.P. Chauhan, J. Lee, A.Y. Ting, D. Fukumura, R.K. Jain, M.G. Bawendi, InAs(ZnCdS) quantum dots optimized for biological imaging in the near-infrared, J. Am. Chem. Soc. 132 (2010) 470–471, https://doi.org/10.1021/ja908250r.
[348] B. Gidwani, V. Sahu, S.S. Shukla, R. Pandey, V. Joshi, V.K. Jain, A. Vyas, Quantum dots: Prospectives, toxicity, advances and applications, J. Drug Deliv. Sci. Technol. 61 (2021), https://doi.org/10.1016/j.jddst.2020.102308.
[349] L. Hu, H. Zhong, Z. He, Toxicity evaluation of cadmium-containing quantum dots: A review of optimizing physicochemical properties to diminish toxicity, Colloids Surf. B 200 (2021), https://doi.org/10.1016/j.colsurfb.2021.111609.
[350] A. Umapathi, M. Kumawat, H.K. Daima, Engineered nanomaterials for biomedical applications and their toxicity: A review, Environ. Chem. Lett. 20 (2022) 445–468, https://doi.org/10.1007/s10311-021-01307-7.
[351] D. Wu, Y. Ma, Y. Cao, T. Zhang, Mitochondrial toxicity of nanomaterials, Sci. Total Environ. 702 (2020), https://doi.org/10.1016/j.scitotenv.2019.134994.
[352] V.I. Naranjo, M. Hendricks, K.S. Jones, Lead toxicity in children: An unremitting public health problem, Pediatr. Neurol. 113 (2020) 51–55, https://doi.org/10.1016/j.pediatrneurol.2020.08.005.
[353] P. Jones, S. Sugino, S. Yamamura, F. Lacy, V. Biju, Impairments of cells and genomic DNA by environmentally transformed engineered nanomaterials, Nanoscale 5 (2013) 9511–9516, https://doi.org/10.1039/C3NR03118G.
[354] C. Kirchner, T. Liedl, S. Kudera, T. Pellegrino, A. Muñoz Javier, H.E. Gaub, S. Stölzle, N. Fertig, W.J. Parak, Cytotoxicity of colloidal CdSe and CdSe/ZnS nanoparticles, Nano Lett. 5 (2005) 331–338, https://doi.org/10.1021/nl047996m.
[355] N. Chen, Y. He, Y. Su, X. Li, Q. Huang, H. Wang, X. Zhang, R. Tai, C. Fan, The cytotoxicity of cadmium-based quantum dots, Biomaterials 33 (2012) 1238–1244, https://doi.org/10.1016/j.biomaterials.2011.10.070.
[356] B. Ballou, B.C. Lagerholm, L.A. Ernst, M.P. Bruchez, A.S. Waggoner, Noninvasive imaging of quantum dots in mice, Bioconjugate Chem. 15 (2004) 79–86, https://doi.org/10.1021/bc034153y.
[357] K.C. Nguyen, P. Rippstein, A.F. Tayabali, W.G. Willmore, Mitochondrial toxicity of cadmium telluride quantum dot nanoparticles in mammalian hepatocytes, Toxicol. Sci. 146 (2015) 31–42, https://doi.org/10.1093/toxsci/kfv068.
[358] I. Corazzari, A. Gilardino, S. Dalmazzo, B. Fubini, D. Lovisolo, Localization of CdSe/ZnS quantum dots in the lysosomal acidic compartment of cultured neurons and its impact on viability: Potential role of ion release, Toxicol. in Vitro. 27 (2013) 752–759, https://doi.org/10.1016/j.tiv.2012.12.016.
[359] K.G. Li, J.T. Chen, S.S. Bai, X. Wen, S.Y. Song, Q. Yu, J. Li, Y.Q. Wang, Intracellular oxidative stress and cadmium ions release induce cytotoxicity of unmodified cadmium sulfide quantum dots, Toxicol. in Vitro. 23 (2009) 1007–1013, https://doi.org/10.1016/j.tiv.2009.06.020.
[360] O.S. Oluwafemi, B.M.M. May, S. Parani, N. Tsolekile, Facile, large-scale synthesis of water soluble $AgInSe_2$/ZnSe quantum dots and its cell viability assessment on different cell lines, Mater. Sci. Eng. C. 106 (2020), https://doi.org/10.1016/j.msec.2019.110181.
[361] G. Chen, F. Tian, Y. Zhang, Y. Zhang, C. Li, Q. Wang, Tracking of transplanted human mesenchymal stem cells in living mice using near-infrared Ag_2S quantum dots, Adv. Funct. Mater. 24 (2014) 2481–2488, https://doi.org/10.1002/adfm.201303263.
[362] C. Tu, X. Ma, A. House, S.M. Kauzlarich, A.Y. Louie, PET imaging and biodistribution of silicon quantum dots in mice, ACS Med. Chem. Lett. 2 (2011) 285–288, https://doi.org/10.1021/ml1002844.
[363] K. Fujioka, M. Hiruoka, K. Sato, N. Manabe, R. Miyasaka, S. Hanada, A. Hoshino, R.D. Tilley, Y. Manome, K. Hirakuri, K. Yamamoto, Luminescent passive-oxidized silicon quantum dots as biological staining labels and their cytotoxicity effects at high concentration, Nanotechnol. 19 (2008), https://doi.org/10.1088/0957-4484/19/41/415102.
[364] E.S. Speranskaya, C. Sevrin, S. De Saeger, Z. Hens, I.Y. Goryacheva, C. Grandfils, Synthesis of hydrophilic $CuInS_2$/ZnS quantum dots with different polymeric shells and study of their cytotoxicity and hemocompatibility, ACS Appl. Mater. Interfaces. 8 (2016) 7613–7622, https://doi.org/10.1021/acsami.5b11258.
[365] W. Zou, L. Li, Y. Chen, T. Chen, Z. Yang, J. Wang, D. Liu, G. Lin, X. Wang, In vivo toxicity evaluation of PEGylated $CuInS_2$/ZnS quantum dots in BALB/c mice, Front. Pharmacol. 10 (2019) 437, https://doi.org/10.3389/fphar.2019.00437.
[366] J.C. Kays, A.M. Saeboe, R. Toufanian, D.E. Kurant, A.M. Dennis, Shell-free copper indium sulfide quantum dots induce toxicity *in vitro* and *in vivo*, Nano Lett. 20 (2020) 1980–1991, https://doi.org/10.1021/acs.nanolett.9b05259.
[367] C.-W. Chen, D.-Y. Wu, Y.-C. Chan, C.C. Lin, P.-H. Chung, M. Hsiao, R.-S. Liu, Evaluations of the chemical stability and cytotoxicity of $CuInS_2$ and $CuInS_2$/ZnS core/shell quantum dots, J. Phys. Chem. C. 119 (2015) 2852–2860, https://doi.org/10.1021/jp510908f.
[368] L. Liu, Y.-Y. Xiao, Y.-H. Ji, M.-Z. Liu, Y. Chen, Y.-L. Zeng, Y.-G. Zhang, L. Jin, $CuInS_2$/ZnS QD exposure induces developmental toxicity, oxidative stress and DNA damage in rare minnow (Gobiocypris rarus) embryos and larvae, Comp. Biochem. Physiol. Part-C: Toxicol. Pharmacol. 198 (2017) 19–27, https://doi.org/10.1016/j.cbpc.2017.04.009.
[369] H. Chibli, L. Carlini, S. Park, N.M. Dimitrijevic, J.L. Nadeau, Cytotoxicity of InP/ZnS quantum dots related to reactive oxygen species generation, Nanoscale 3 (2011) 2552, https://doi.org/10.1039/c1nr10131e.
[370] H. Bahmani Jalali, O. Karatum, R. Melikov, U.M. Dikbas, S. Sadeghi, E. Yildiz, I. B. Dogru, G. Ozgun Eren, C. Ergun, A. Sahin, I.H. Kavakli, S. Nizamoglu, Biocompatible quantum funnels for neural photostimulation, Nano Lett. 19 (2019) 5975–5981, https://doi.org/10.1021/acs.nanolett.9b01697.
[371] H. Bahmani Jalali, M. Mohammadi Aria, U.M. Dikbas, S. Sadeghi, B. Ganesh Kumar, M. Sahin, I.H. Kavakli, C.W. Ow-Yang, S. Nizamoglu, Effective neural photostimulation using indium-based type-II quantum dots, ACS Nano 12 (2018) 8104–8114, https://doi.org/10.1021/acsnano.8b02976.
[372] Z. Bujňáková, E. Dutková, A. Zorkovská, M. Baláž, J. Kováč, M. Kello, J. Mojžiš, J. Briančin, P. Baláž, Mechanochemical synthesis and in vitro studies of chitosan-coated InAs/ZnS mixed nanocrystals, J. Mater. Sci. 52 (2017) 721–735, https://doi.org/10.1007/s10853-016-0366-x.
[373] J. Sobhanan, Y. Takano, S. Sugino, E. Hirata, S. Yamamura, V. Biju, Multimodal CTC detection using stem cell antigen-specific immunosilica particles and immunofluorescent quantum dots, NPG Asia Mater. 14 (2022) 3, https://doi.org/10.1038/s41427-021-00353-5.
[374] P. Kumar, J. Sobhanan, Y. Takano, V. Biju, Molecular recognition in the infection, replication, and transmission of COVID-19-causing SARS-CoV-2: an emerging interface of infectious disease, biological chemistry, and nanoscience, NPG Asia Mater. 13 (2021) 14, https://doi.org/10.1038/s41427-020-00275-8.
[375] A. Anas, J. Sobhanan, K.M. Sulfiya, C. Jasmin, P.K. Sreelakshmi, V. Biju, Advances in photodynamic antimicrobial chemotherapy, J. Photochem. Photobiol. C: Photochem. Rev. 49 (2021) 100452, https://doi.org/10.1016/j.jphotochemrev.2021.100452.
[376] J. Jose, A. Anas, B. Jose, A.B. Puthirath, S. Athiyanathil, C. Jasmin, M.R. Anantharaman, S. Nair, C. Subrahmanyam, V. Biju, Extinction of antimicrobial resistant pathogens using silver embedded silica nanoparticles and an efflux pump blocker, ACS Appl. Bio Mater. 2 (2019) 4681–4686, https://doi.org/10.1021/acsabm.9b00614.